

Important Notice

This copy may be used only for the purposes of research and private study, and any use of the copy for a purpose other than research or private study may require the authorization of the copyright owner of the work in question. Responsibility regarding questions of copyright that may arise in the use of this copy is assumed by the recipient.

UNIVERSITY OF CALGARY

Improving Seismic-to-well Ties

by

Tianci Cui

A THESIS

SUBMITTED TO THE FACULTY OF GRADUATE STUDIES
IN PARTIAL FULFILMENT OF THE REQUIREMENTS FOR THE
DEGREE OF MASTER OF SCIENCE

DEPARTMENT OF GEOSCIENCE

CALGARY, ALBERTA

NOVEMBER, 2015

© Tianci Cui, 2015

Abstract

Seismic-to-well ties are important for seismic interpretation and impedance inversion. Reflectivity can be calculated directly from well logs while its estimation from seismic data requires the determination of the seismic wavelet and the removal of the same. In the presence of anelastic attenuation, the constant-Q theory predicts that the seismic wavelet evolves with amplitude decay and minimum-phase dispersion. Stationary deconvolution estimates and eliminates a single wavelet from the nonstationary trace, resulting in large nonstationary amplitude and phase errors. Gabor deconvolution accurately estimates and eliminates the amplitude spectra of the propagating wavelets, but only corrects the phase to the seismic Nyquist frequency. A phase correction operator is developed to correct the phase to the well logging frequency. Both synthetic and real data examples show seismic-to-well ties can be improved by correcting their time shifts via smooth dynamic time warping and addressing slowly time-variant nonstationarity in a sliding Gaussian window.

Acknowledgements

First of all, I would like to thank my supervisor Dr. Gary Margrave for his inspiration, trust, guidance and support. His decision to take me on as his student is the most important turning point of my life, at least for now. When I started in September 2013, I was asked to test some Matlab code. Being frustrated for weeks, I had to tell him that I did not understand anything. Now I have completed my Master of Science degree with the ability to analyze and solve problems with the help of programming. This would not have been possible without his incredible patience, continuous encouragement, superb signal processing courses, and the stimulating weekly meeting. I could not have imagined having a better supervisor than Gary.

I would like to acknowledge all the technical training from CREWES at the University of Calgary. Thank you to Dr. Larry Lines for teaching us the fundamental interpretation course, his valuable suggestions on my GOPH 701 project, being on my thesis defense committee and his careful proof-reading of my thesis. Thank you to Dr. Kris Innanen for giving us profound courses on multiples, interferometry and inversion, which opened the door to my oncoming Ph.D. studies. Thank you to Dr. Rob Ferguson for teaching us the seismic imaging course. Thank you to Dr. Don Lawton for sharing dataset with me for testing. Thank you to Dr. John Bancroft for teaching us practical migration course and posing thought-provoking questions on my GOPH 701 project. I would also like to thank Dr. Cristian Rios for being my external examiner.

I would like to thank all the support staff at CREWES as well. Thank you to Laura for making everything ready for us to succeed. She always makes CREWES full of vigor and vitality. Thank you to Kevin Hall and Rolf Maier for their technical support whenever it is needed. Thank you to Dr. Helen Isaac for providing the Hussar data. Thank you to Dr. Joe Wong, Dr. Peter Manning and Dr. David Henley for their insight and encouragement on my

CREWES technical talks. Thank you to Kevin Bertram for the guidance in the field work and printing the posters for us.

I am grateful to CREWES sponsors and NSERC (Natural Science and Engineering Research Council of Canada) for their financial support. I would like to thank the SEG Foundation, Department of Geoscience at the University of Calgary and AITF (Alberta Innovates-Technology Futures) for awarding me scholarships.

This thesis also benefits from my fellow students and colleagues at CREWES. Thank you to Wenyong Pan for collaboration on GOPH 657 project. He sets me a great example for his enthusiasm, diligence and humility. Thank you to Raúl Cova and Babatunde Arenrin for all the science you have taught me. Thank you to Jean Cui for helping me with my thesis defense. Thank you to Penny Pan, Bona Wu, Rafael Asuaje and Marcelo Guarido de Andrade for sharing my happiness and sorrow. Thank you to Sina Esmaili for helpful discussions on our theses. Thank you to Michelle Montano, Shahin Jabbari, Shahin Moradi and Eric Rops for great cooperation in student activities. Thank you to visiting scholars Shengjun Li and Tiansheng Chen for stimulating conversations on my work. Thank you to Junxiao Li, Jian Sun, Khaled Al Dulaijan, Jessica Dongas, Jesse Kolb, Shahpoor Moradi, Winnie Ajiduah, Bobby Gunning and Scott Keating for sharing my graduate studies.

This thesis would not have been possible without the support at home. Thank you to my dad Benjing Cui and mom Chunyan Wu. They are far away in China and have no idea what I was doing here, but they keep encouraging me and caring about me all the time. Thank you to my boyfriend Mingxu Ma. Not only does his good work inspire me, but also he takes a good care of my studies and life with unending patience: offering me useful tips, cooking delicious meals, picking me up home and so on. Thank you for everything.

Dedication

To my beloved parents and Mingxu

致我亲爱父母和铭勛，感谢他们的爱与关怀

Table of Contents

Abstract	ii
Acknowledgements	iii
Dedication	v
Table of Contents	vi
List of Figures and Illustrations	viii
List of Symbols, Abbreviations and Nomenclature	xvi
CHAPTER ONE: INTRODUCTION	1
1.1 Why seismic-to-well ties are important	1
1.2 Why seismic-to-well ties are imperfect	1
1.3 Seismic-to-well ties in industrial practice	2
1.4 Improving seismic-to-well ties in the literature	4
1.5 Overview of chapters	5
1.6 Software and development	6
1.7 Original contributions	6
CHAPTER TWO: DYNAMIC TIME WARPING AND SMOOTH DYNAMIC TIME WARPING	7
2.1 Chapter overview	7
2.2 Dynamic time warping	7
2.2.1 Introduction	7
2.2.2 Constrained optimization	10
2.2.3 Dynamic programming	11
2.3 Smooth dynamic time warping	14
2.4 Time-variant crosscorrelation	19
2.5 Summary	20
CHAPTER THREE: SEISMIC-TO-WELL TIES BY STATIONARY DECONVOLUTION	21
3.1 Chapter overview	21
3.2 Stationary convolutional model	21
3.3 Stationary deconvolution	22
3.4 Constant-Q model	26
3.5 Nonstationary convolutional model	30
3.6 Nonstationary analysis and processing tools	33
3.6.1 Time-variant amplitude balancing	34
3.6.2 Time-variant constant-phase rotation and estimation	35
3.6.3 Time-variant crosscorrelation	37
3.7 Stationary deconvolution on the nonstationary seismic trace	39
3.8 Summary	44
CHAPTER FOUR: SEISMIC-TO-WELL TIES BY GABOR DECONVOLUTION	45
4.1 Chapter overview	45
4.2 Gabor deconvolution	45
4.3 Phase correction of Gabor deconvolution	53

4.4 Residual drift time estimation after Gabor deconvolution.....	64
4.5 Summary.....	66
CHAPTER FIVE: SEISMIC-TO-WELL TIES ON HUSSAR SYNTHETICS AND FIELD	
DATA	68
5.1 Chapter overview	68
5.2 Seismic-to-well ties on well-based 1-D seismogram models	69
5.2.1 Hypothetical Q log	69
5.2.2 Drift time	71
5.2.3 Well-based 1-D seismogram models.....	73
5.2.4 Tying the nonstationary trace with Q effects to the well reflectivity	75
5.2.5 Q estimation.....	77
5.2.6 Inclusion of internal multiples.....	80
5.3 Seismic-to-well ties on Hussar field data	85
5.3.1 Data preparation	85
5.3.2 Seismic-to-well ties	90
5.3.3 Bandlimited impedance inversion	95
5.3.4 Discussion.....	98
5.4 Summary.....	106
CHAPTER SIX: CONCLUSIONS.....	108

List of Figures and Illustrations

Figure 2.1: Two synthetic traces (top) and the time shift sequence between them (bottom).	8
Figure 2.2: Alignment error array where dark blue indicates the error values are small.	9
Figure 2.3: The known lag sequence is plotted in white on top of the alignment error array.	10
Figure 2.4: Distance array where dark blue indicates the error values are small. The lag sequence calculated by DTW is plotted in white on top of the distance array.	13
Figure 2.5: Known and DTW estimated time shift sequences (top). Time shifted s1 by DTW in comparison with s2 (bottom).	13
Figure 2.6: Zoomed-in version of alignment error array, on top of which are the 3 subpaths searched for a certain sample location in red lines, the known lag sequence in solid white curve and the estimated lag sequence by DTW in dotted white curve.	15
Figure 2.7: Zoomed-in version of alignment error array, on top of which are the 11 subpaths searched for a certain sample location in red lines, the known lag sequence in solid white curve, and the estimated lag sequence by SDTW in dotted white curve with white circles indicating the coarse sample locations where its subpaths are calculated.	16
Figure 2.8: Distance array accumulated every 100 th sample. The lag sequence calculated by SDTW is plotted in white on top of the distance array.	18
Figure 2.9: Known and estimated time shift sequences (top). Time shifted s1 by SDTW in comparison with s2 (bottom).	18
Figure 2.10: The known time shift sequence and its estimate (top). Time-variant crosscorrelation coefficient (middle). Time shifted s1 compared to s2 (bottom).	20
Figure 3.1: The stationary convolutional model is illustrated. The left panel is the Toeplitz matrix in gray, on top of which are wavelets plotted every 0.1 second in blue using wiggle-trace variable-area format. It multiplies a column vector containing a reflectivity series (middle) to produce the stationary trace (right).	22
Figure 3.2: Amplitude spectra of the wavelet, reflectivity, seismic trace and the wavelet estimated by the frequency domain spiking deconvolution.	25
Figure 3.3: The known wavelet (solid red), estimated wavelet (dotted black), known reflectivity (solid blue) and estimated reflectivity (solid black) in the time domain. The wavelets are both delayed by 0.5 seconds for a better display.	25
Figure 3.4: A minimum-phase source wavelet with a dominant frequency of 30 Hz (red) is shown after various traveltimes (blue) assuming a Q of 50.	29
Figure 3.5: Amplitude spectra of the wavelets in Figure 3.4.	29

Figure 3.6: The velocity is dependent on frequency for various Q values assuming $v_0 = 3000$ m/s at the well logging frequency of $f_0 = 12.5$ kHz.	30
Figure 3.7: The nonstationary convolutional model is illustrated. The left panel is the Q matrix in gray, on top of which are wavelets plotted every 0.1s in red using wiggle-trace variable-area format. The bandlimited evolving wavelets lag behind the dashed blue diagonal by a progressively increasing amount. The Q matrix multiplies a column vector containing a reflectivity series (middle) to produce the nonstationary trace (right).	32
Figure 3.8: Comparison of stationary and nonstationary traces in the time and frequency domains.	33
Figure 3.9: Time-variant amplitude balancing is illustrated. Seismic traces with and without time-variant balancing compared to the reference trace (top). The known time-variant scalar function and its estimate (bottom).	35
Figure 3.10: Time-variant constant-phase rotation and estimation are illustrated. Seismic traces before and after time-variant constant-phase rotation compared to the reference trace (top). The known time-variant constant-phase function and its estimate (bottom).	37
Figure 3.11: Time-variant crosscorrelation is illustrated. Seismic traces before and after time-variant time shift compared to the reference trace (top). The known time-variant time shift function and its estimate (middle). Time-variant crosscorrelation coefficient (bottom).	39
Figure 3.12: A procedure of tying the nonstationary trace to the known reflectivity by stationary deconvolution, time-variant amplitude balancing and time-variant constant-phase rotation.	42
Figure 3.13: The estimated wavelet in comparison with the embedded evolving wavelets propagating to different traveltimes in the frequency domain.	42
Figure 3.14: Amplitude spectra of the deconvolved seismic trace within different time ranges in decibels.	43
Figure 3.15: The time-variant constant-phase differences between the known reflectivity and the deconvolved trace before and after phase rotation (top). The time-variant crosscorrelation coefficient sequences between the known reflectivity and the nonstationary trace, the deconvolved trace after time-variant amplitude balancing, the deconvolved trace after time-variant amplitude balancing and time-variant constant-phase rotation (middle). The time-variant time shift sequences at which the coefficients are obtained (bottom).	43
Figure 4.1: The forward and inverse Gabor transform is demonstrated. The nonstationary trace after forward and inverse Gabor transform is on top of the original trace (left). A set of selected Gaussian windows used for the forward Gabor transform (middle). The Gabor magnitude spectrum of the nonstationary trace (right).	46

Figure 4.2: The magnitude of three components: the Fourier transform of the source wavelet duplicated along the travelttime (left), the attenuation function represented on the time-frequency plane (middle) and the Gabor spectrum of the reflectivity (right).	48
Figure 4.3: The pointwise product of the three magnitude spectra in Figure 4.2 (left) and the Gabor magnitude spectrum of the nonstationary trace (right), which is the same as Figure 4.1 right panel.	48
Figure 4.4: The Gabor magnitude spectra of the propagating wavelet (left), the estimated propagating wavelet (middle) and the estimated reflectivity (right) by Gabor deconvolution.	49
Figure 4.5: A procedure of tying the nonstationary trace to the known reflectivity (blue) by Gabor deconvolution, time-variant amplitude balancing and time-variant constant-phase rotation.	52
Figure 4.6: Amplitude spectra of the Gabor deconvolved seismic trace within different time ranges in decibels.	52
Figure 4.7: The time-variant constant-phase differences between the known reflectivity and the Gabor deconvolved trace before and after phase rotation (top). The time-variant crosscorrelation coefficient sequences between the known reflectivity and the nonstationary trace, the Gabor deconvolved trace after time-variant amplitude balancing, the Gabor deconvolved trace after time-variant amplitude balancing and time-variant constant-phase rotation (middle). The time-variant time shift sequences at which the coefficients are obtained (bottom).	53
Figure 4.8: Comparison of the propagating wavelets estimated by Gabor deconvolution and those modeled by the Q matrix in Figure 3.7.	54
Figure 4.9: Amplitude spectra of the wavelets propagating to four different times in Figure 4.8.	55
Figure 4.10: Phase spectra of the wavelets propagating to four different times in Figure 4.8.	55
Figure 4.11: Comparison of the Q matrixes in gray built using the well logging frequency (left, the same as Figure 3.7 left panel) and the seismic Nyquist frequency (right) as the reference frequency respectively.	58
Figure 4.12: Same as Figure 4.10 except that the phase spectra of the propagating wavelets modeled by the Q matrix with respect to the seismic Nyquist frequency are plotted as well.	58
Figure 4.13: The time-domain propagating wavelets at four different times estimated by Gabor deconvolution, modeled by the Q matrixes with respect to the well logging frequency and the seismic Nyquist frequency.	59

Figure 4.14: Same as Figure 4.12 except that the wavelets estimated by Gabor deconvolution are phase corrected.....	60
Figure 4.15: Same as Figure 4.13 except that the wavelets estimated by Gabor deconvolution are phase corrected.....	61
Figure 4.16: Comparison of the propagating wavelets estimated by Gabor deconvolution with phase correction and those modeled by the Q matrix with respect to the well logging frequency in Figure 3.7.....	61
Figure 4.17: A procedure of tying the nonstationary trace to the known reflectivity (blue) by Gabor deconvolution, phase correction, time-variant amplitude balancing and time-variant constant-phase rotation.	63
Figure 4.18: The time-variant constant-phase differences (top), the time-variant crosscorrelation coefficient sequences (middle) and the time-variant time shift sequences at which the coefficients are obtained (bottom) between the known reflectivity and the Gabor deconvolved trace, the Gabor deconvolved trace after phase correction, the Gabor deconvolved trace after phase correction, time-variant amplitude balancing and time-variant constant-phase rotation.....	63
Figure 4.19: The Gabor deconvolved trace corrected by the known residual drift time, the residual drift time estimated by time-variant crosscorrelation and the residual drift time estimated by smooth dynamic time warping compared to the well reflectivity (blue) separately.	65
Figure 4.20: Residual drift time after Gabor deconvolution: the known function, time-variant crosscorrelation estimate and smooth dynamic time warping estimate (top). Time-variant time shift sequences between the known reflectivity and the Gabor deconvolved trace corrected by the known residual drift time, corrected by the residual drift time estimated by time-variant crosscorrelation and corrected by the residual drift time estimated by smooth dynamic time warping (bottom).	66
Figure 5.1: The location of the seismic line and wells in Hussar experiment (Lloyd, 2013).	69
Figure 5.2: Logs from Hussar well 12-27.....	70
Figure 5.3: Time-depth relations at different frequencies (left) and the drift time with respect to depth (right).	73
Figure 5.4: Construction of a stationary seismogram $s(t)$	74
Figure 5.5: The primaries-only upgoing wavefield of the synthetic zero-offset VSP model with Q effects.	75
Figure 5.6: The stationary seismogram $s(t)$ and the nonstationary trace with Q effects $s_q(t)$ (top), the reflectivity estimate without phase correction compared to the well reflectivity	

(middle), the reflectivity estimate with phase correction compared to the well reflectivity (bottom).	76
Figure 5.7: The estimated drift time and residual drift time sequences compared to the known ones (top). The time-variant constant-phase differences between the well reflectivity and Gabor deconvolved $sq(t)$ with and without phase correction (middle). The time-variant crosscorrelation coefficients at lag zero between the well reflectivity and its estimates with and without phase correction (bottom).	77
Figure 5.8: The known interval Q , known average Q , estimated average Q from drift time and residual drift time estimation.	78
Figure 5.9: The reflectivity estimates (red) with phase correction using a series of time-invariant Q values compared to the well reflectivity (blue).	79
Figure 5.10: The overall crosscorrelation coefficients between the reflectivity estimates and the well reflectivity at lag zero with respect to the corresponding time-invariant Q values used for phase correction and there is no phase correction are plotted as stars for reference.	80
Figure 5.11: The upgoing wavefield of the synthetic zero-offset VSP model with both Q and internal multiple effects.	83
Figure 5.12: The stationary seismogram $s(t)$, the nonstationary trace with Q effects only $sq(t)$, the nonstationary trace with both Q and internal multiple effects $sqi(t)$ (top). The estimated drift time and residual drift time sequences compared to the known ones (bottom).	83
Figure 5.13: The known interval intrinsic Q , known average intrinsic Q , estimated average apparent Q from drift time estimation and that from residual drift time estimation in the presence of internal multiples.	84
Figure 5.14: The reflectivity estimate without phase correction (top), with phase correction associated with the intrinsic Q (middle) and with phase correction associated with the apparent Q (bottom) compared to the well reflectivity.	84
Figure 5.15: The time-variant constant-phase differences between the well reflectivity and Gabor deconvolved $sqi(t)$ without phase correction, with phase correction associated with the intrinsic Q , with phase correction associated with the apparent Q and Gabor deconvolved $sq(t)$ with phase correction associated with the intrinsic Q (top). The time-variant crosscorrelation coefficients at lag zero between the well reflectivity and its final estimates (bottom).	85
Figure 5.16: The 2-D seismic section after processing and migration. The three wiggle traces in red are the average traces at the corresponding well locations.	87
Figure 5.17: The density log and P-wave velocity log from each well after being edited.	87

Figure 5.18: Reflectivity calculated from each well.	88
Figure 5.19: The zero-phase wavelet estimated from the average trace at each well location.	88
Figure 5.20: The synthetic seismogram and the average trace at the corresponding well location before being tied. The cc values annotated are their overall crosscorrelation coefficients at lag zero.	89
Figure 5.21: The 2-D seismic section, on top of which are the untied synthetic seismograms at the corresponding well locations separated by the dotted red lines.	89
Figure 5.22: The time shifts between the synthetic seismogram and the average trace at the corresponding well location (top). The time-variant constant-phase difference between the average trace and the synthetic seismogram after time calibration at each well location (middle). The time-variant amplitude scaler function between the phase rotated average trace and the synthetic seismogram after time calibration at each well location (bottom).....	91
Figure 5.23: The original and time shifted reflectivities at each well.	92
Figure 5.24: The reconstructed synthetic seismogram and the average trace at the corresponding well location after the timing of the reflectivity being corrected. The cc values annotated are their overall crosscorrelation coefficients at lag zero.....	92
Figure 5.25: The 2-D time-variant constant-phase, on top of which are the phases used for interpolation and extrapolation at the corresponding well locations separated by the dotted white lines.	93
Figure 5.26: The 2-D time-variant amplitude scalar, on top of which are the scalars used for interpolation and extrapolation at the corresponding well locations separated by the dotted white lines.	93
Figure 5.27: The 2-D seismic section after phase rotation and amplitude balancing, on top of which are the synthetic seismograms after time calibration at the corresponding well locations separated by the dotted red lines.....	94
Figure 5.28: The synthetic seismogram and the average trace at the corresponding well location after being tied. The cc values annotated are their overall crosscorrelation coefficients at lag zero.	94
Figure 5.29: The 2-D interpolated well impedance, on top of which are the well impedance used for interpolation and extrapolation at the corresponding well locations separated by the dotted white lines.	96
Figure 5.30: The 2-norm errors between the log impedance and the impedance inversion of the seismic trace at each well location using different low frequency cut-offs.	97

Figure 5.31: Bandlimited impedance inversion of the 2-D seismic section, on top of which are the low-pass filtered well impedance separated by the dotted white lines at the corresponding well locations with the tops annotated.	97
Figure 5.32: Comparison of the low-passed well impedance and the bandlimited seismic impedance inversion at each well location with their percent errors denoted.	98
Figure 5.33: The results in the second iteration of time calibration are shown. The time shifts between the average trace and the synthetic seismogram after time calibration once (top). The time-variant constant-phase difference between the average trace and the synthetic seismogram after time calibration twice (middle). The time-variant amplitude scaler function between the phase rotated average trace and the synthetic seismogram after time calibration twice (bottom).	99
Figure 5.34: The results in the third iteration of time calibration are shown. The time shifts between the average trace and the synthetic seismogram after time calibration twice (top). The time-variant constant-phase difference between the average trace and the synthetic seismogram after time calibration three times (middle). The time-variant amplitude scaler function between the phase rotated average trace and the synthetic seismogram after time calibration three times (bottom).	100
Figure 5.35: The 2-D time-variant constant-phase after two iterations, on top of which are the phases used for interpolation and extrapolation at the corresponding well locations separated by the dotted white lines.	101
Figure 5.36: The 2-D time-variant amplitude scalar after two iterations, on top of which are the scalars used for interpolation and extrapolation at the corresponding well locations separated by the dotted white lines.	102
Figure 5.37: The final well tying results after two iterations of time calibration are shown. The 2-D seismic section after phase rotation and amplitude balancing, on top of which are the synthetic seismograms after time calibration twice at the corresponding well locations separated by the dotted red lines.	102
Figure 5.38: The synthetic seismogram and the average trace at the corresponding well location after being tied through two iterations of time calibration. The cc values annotated are their overall crosscorrelation coefficients at lag zero.	103
Figure 5.39: The time-variant crosscorrelation coefficients between the synthetic seismogram and the seismic trace before well tying, after well tying with time calibration once and after well tying with time calibration twice.	103
Figure 5.40: Bandlimited impedance inversion of the 2-D seismic section, with two iterations of time calibration in the well tying, on top of which are the low-pass filtered well impedance separated by the dotted white lines at the corresponding well locations with the tops annotated.	104

Figure 5.41: Comparison of the low-passed well impedance and the bandlimited seismic impedance inversion with two iterations of time calibration in the well tying. Their impedance percent errors are denoted..... 105

Figure 5.42: The impedance percent errors between the seismic impedance inversion and the interpolated well impedance at every CDP location, with one and two iterations of time calibration in the well tying. 105

List of Symbols, Abbreviations and Nomenclature

Symbol	Definition
AGC	Automatic gain correction
BLIMP	Bandlimited impedance inversion
$cc(t)$	A time-variant crosscorrelation coefficient function
CDP	Common depth point
CREWES	Consortium for Research in Elastic Wave Exploration Seismology
$d(m, n)$	A distance array in lag m and sample number n
dt_k	The two-way time thickness of the k^{th} layer
dz_k	The k^{th} layer thickness
$D[m(1:N)]$	A total distance which is the cumulative errors summing along the path $m(1:N)$ in the alignment error array
DTW	Dynamic time warping
$e(m, n)$	An alignment error array in lag m and sample number n
f	Frequency, the Fourier dual to t or τ
f_0	The reference frequency of the constant-Q model
f_c	The low frequency cut-off in BLIMP
f_h	The high-end frequency in BLIMP
f_{NYQ}	The seismic Nyquist frequency
f_w	The well logging frequency
$g_\sigma(t - \tau)$	A Gaussian function of standard width 2σ centered at time τ

h	A coarse sampling interval used in smooth dynamic time warping
$I_{inversion}$	Seismic impedance inversion
I_{well}	Well impedance
L	The maximum of the searched lag
$m(n)$	A lag between two traces at a sample number n
n	The time sample number
$nshift$	The lag sequence, which is the time shift function expressed in lags
N	The maximum time sample number
Q	The quality factor in the constant-Q model
Q_{ave}	The average Q
Q_k	The interval Q of the k^{th} layer
$r(t)$	Reflectivity as a time signal
$\hat{r}(f)$	The Fourier transforms of $r(t)$
$\hat{r}_g(\tau, f)$	The forward Gabor transform of the reflectivity $r(t)$, which is a complex-valued time-frequency decomposition
RMS	Root mean square
$s(t)$	A seismic trace
$\hat{s}(f)$	The Fourier transform of $s(t)$
$\hat{s}_g(\tau, f)$	The forward Gabor transform of the seismic trace $s(t)$, which is a complex-valued time-frequency decomposition
$s_q(t)$	A nonstationary seismic trace including Q effects only
$s_{qi}(t)$	A nonstationary seismic trace including both Q

	and internal multiple effects
$s^\theta(t)$	A trace s after θ degree phase rotation
$s^\sigma(\tau)$	A trace s windowed by a Gaussian function $g_\sigma(t)$ of standard width 2σ centered at time τ
$scalar(t)$	A time-variant scalar function used to illustrate time-variant amplitude balancing
SDTW	Smooth dynamic time warping
t, τ	Variables denoting the time coordinate
$tshift$	A time-variant time shift function used to illustrate dynamic time warping and time-variant crosscorrelation
TVCC	Time-variant crosscorrelation
$u(n)$	The lag sequence computed by dynamic time warping
v_0	The reference velocity of the constant-Q model
v_k	The velocity of the k^{th} layer
v_p	The value of a P-wave velocity log
VSP	Vertical seismic profile
$w(t), w_0(t)$	The source wavelet or signature
$\widehat{w}(f), \widehat{w}_0(f)$	The Fourier transform of the source wavelet
$w_Q(\tau, t)$	The propagating wavelet at travelttime τ
$\widehat{w}_Q(\tau, f)$	The Fourier transform of the propagating wavelet at travelttime τ
z_k	The depth to the k^{th} layer
$\alpha(\tau, t)$	The impulse response of the attenuation process for an impulse at time τ
$\alpha(\tau, f)$	The attenuation function in the time-frequency

domain, which is the Fourier transform of $a(\tau, t)$ over the second variable

$\Delta drift(t)$

The residual drift time remaining in the nonstationary seismic trace after Gabor deconvolution compared to the well reflectivity

$\Delta\varphi(t, f)$

The residual phase remaining in the nonstationary seismic trace after Gabor deconvolution compared to the well reflectivity

$\vartheta(t)$

A time-variant constant-phase function used to illustrate time-variant constant-phase rotation

ρ

The value of a density log

$\varphi_{w_Q}(t, f)$

The phase spectrum of the propagating wavelet at traveltime t

$\varphi_{w_Q}^H(t, f)$

The phase spectrum of the propagating wavelet at traveltime t estimated by the digital Hilbert transform

$\varphi_{w_Q}^{H,c}(t, f)$

The phase spectrum of the propagating wavelet at traveltime t estimated by the digital Hilbert transform and being phase corrected

Chapter One: Introduction

1.1 Why seismic-to-well ties are important

Reflection seismology is essential for modern petroleum exploration. Seismic data allows us to estimate the subsurface properties between control points of existing wells (Lines and Newrick, 2004). Well formations provide us clues about identifying and tracing seismic reflections in seismic data interpretation. Moreover, the well measurements can obtain a wide bandwidth while seismic data is always bandlimited and lacks very low frequencies due to the source, receiver and earth effects. Without low frequency information, seismic inversion can only prescribe a deviation of earth property values from an unknown trend, which can be compensated by well logs.

Seismic interpretation and inversion are possible only if we can correlate seismic reflections to well log formations. This is usually done by calculating a reflectivity from sonic and density logs and then bandlimiting it as a synthetic seismogram to match the seismic trace, which should be a robust estimate of bandlimited reflectivity after processing. However, the synthetic seismogram and the seismic trace are never seen to be perfectly tied automatically.

1.2 Why seismic-to-well ties are imperfect

Seismic-to-well ties are the process of using the well information to calibrate the seismic estimate (Margrave, 2013c), since seismic-to-well ties are always imperfect for the following reasons (Hampson-Russell Software, 2013; Margrave, 2013)

- Well logging traveltime corresponding to a particular depth, depends on all the velocities above that depth including the top of the log to the surface. However, logs are not usually recorded near the surface, so the overburden velocities are unknown.

- Problems with sonic logs such as cycle skipping or mud invasion produces cumulative errors in the calculated traveltime.
- Problems with seismic traces such as noise or mispositioned events due to imperfect processing.
- The six inch borehole measurements may not represent the wider stratigraphy, structure or anisotropy.
- Well tying is usually done to primary reflectivity but there may be multiples present in the seismic data.
- The presence of anelastic attenuation makes velocity dependent on frequency. Thus, velocities propagating at the seismic frequencies (below 50Hz) are systematically lower than those measured at the well logging frequency (about 12.5 kHz).
- Wavelets vary both in space and in time due to anelastic attenuation, near surface effects, inter-bed multiples, NMO stretch, anisotropy and etc.

This thesis is mainly to address the misties caused by anelastic attenuation.

1.3 Seismic-to-well ties in industrial practice

The standard steps of seismic-to-well ties modified from White and Simm (2003) are:

- 1 Edit well logs and process seismic data.
- 2 Calibrate the sonic times to seismic times.
- 3 Create a reflectivity using the calibrated sonic times.
- 4 Estimate a zero-phase wavelet from the seismic trace at the well location.
- 5 Construct a synthetic seismogram by convolving the well reflectivity with the estimated wavelet.

- 6 The phase of the seismic trace is rotated by a single constant-phase (independent of frequency) to maximize its correlation with the synthetic seismogram.

In the first step, the standard seismic data processing estimates the reflectivity by determining a single seismic wavelet in the target zone and removing the same through stationary deconvolution. However, in the presence of anelastic attenuation, the very notion of a single seismic wavelet is not robust. The extracted wavelet is adequate for zone-of-interest interpretation but becomes increasingly erroneous above and below the analysis window (Margrave, 2013).

The second step is the most important step because timing errors in the synthetic seismogram are much more detrimental than amplitude errors (White and Simm, 2003). With knowledge of attenuation factor Q , the expected sonic velocities at the seismic frequency can be calculated according to the constant- Q theory (Kjartansson, 1979). Or with a VSP (vertical seismic profile) or a check-shot survey available, the integrated sonic times and the seismic first arrival times are compared at equal depths to create a time-depth relationship. In the most cases where Q values, check-shot or VSP surveys are not available, the synthetic seismogram has to go through an interpretive stretch-squeeze process to match the same events on seismic trace based on their visual similarity. This process is subjective and is often labeled as unscientific (White and Simm, 2003).

Since deconvolution never perfectly eliminates the embedded wavelets from the seismic trace especially for the real data, the wavelet estimated in the fourth step is a residual wavelet after deconvolution, which should be time-variant as a result of running stationary deconvolution on the nonstationary seismic trace. Thus, the time-invariant constant-phase in the sixth step may be insufficient to remove the residual phase in the deconvolved seismic trace. A time-variant

phase correction operator is needed to rotate the residual wavelets so that the maximum energy is centered at the reflection coefficients as required by interpretation and inversion.

1.4 Improving seismic-to-well ties in the literature

In this thesis, frequency-dependent attenuation is considered as the major cause of the misties. The nonstationarity of seismic traces is addressed by many authors, whose studies generally fall into two distinct classes: the inverse Q filtering and the nonstationary deconvolution (Margrave et al., 2011). The inverse Q filtering is an exponential amplitude increase in both time and frequency, so it is unstable blowing up even a small amount of noise (Margrave, 2013c). Another difficulty is that the inverse Q filtering requires knowledge of the Q structure, which is difficult to measure and can only be crudely estimated at present (Cheng, 2013). Gabor deconvolution (Margrave et al., 2011) is a nonstationary deconvolution algorithm that corrects for both wavelet shape and attenuation. Without Q information, it measures the inherent attenuation from the data directly. Thus, the data adaptive process does not suffer from instability and better deals with noise. However, large and time-variant phase errors remain in the Gabor deconvolved trace compared to the well reflectivity (Margrave, 2013c).

As seismic-to-well ties involve estimating and correcting relative time shifts between synthetic seismogram and seismic traces, Munoz and Dave (2012), Herrera and van der Baan (2014) and Herrera et al. (2014) replace the stretching and squeezing step with a constrained dynamic time warping (DTW) technique, which can warp synthetic seismogram to tie seismic traces automatically. Although a high correlation can usually be achieved, the time shifts estimated by DTW are not smooth enough to approximate the actual drift time, and can be distorted by noise and phase errors to make them “overtied”. Compton and Hale (2014) further develop a smooth

dynamic time warping (SDTW) technique by introducing a coarse sampling interval so that the estimated time shifts are smoother and more accurate. Munoz and Hale (2015) apply SDTW to seismic-to-well ties. Although the estimated time shifts are more realistic, they are used to warp the synthetic seismogram directly to tie the seismic trace, whose nonstationary residual phase is not corrected and may lead to inversion errors.

1.5 Overview of chapters

This thesis is presented in 6 chapters.

Chapter 2 illustrates a new technique named smooth dynamic time warping to estimate smooth time shifts between two traces.

Chapter 3 builds the stationary and nonstationary convolutional models, the latter of which is based on the constant-Q theory. The case of running stationary deconvolution on the nonstationary seismic trace to tie the well reflectivity is discussed. A set of nonstationary analysis and processing tools is introduced.

In Chapter 4, the nonstationary seismic trace is tied to the well reflectivity by Gabor deconvolution. A phase correction operator is developed with the help of smooth dynamic time warping.

In Chapter 5, nonstationary synthetic seismograms are built and are tied to a Hussar well by Gabor deconvolution with phase correction. The Hussar 2-D seismic section is tied to three Hussar wells with the help of smooth dynamic time warping and nonstationary analysis and processing tools. Bandlimited impedance inversion is conducted to examine the quality of seismic-to-well ties.

In Chapter 6, conclusions from Chapter 2 to 5 are summarized.

1.6 Software and development

The main software used in this thesis is MATLAB® which is a high-level programming language developed by MathWorks. CREWES has been developing a MATLAB toolbox with a variety of modeling, processing and utility functions, which are extensively used in this thesis. Several new MATLAB tools are developed and some existing MATLAB tools are upgraded as a product of this thesis, which will be introduced in the next section.

1.7 Original contributions

- A new function named *DTW* is developed to estimate the time shifts between two signals by warping one to match the other based on dynamic time warping algorithm. It is described in detail in Section 2.2.
- A new function named *DTWs* is developed to estimate the smooth time shifts between two signals by warping one to match the other based on smooth dynamic time warping algorithm. It is described in detail in Section 2.3.
- A new function named *tvccorr* is developed to conduct time-variant crosscorrelation between two signals. It is described in detail in Section 2.4 and 3.6.3.
- An existing function named *deconf*, which performs frequency domain spiking deconvolution, is upgraded by adding different window types to smooth the amplitude spectrum of the seismic trace. Available choices are boxcar, Gaussian, Hanning and Bartlett.
- An existing function named *gabordecon*, which performs Gabor deconvolution, is upgraded by including phase correction with input Q values or residual drift time. It is described in detail in Section 4.3 and 4.4.

Chapter Two: Dynamic time warping and smooth dynamic time warping

2.1 Chapter overview

This chapter builds a set of tools to estimate the time shifts between two traces. First, a new technique called dynamic time warping (DTW) is introduced. It is based on a constraint optimization algorithm and is realized by dynamic programming. Then an improved approach called smooth dynamic time warping (SDTW) is discussed to estimate smooth time shifts. Finally, DTW and SDTW are compared to the common time-variant crosscorrelation (TVCC) method. The application of SDTW in drift time or residual drift time estimation in seismic-to-well ties will be illustrated in Chapter 4 and Chapter 5.

2.2 Dynamic time warping

2.2.1 Introduction

Consider two synthetic traces $s_1(n)$ and $s_2(n)$ shown in Figure 2.1 top panel where n is sample number. Trace $s_1(n)$ is computed by convolving a random reflectivity series with a minimum-phase wavelet whose dominant frequency is 30 Hz. Trace $s_1(n)$ is then warped by a time-variant shift sequence $tshift(n)$ to obtain trace $s_2(n)$. The maximum crosscorrelation coefficient between $s_1(n)$ and $s_2(n)$ is 0.4 and this occurs at a lag of -24.2 milliseconds (a negative lag value indicates s_2 is delayed relative to s_1). Time shift sequence $tshift(n)$ is a sinusoidal function as shown in Figure 2.1 bottom panel. Representing the time shifts $tshift(n)$ as lag $nshift$

$$nshift(n) = \frac{tshift(n)}{dt}, \quad (2.1)$$

where dt is the time sample interval and $nshift$ is not restricted to integer values. Therefore, the two traces are related by

$$s_1(n) = s_2(n + nshift(n)). \quad (2.2)$$

The dynamic time warping (DTW) method (Hale, 2013) is adapted to estimate the time shift sequence $nshift(n)$ given the traces $s_1(n)$ and $s_2(n)$. Then trace $s_1(n)$ is warped by the estimated $nshift(n)$ using Equation 2.2 so that the two traces gain a better correlation with each other.

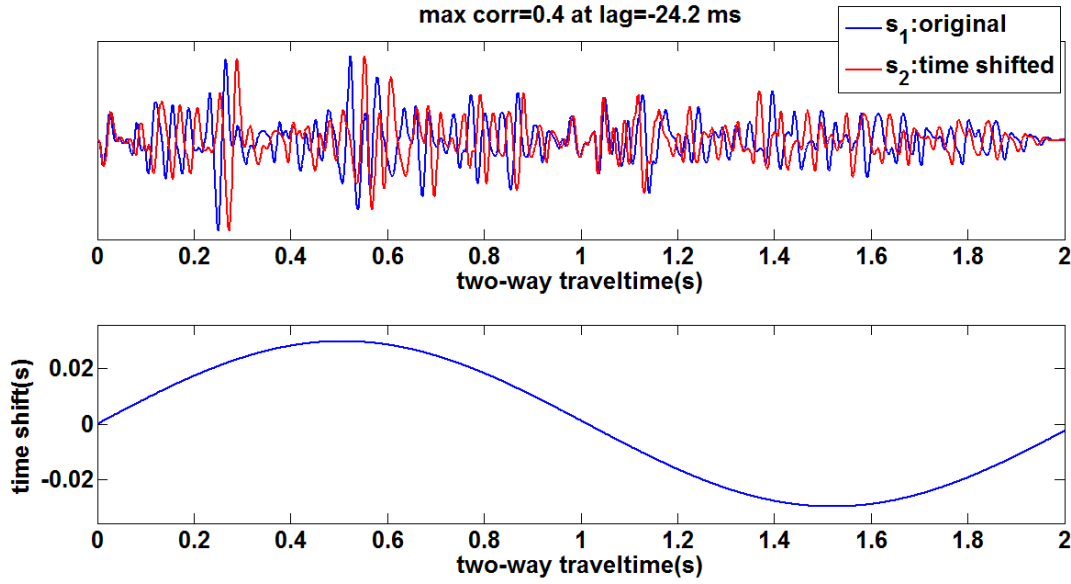


Figure 2.1: Two synthetic traces (top) and the time shift sequence between them (bottom).

To find the time-variant lag between the two traces, an alignment error array e is calculated according to

$$e(m, n) = |s_1(n) - s_2(n + m)| \quad (2.3)$$

for all the sample numbers $n = 1, 2, \dots, N$ of s_1 and s_2 . Lag m is set to be $-L \leq m \leq L$, namely for each sample $s_1(n)$, we calculate the absolute differences between $s_1(n)$ and the most adjacent $2L + 1$ samples to $s_2(n)$. The alignment error array, computed for the two synthetic traces in Figure 2.1 with $N = 2001$ and $L = 50$, is shown in Figure 2.2. The known lag sequence $nshift(n)$ calculated from $tshift(n)$ by Equation 2.1 is plotted on top of the

alignment error array in Figure 2.3. Note that the alignment errors are nearly zero along the known lag sequence $nshift(n)$ where $m(n)$ is approximate to $nshift(n)$. There are 101^{2001} paths along $n = 1, 2, \dots, 2001$, among which $nshift(n)$ is the one whose cumulative error summing along its path is the smallest. However, calculating 101^{2001} cumulative errors and finding the smallest one is far beyond the computation ability of a modern computer. Fortunately, DTW can solve it by applying suitable constraints to this optimization problem and therefore reduce computation dramatically.

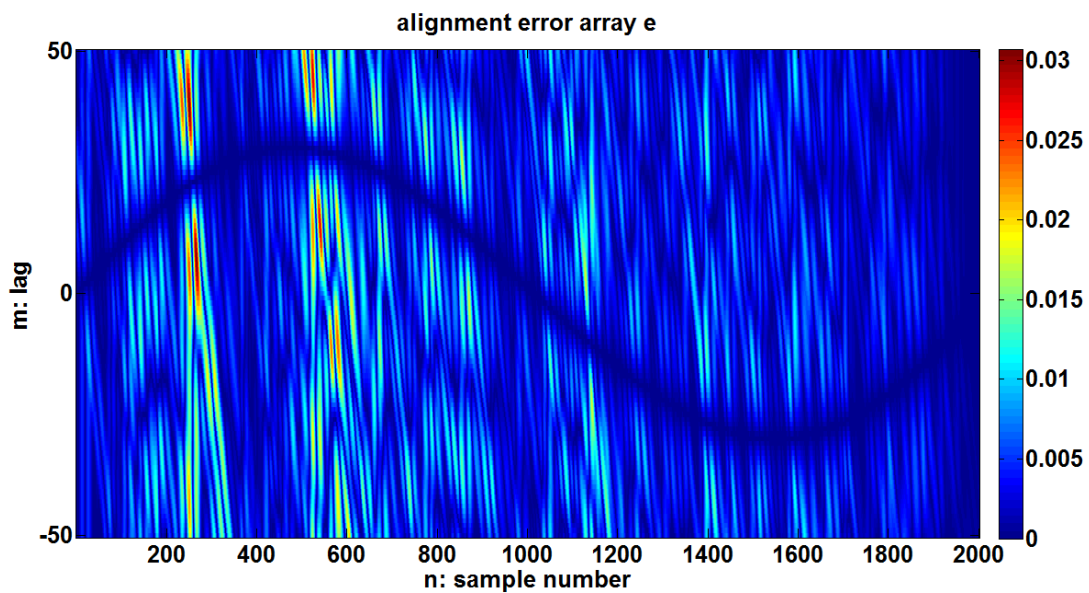


Figure 2.2: Alignment error array where dark blue indicates the error values are small.

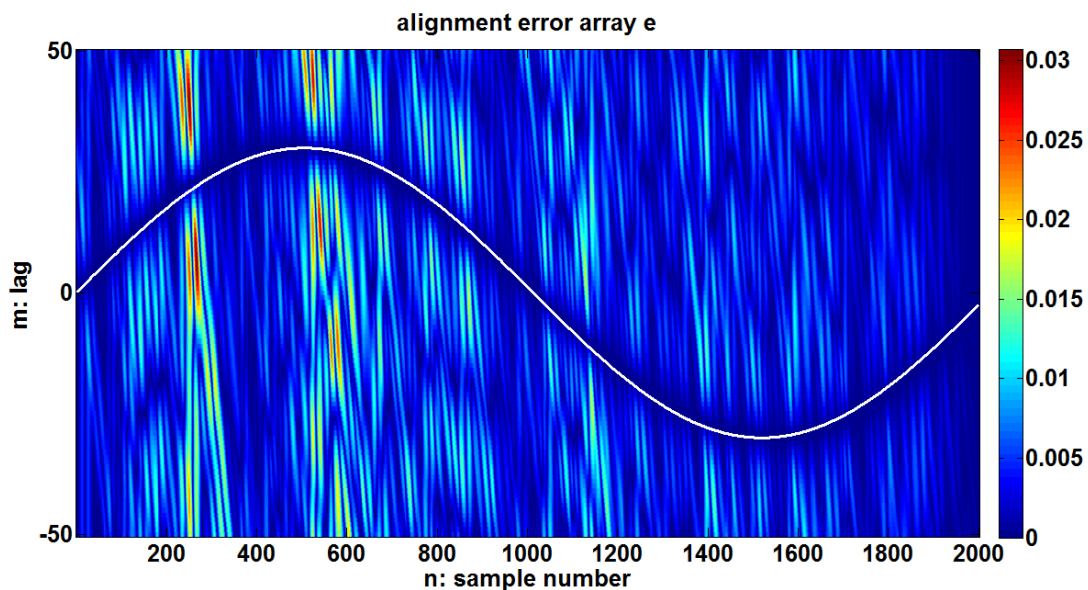


Figure 2.3: The known lag sequence is plotted in white on top of the alignment error array.

2.2.2 Constrained optimization

DTW computes a sequence $u(n) = [u(1), u(2), \dots, u(N)]$ that closely approximates the known lag sequence $nshift(n) = [nshift(1), nshift(2), \dots, nshift(N)]$ by solving the following optimization problem:

$$u(1:N) = \underset{m(1:N)}{\operatorname{arg\,min}} D[m(1:N)], \quad (2.4)$$

where

$$D[m(1:N)] = \sum_{n=1}^N e(n, m(n)) \quad (2.5)$$

subject to the constraint

$$|u(n) - u(n-1)| \leq 1. \quad (2.6)$$

The function D is referred to as total distance which represents the cumulative errors summing along a path from the first sample to the last in the alignment error image shown in Figure 2.2.

Equation 2.4 means that DTW chooses a path $u(1:N)$ to minimize the total distance among the paths satisfying the constraint required by Equation 2.6, the number of which is about 3^N , much smaller than $(2L + 1)^N$ but is still too large. The constraint itself indicates that the lag sequence $u(n)$ cannot change too rapidly from one sample to the next, which is reasonable for the drift time sequence in seismic-to-well ties. When $u(n) - u(n - 1) = 1$, s_2 is stretched such that its two adjacent samples are corresponding to two non-adjacent samples in s_1 with one sample between them. When $u(n) - u(n - 1) = -1$, s_2 is squeezed such that its two adjacent samples are corresponding to only one sample in s_1 .

2.2.3 Dynamic programming

DTW is a dynamic programming algorithm, which decomposes a problem into a sequence of smaller and nested subproblems. Consider a subpath $u(1:k)$ of the minimizing path $u(1:N)$, $u(1:k)$ should satisfy

$$u(1:k) = \arg \min_{m(1:k)} \sum_{n=1}^k e(n, m(n)), \quad (2.7)$$

namely $u(1:k)$ must be a minimizing subpath, or $u(1:N)$ could not minimize D . In other words, $u(1:N)$ is a globally optimal solution of a minimization problem with many possible local minima. According to Equation 2.7, we can further decrease the number of paths we will search from 3^N in two steps: accumulation and backtracking.

In the accumulation step, an array of distances $d(m, n)$ is computed recursively from the array of alignment errors $e(m, n)$ as follows:

$$d(m, 1) = e(m, 1), \quad (2.8)$$

$$d(m, n) = e(m, n) + \min \begin{cases} d(m-1, n-1) \\ d(m, n-1), n = 2, 3, \dots, N. \\ d(m+1, n-1) \end{cases} \quad (2.9)$$

The distance array calculated from the alignment error array in Figure 2.2 is shown in Figure 2.4.

In the backtracking step we calculate the minimizing path $u(1:N)$ starting with the last lag $u(N)$ and ending with the first lag $u(1)$ as follows:

$$u(N) = \arg \min_{-L \leq m \leq L} d(m, N), \quad (2.10)$$

$$u(n) = \arg \min_{m \in \{u(n+1)+1, u(n+1), u(n+1)-1\}} d(m, n), n = N-1, N-2, \dots, 1. \quad (2.11)$$

The computational complexity of the accumulation step is $O((2L+1) \times N)$ and of the backtracking step is $O(N)$, which is easily realized on a personal computer.

The lag sequence $u(n)$ computed by DTW is shown in white on top of the distance array in Figure 2.4. The lag sequence $u(n)$ is represented as time shift sequence $tu(n)$ by

$$tu(n) = u(n) \times dt \quad (2.12)$$

and plotted in Figure 2.5 top panel in red with the known time shift sequence $tshift(n)$ in blue.

We can observe that the time shift sequence calculated from DTW roughly matches the known one except for obvious errors between 0.6 and 1 s. For further study, trace s_1 is warped by the estimated lag sequence $u(n)$ using Equation 2.2 and the time shifted trace (solid blue curve in Figure 2.5 bottom panel) is well tied to s_2 (dotted red curve in Figure 2.5 bottom panel) except for visible discrepancy at about 0.7 s where the estimated time shifts are obviously erroneous.

The maximum crosscorrelation coefficient between them is increased to 0.96 at a decreased lag of 1 milliseconds.

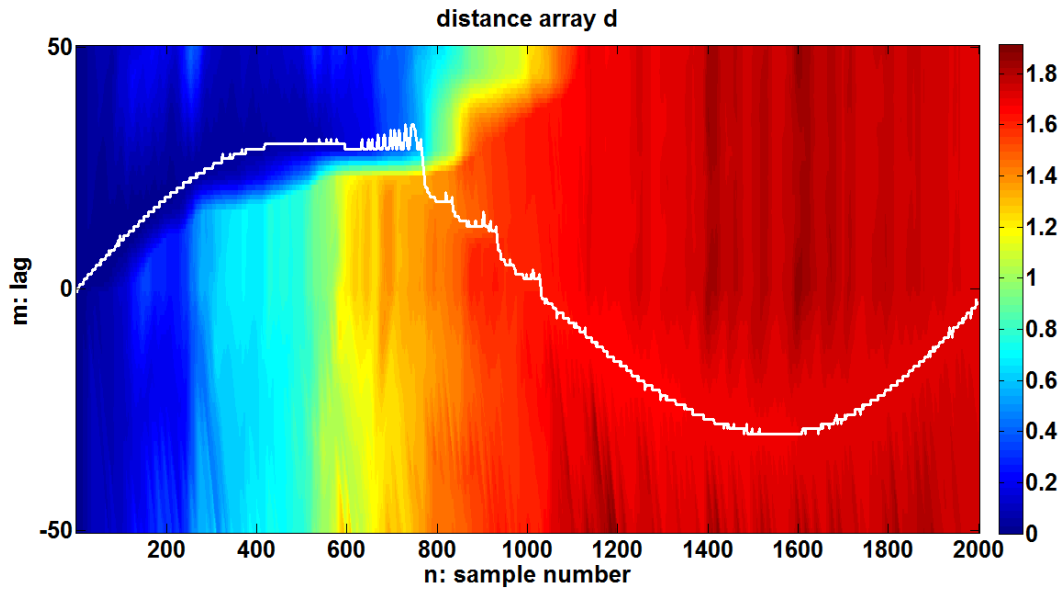


Figure 2.4: Distance array where dark blue indicates the error values are small. The lag sequence calculated by DTW is plotted in white on top of the distance array.

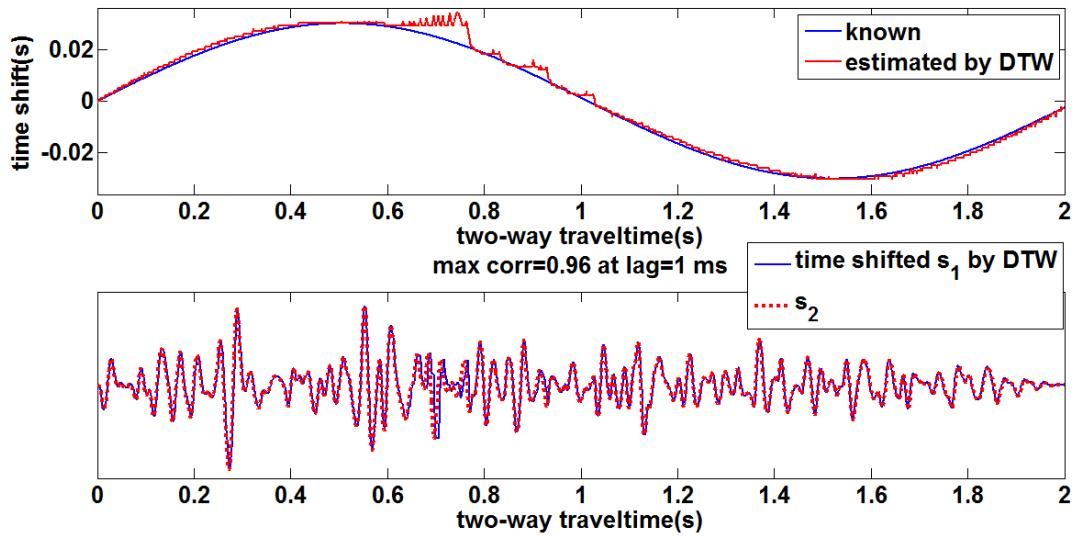


Figure 2.5: Known and DTW estimated time shift sequences (top). Time shifted s_1 by DTW in comparison with s_2 (bottom).

2.3 Smooth dynamic time warping

DTW can roughly estimate the time shifts between two traces, but returns unsmooth integer lags, which are not accurate enough. Figure 2.6 is a zoomed-in version of the alignment error array in Figure 2.2. With constraint Equation 2.6, DTW searches subpaths of only 3 slope values (-1, 0 and 1) shown in red lines, traveling across every two consecutive time samples. Thus, the globally optimal path (dotted white curve) calculated by DTW is the combination of subpaths with these 3 slopes. As we can see, it cannot well approximate the known lag sequence (solid white curve), which is smooth and has multiple slope values between -1 and 1. What is more, when traces s_1 and s_2 are not simply the time-shifted version of each other, the ability of DTW is in doubt to detect such minute time shift changes for every two consecutive time samples, whose interval can be tens times smaller than the time period of seismic events. In seismic-to-well ties, the drift time used to calibrate the timing difference between the sonic logs and the seismic should be smooth and varies slowly with two-way traveltimes to reduce artificial events being introduced in the corrected seismic trace. And seismic traces are not related to synthetic seismograms by time shifts only, but also involve amplitude and phase changes in the presence of anelastic attenuation.

According to Compton and Hale (2013), smooth dynamic time warping (SDTW) can estimate a much smoother time shift sequence with as many possible slopes as required. It is more accurate than DTW especially when two traces are not related by time shifts only, but also have differences in waveforms, noise and etc. Instead of searching 3 possible subpaths at every single time sample, SDTW searches $2h + 1$ possible subpaths of multiple slope values ranging from -1 to 1 at every h^{th} sample. Figure 2.7 shows the same alignment error array and 11 subpaths of different slopes searched for the same sample location by SDTW as Figure 2.6 when

the coarse sampling interval h equals 5 samples. Similar to DTW, alignment errors are then accumulated along each possible linear subpath across h samples, and the subpath with the minimal summation is locally optimal. For a sample on a subpath but at a noninteger lag, its alignment error value is approximated by linearly interpolating the alignment error values of its two vertically adjacent samples. The white circles in Figure 2.7 are the sample locations where the locally optimal subpaths are calculated. By piecewise-linearly interpolating these coarse samples, we obtain the globally optimal path (dotted white curve), which approximates the known lag sequence (solid white curve) much better than the one from DTW. When $h = 1$, SDTW is equal to DTW.

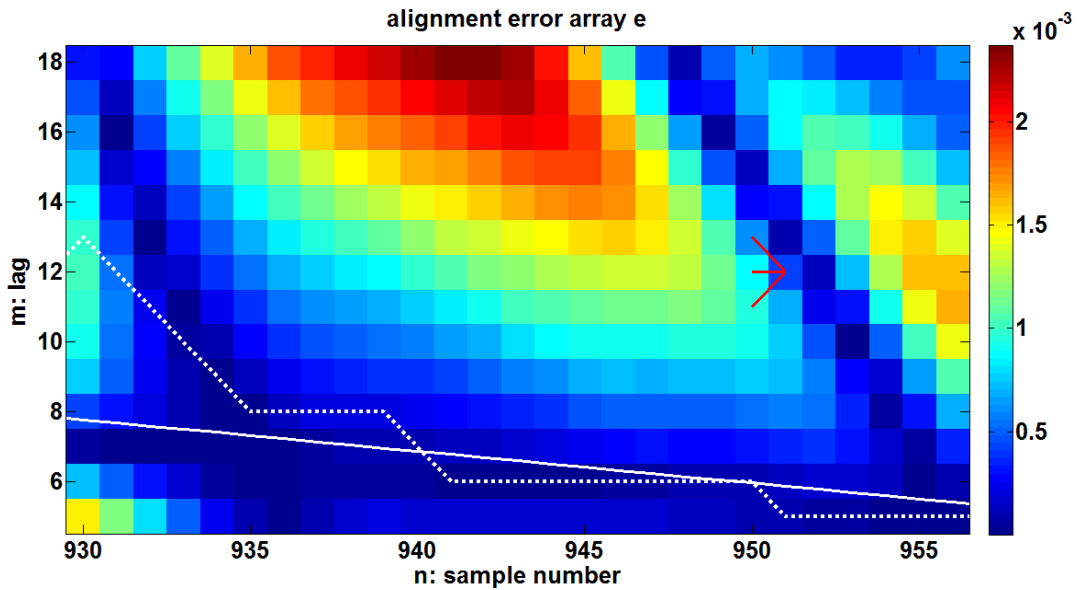


Figure 2.6: Zoomed-in version of alignment error array, on top of which are the 3 subpaths searched for a certain sample location in red lines, the known lag sequence in solid white curve and the estimated lag sequence by DTW in dotted white curve.

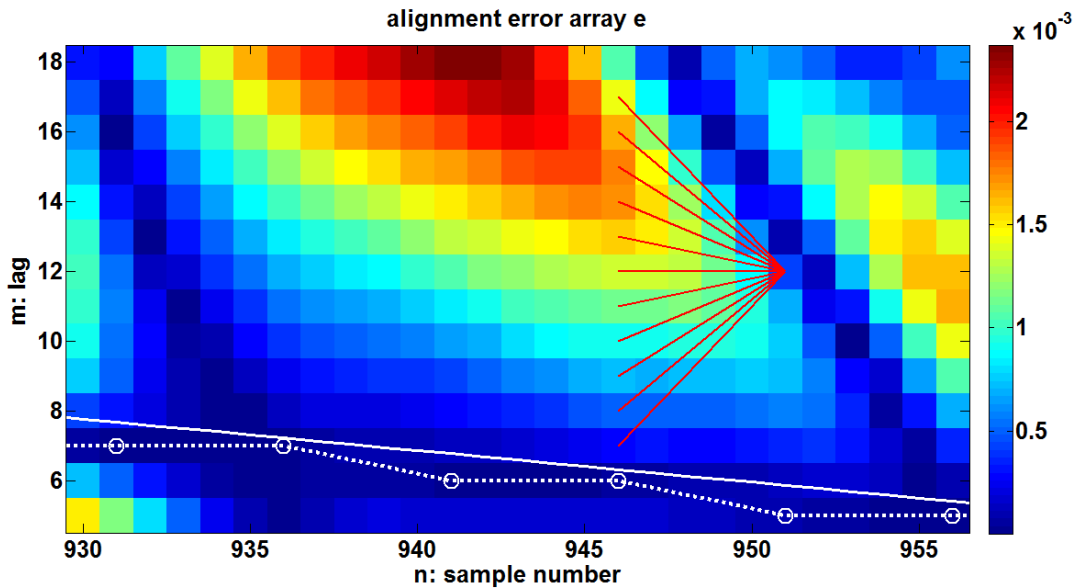


Figure 2.7: Zoomed-in version of alignment error array, on top of which are the 11 subpaths searched for a certain sample location in red lines, the known lag sequence in solid white curve, and the estimated lag sequence by SDTW in dotted white curve with white circles indicating the coarse sample locations where its subpaths are calculated.

SDTW searches locally optimal paths every h samples, ending up with a distance array h times smaller than the one accumulated by DTW, which saves computation time and memory significantly. Numerical tests (not shown here) find that in this case, SDTW does a good job when the value of h is about 100. If h is too small, the estimated time shifts are not smooth enough. If h is too large, the globally optimal path is composed by only limited number of linear subpaths, which cannot well approximate the known time shifts. Furthermore, different distributions of the coarse samples result in similar estimates as long as they are approximately 100 samples apart. Figure 2.8 shows the distance array accumulated by SDTW when $h = 100$. Compared to the distance array calculated by DTW in Figure 2.4, SDTW loses horizontal resolution because it estimates time shifts at coarsely sampled locations only, making the estimated time shift sequence (solid white curve) smoother and more robust when differences

other than time shifts exist between two traces. Figure 2.9 top panel compares the known time shift sequence in solid blue curve, the estimate by SDTW when $h = 100$ in solid red curve with red circles indicating the coarse locations with 100 samples apart where the time shifts are calculated, and the estimate by DTW after being convolved with a normalized Gaussian window with 100 ms half-width in dotted black curve. The time shift sequence estimated by DTW is smoothed and better approximates the known time shifts, but it remains obviously erroneous from 0.6 to 0.8 s. Thus, smoothing the rough time shifts estimated by DTW is not equal to the globally optimal time shifts computed by SDTW. Trace s_1 is warped by the SDTW estimated time shifts using Equation 2.2 and the time shifted trace (solid blue curve in Figure 2.9 bottom panel) is well tied to trace s_2 (dotted red curve in Figure 2.9 bottom panel). The maximum crosscorrelation coefficient between them is 0.98 at a lag of 0.1 milliseconds, indicating a better correlation than the result from DTW in Figure 2.5 bottom panel.

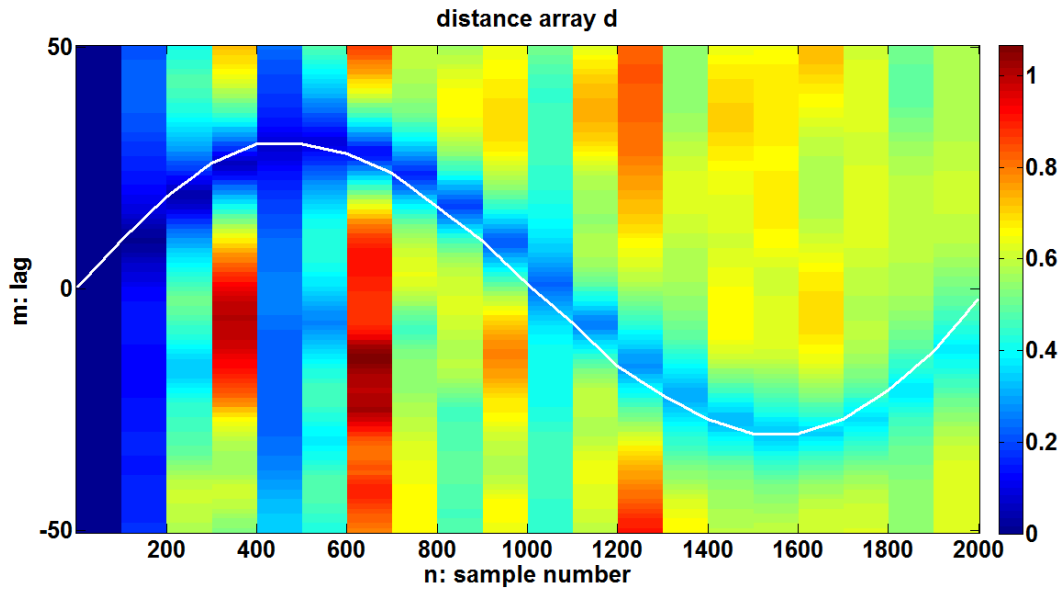


Figure 2.8: Distance array accumulated every 100th sample. The lag sequence calculated by SDTW is plotted in white on top of the distance array.

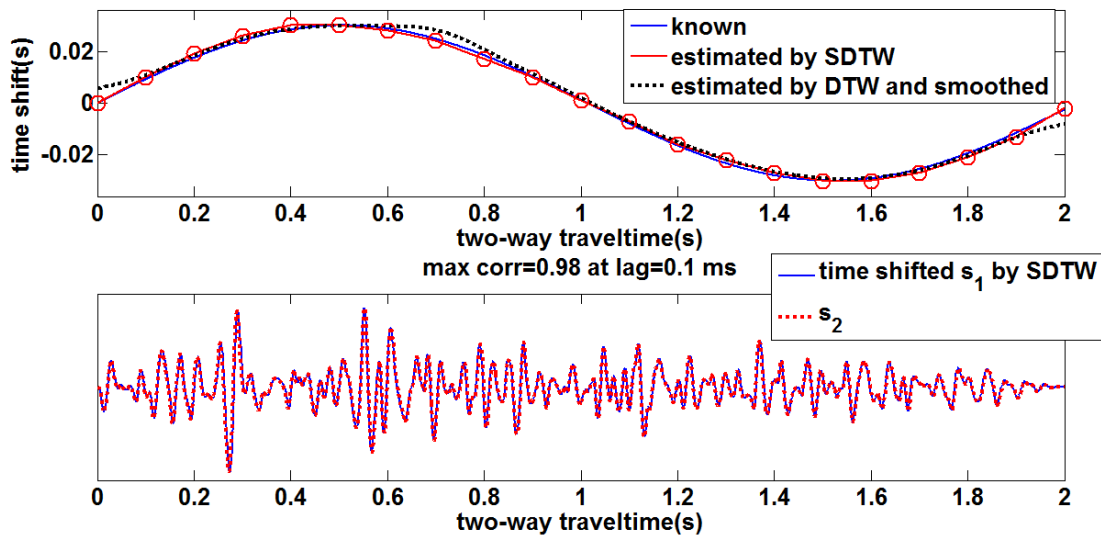


Figure 2.9: Known and estimated time shift sequences (top). Time shifted s_1 by SDTW in comparison with s_2 (bottom).

2.4 Time-variant crosscorrelation

The common method, time-variant crosscorrelation (TVCC) is applied to estimate the time shifts between traces s_1 and s_2 for comparison with DTW and SDTW. Algorithm details are described in Section 1.5.3 using a sinusoid function with a maximum value of 10 ms as the known time shift sequence, which is accurately estimated by TVCC. In this section, the known sinusoid time shift sequence has the maximum value of 30 ms, implying more rapid changes.

Figure 2.10 top panel shows the time shifts estimated by TVCC (dotted red curve) using Gaussian windows with 100 ms half-width and 10 ms increment, in comparison with the known time shifts (solid blue curve). We observe that significant errors and instability occur where the time shift sequence increases or decreases rapidly and their corresponding time-variant crosscorrelation coefficients are also very low shown in Figure 2.10 middle panel. At these time spots, the time shifted trace s_1 (solid blue curve) by the TVCC estimated time shift does not align with trace s_2 (dotted red curve) in Figure 2.10.

TVCC assumes that the time shifts are almost constant within every single Gaussian window. We have to choose a window width, which is small enough, but also has to be larger than the existing time shift to correctly calculate crosscorrelation coefficient. If the time shifts vary rapidly, a suitable window width may not exist and TVCC fails in estimating the time shifts. This is why TVCC succeeds when the known sinusoid time shift sequence has the maximum value of 10 ms but fails when its maximum value is 30 ms. Without windows, DTW or SDTW is more sensitive to the rapidly varying time shifts. Instead of estimating time shifts, this thesis employs TVCC to quantitatively examine the correlation between the synthetic seismogram and the seismic trace in the well tying procedure.

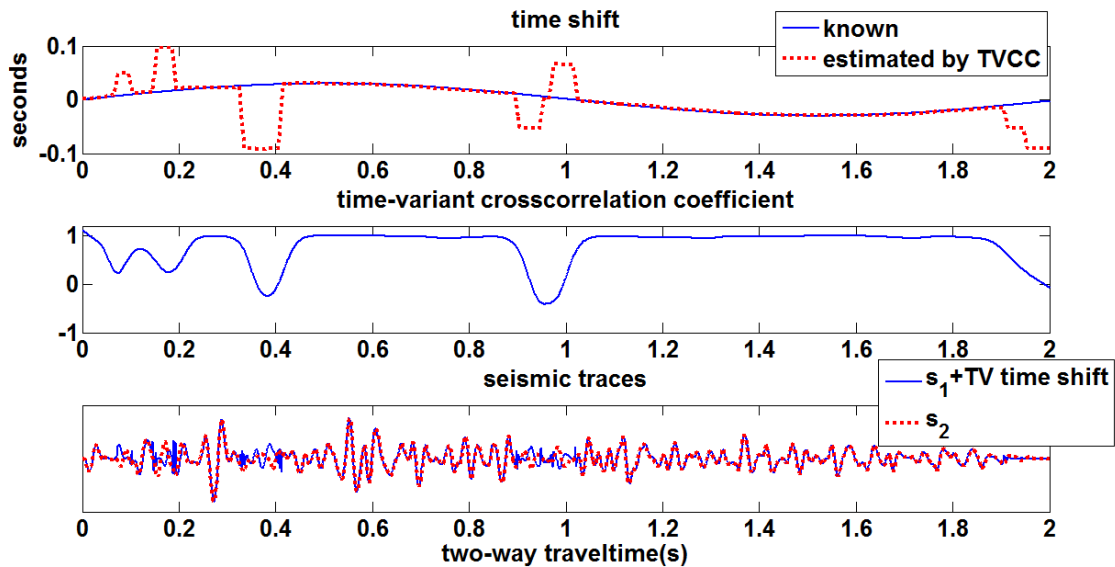


Figure 2.10: The known time shift sequence and its estimate (top). Time-variant crosscorrelation coefficient (middle). Time shifted s_1 compared to s_2 (bottom).

2.5 Summary

- Dynamic time warping can roughly estimate time shifts between two traces automatically to achieve a high correlation between them. But the estimated time shifts are not smooth.
- Smooth dynamic time warping can accurately estimate smooth time shifts between two traces automatically to get a good correlation between them.
- Smoothing the rough time shifts estimated by DTW is not equal to the globally optimal time shifts computed by SDTW.
- Dynamic time warping or smooth dynamic time warping is more sensitive to the rapidly varying time shifts than time-variant crosscorrelation.

Chapter Three: Seismic-to-well ties by stationary deconvolution

3.1 Chapter overview

First, the stationary convolutional model is built to relate the well reflectivity to the seismic trace. Then the frequency domain spiking deconvolution algorithm is illustrated as an example of the stationary deconvolution to estimate the well reflectivity from the seismic trace. Next the stationary convolutional model is extended to nonstationary based on the constant-Q theory. A set of analysis and processing tools aimed to address the nonstationarity is introduced through synthetic examples. Finally, the nonstationary trace model is deconvolved by the standard stationary deconvolution algorithm, followed by the nonstationary analysis and processing to tie the well reflectivity.

3.2 Stationary convolutional model

In a 1-D linear earth, the seismic trace $s(t)$ can be modeled by the convolution of a seismic wavelet $w(t)$ with the earth's reflectivity $r(t)$ (Margrave, 2013a)

$$s(t) = (w \cdot r)(t) \equiv \int_{-\infty}^{\infty} w(t - \tau)r(\tau)d\tau \quad (3.1)$$

where \cdot is the stationary convolution operator. All the physical effects that require the wavelet to evolve such as wavefront spreading, transmission loss, multiples, attenuation, elastic mode conversions and noise are ignored. The stationary convolutional model assumes that the seismic wavelet $w(t)$ does not change with traveltime. Figure 3.1 is an illustration of the convolution of a minimum-phase wavelet, which models the seismic wavelets generated by dynamite or airgun sources, with a reflectivity series to yield a 1-D stationary trace by matrix multiplication. The

waveforms in each column of the Toeplitz matrix are identical and are aligned along the diagonal corresponding to the two-way propagation time.

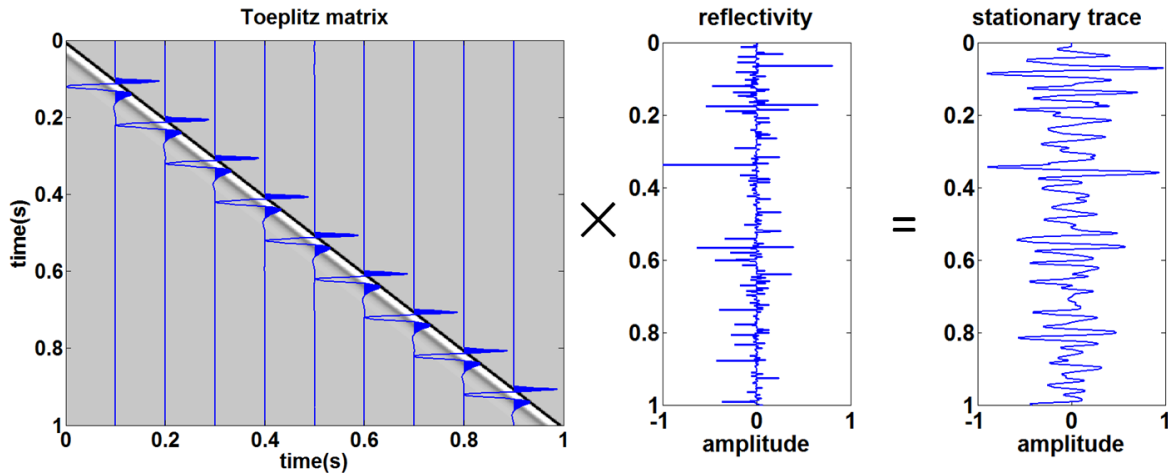


Figure 3.1: The stationary convolutional model is illustrated. The left panel is the Toeplitz matrix in gray, on top of which are wavelets plotted every 0.1 second in blue using wiggle-trace variable-area format. It multiplies a column vector containing a reflectivity series (middle) to produce the stationary trace (right).

3.3 Stationary deconvolution

The ultimate goal of seismic data processing is to estimate the earth's reflectivity, which, theoretically, should be tied to the well reflectivity. This means that the reflectivity estimate from deconvolution should be validated by comparing it to reflectivity calculated directly from well logs. Deconvolution is one of our major tools for achieving this end by separating the seismic wavelet from the reflectivity in the seismic trace. The deconvolution algorithm used in this thesis falls into the blind deconvolution category, meaning that the wavelet to be deconvolved is unknown and must be estimated from the data itself under physically appropriate assumptions about the nature of the reflectivity and the wavelet (Margrave et al., 2011):

- The reflectivity $r(t)$ is a random time series, implying an approximate constant amplitude spectrum at all frequencies.
- The seismic wavelet is a temporally short pulse, implying a smooth Fourier amplitude spectrum. It is causal and invertible and its inverse is causal, implying a minimum phase.
- The seismic wavelet is stationary.

Take the frequency domain spiking deconvolution as an example. The stationary convolutional model in the frequency domain is

$$\hat{s}(f) = \hat{w}(f)\hat{r}(f) \quad (3.2)$$

where $\hat{s}(f)$, $\hat{w}(f)$ and $\hat{r}(f)$ are the complex-valued Fourier spectra of $s(t)$, $w(t)$ and $r(t)$ respectively. The wavelet design portion of the deconvolution algorithm works on the amplitude spectra only. Take the amplitude spectra of Equation 3.2:

$$|\hat{s}(f)| = |\hat{w}(f)||\hat{r}(f)|. \quad (3.3)$$

Figure 3.2 shows the amplitude spectra of the wavelet (red), reflectivity (blue) and seismic trace (green) in decibels. We can see that the amplitude spectral shape of the embedded wavelet is imposed on the seismic trace. This is because the reflectivity is assumed to be statistically white, namely

$$\overline{|\hat{r}(f)|} \approx 1 \quad (3.4)$$

where the overbar denotes the smoothing operation. Thus, we can estimate the amplitude spectrum of the wavelet by smoothing $|\hat{s}(f)|$:

$$|\hat{w}(f)|_{est} = \overline{|\hat{s}(f)|} \approx |\hat{w}(f)| \quad (3.5)$$

where the subscript *est* indicates the estimate. The back curve in Figure 3.2 is the amplitude spectrum of the estimated wavelet by convolving $|\hat{s}(f)|$ with a 10 Hz half-width Gaussian smoother. It well approximates the known wavelet in red curve.

According to the assumption that the phase of the seismic wavelet is minimum, the phase of the wavelet $\varphi_w(f)$ can be computed from its amplitude spectrum via the Hilbert transform

(Margrave, 2013a)

$$\varphi_w(f) = -\frac{1}{\pi} \int_{-\infty}^{\infty} \frac{\ln|\hat{w}(\tilde{f})|_{est}}{f-\tilde{f}} d\tilde{f}. \quad (3.6)$$

In the digital implementation, the integral must be calculated within the seismic frequency band only

$$\varphi_w(f) = -\frac{1}{\pi} \int_{-f_{NYQ}}^{f_{NYQ}} \frac{\ln|\hat{w}(\tilde{f})|_{est}}{f-\tilde{f}} d\tilde{f}, \quad (3.7)$$

where f_{NYQ} is the Nyquist frequency and it equals 250 Hz with a 2 milliseconds sample interval in this numerical test.

Figure 3.3 shows the estimated wavelet (dotted black) on top of the known wavelet (solid red) in the time domain. Their maximum crosscorrelation coefficient is 0.98 at a lag of 0.2 milliseconds, implying an accurate wavelet estimate. Deconvolving the estimated wavelet from the seismic trace, the estimated reflectivity is shown in solid black in comparison with the known reflectivity in solid blue. Their maximum crosscorrelation coefficient is 0.94 at a lag of 0 milliseconds, indicating the standard deconvolution algorithm succeeds in the stationary seismic trace. However, such nearly perfect results are never seen in practice to make seismic-to-well ties trivial (Margrave, 2013c).

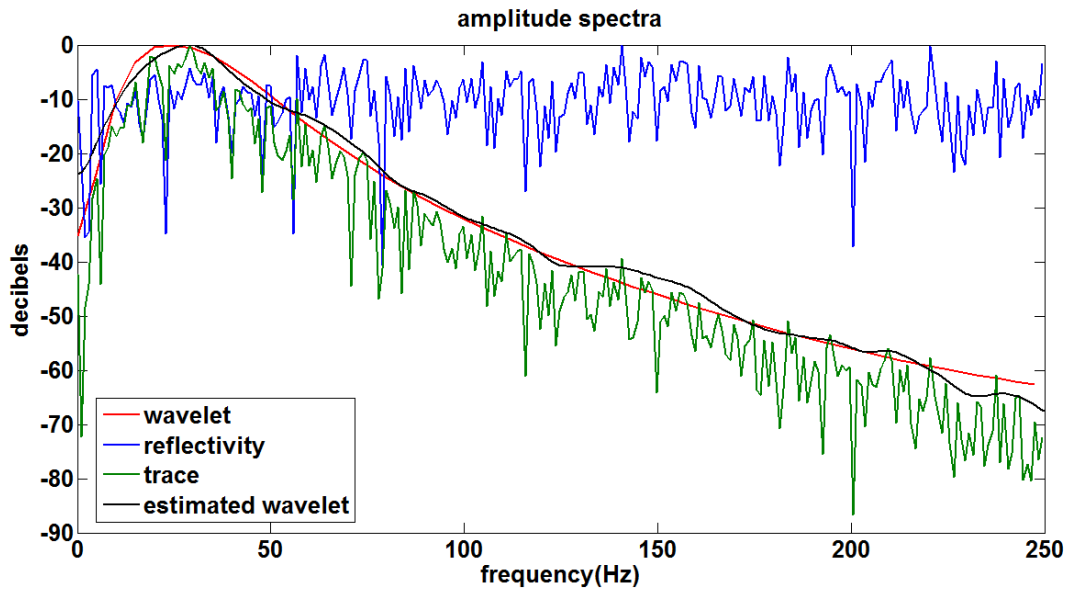


Figure 3.2: Amplitude spectra of the wavelet, reflectivity, seismic trace and the wavelet estimated by the frequency domain spiking deconvolution.

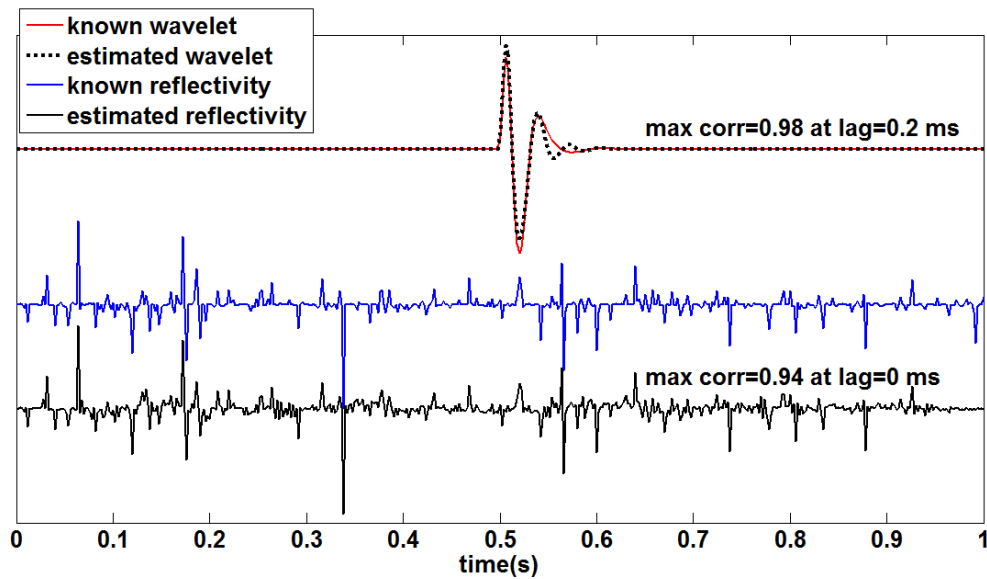


Figure 3.3: The known wavelet (solid red), estimated wavelet (dotted black), known reflectivity (solid blue) and estimated reflectivity (solid black) in the time domain. The wavelets are both delayed by 0.5 seconds for a better display.

3.4 Constant-Q model

In this thesis, the term nonstationary refers to physical processes that cause data variation in both time and frequency. Simpler nonstationary processes that are time variant but not frequency variant, such as wavefront spreading are well handled by standard seismic data processing methods (Margrave, 2013c). The propagating seismic waves always suffer anelastic attenuation, which predicts an exponential amplitude decay in traveltime and frequency associated with minimum-phase dispersion. It is considered as a source of nonstationarity. The constant-Q model (Kjartansson, 1979) is a widely accepted approximation to observed attenuation behaviour. The constant-Q model refers to a Q that is independent of frequency at least over the seismic bandwidth, but may still be a function of position. In the constant-Q theory, the amplitude spectrum of the wavelet approximates to

$$|\widehat{w}_Q(x, f)| \approx |\widehat{w}_0(f)| e^{-\frac{\pi f x}{v_0 Q}} \quad (3.8)$$

where $|\widehat{w}_0(f)|$ is the amplitude spectrum of the source wavelet, $|\widehat{w}_Q(x, f)|$ is the amplitude spectrum of the propagating wavelet which starts as the source wavelet but travels distance x , f is frequency, v_0 is the reference velocity measured at the reference frequency f_0 and Q is a rock property. Letting $\frac{x}{v_0}$ equals traveltime t , Equation 3.8 becomes

$$|\widehat{w}_Q(t, f)| \approx |\widehat{w}_0(f)| e^{-\frac{\pi f t}{Q}}. \quad (3.9)$$

The attenuation is necessarily coupled with minimum phase dispersion (Futterman, 1962). The phase spectrum of the propagating wavelet is

$$\varphi_{w_Q}(x, f) = \varphi_{w_0}(f) - \frac{2\pi f x}{v(f)} \quad (3.10)$$

where $\varphi_{w_Q}(x, f)$ is the phase spectrum after travel distance x , $\varphi_{w_0}(f)$ is the phase spectrum of the source wavelet, and the frequency dependent phase velocity $v(f)$ is given by

$$v(f) = v_0 \left(1 + \frac{1}{\pi Q} \ln \frac{f}{f_0} \right). \quad (3.11)$$

Substituting Equation 3.11 into Equation 3.10, φ_{w_Q} is approximate to

$$\varphi_{w_Q}(t, f) \approx \varphi_{w_0}(f) - 2\pi f t \left(1 - \frac{1}{\pi Q} \ln \frac{f}{f_0} \right). \quad (3.12)$$

Figure 3.4 shows the bandlimited response of the 1-D constant-Q process for various traveltimes in the time domain. The progressive widening waveform and the overall diminishing amplitude indicate the progressive attenuation of high frequencies. Figure 3.5 is the amplitude spectra of the wavelets in Figure 3.4. The blue curve is $|\widehat{w}_0(f)|$ and the others are $|\widehat{w}_Q(t, f)|$ computed by Equation 3.9. The seismic wavelet is observed to have continuously decreasing bandwidth. Figure 3.6 shows that the velocity is dependent on frequency for various Q values according to Equation 3.11. The velocity dispersion is strong for low Q values. The dominant frequency of well logging is about 12.5 kHz while that of seismic exploration is typically below 50 Hz. Thus, the velocities measured by the sonic tool are systematically faster than those experienced by seismic waves. In seismic-to-well ties, synthetic seismograms created with well logging velocities predict events systematically earlier than seismic traces. The traveltime difference due to the discrepancy between seismic and well logging frequencies is called drift time and is always positive.

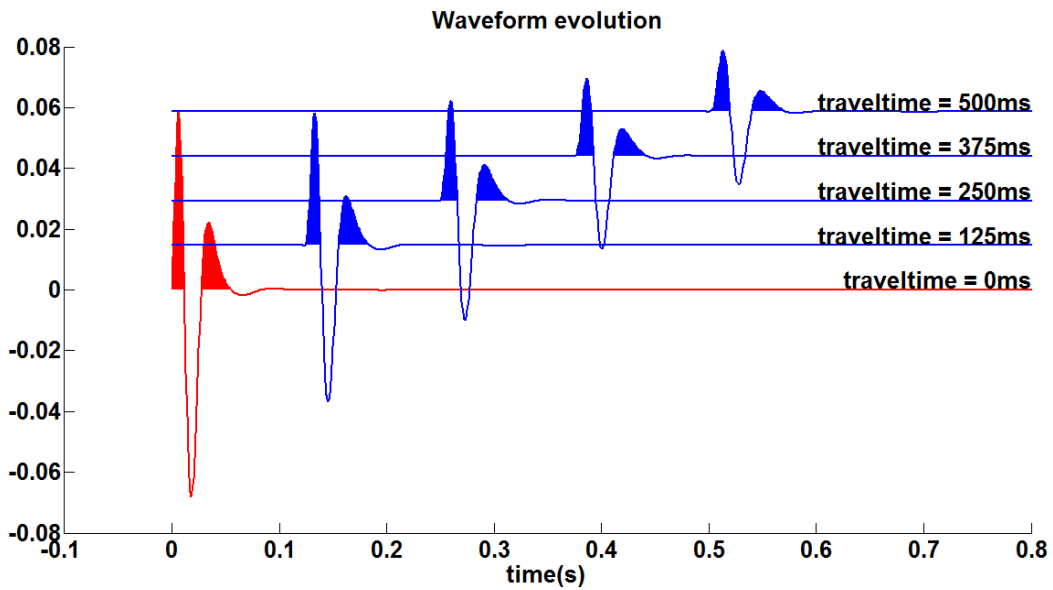


Figure 3.4: A minimum-phase source wavelet with a dominant frequency of 30 Hz (red) is shown after various traveltimes (blue) assuming a Q of 50.

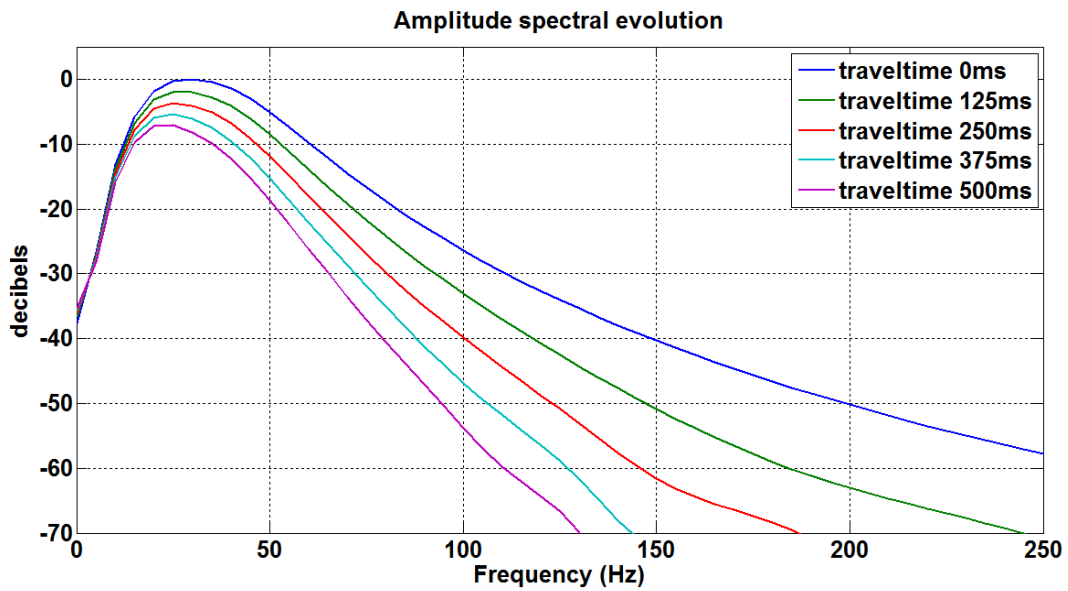


Figure 3.5: Amplitude spectra of the wavelets in Figure 3.4.

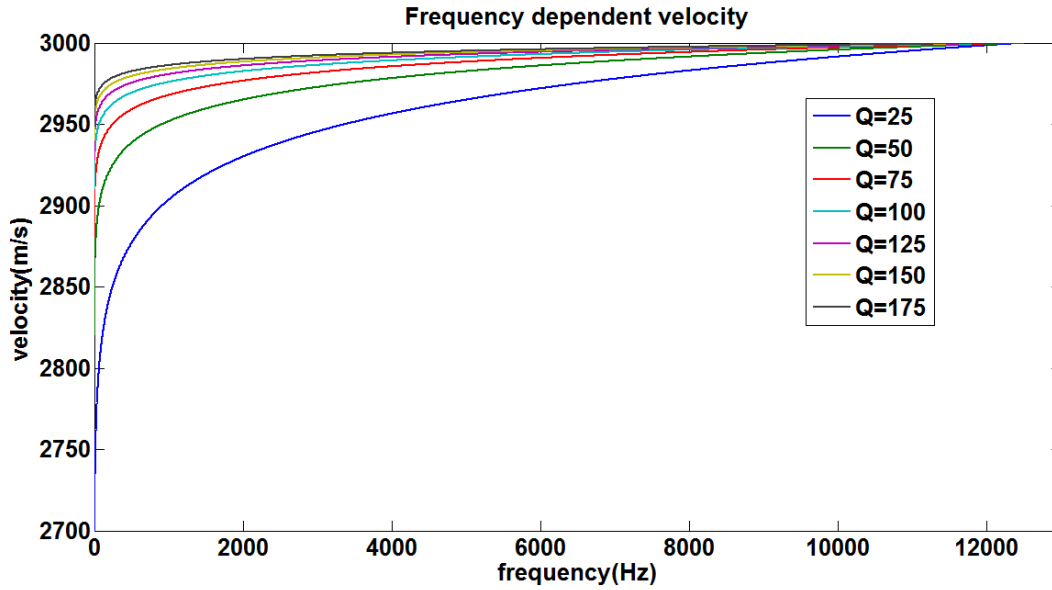


Figure 3.6: The velocity is dependent on frequency for various Q values assuming $v_0 = 3000$ m/s at the well logging frequency of $f_0 = 12.5$ kHz.

3.5 Nonstationary convolutional model

The stationary convolutional model is not valid in the presence of frequency-dependent attenuation. The stationary convolutional model has been extended to nonstationary by Margrave et al. (2011)

$$s(t) = (w_0 \cdot \alpha \odot r)(t) \quad (3.13)$$

where $w_0(t)$ is a minimum-phase source wavelet without attenuation, $\alpha(\tau, t)$ is called the attenuation function, and the symbol \odot is introduced as the nonstationary convolution operator.

Assuming an impulsive source, the 1-D nonstationary seismic response I_r is

$$I_r(t) = (\alpha \odot r)(t) \equiv \int_{-\infty}^{\infty} \alpha(\tau, t - \tau) r(\tau) d\tau. \quad (3.14)$$

Including the effect of the nonimpulsive signature $w_0(t)$ as a stationary convolution with the nonstationary seismic response $I_r(t)$, Equation 3.13 can be written as

$$s(t) = (w_0 \cdot I_r)(t) = \int_{-\infty}^{\infty} w_0(t - \tau) I_r(\tau) d\tau. \quad (3.15)$$

The attenuation function $\alpha(\tau, t)$ is essentially the impulse response of the attenuation process at traveltime τ predicted by the constant-Q theory. In the frequency domain, its amplitude spectrum is

$$|\alpha(\tau, f)| = e^{-\pi f \tau / Q} \quad (3.16)$$

and its phase is minimum for any constant time τ . The propagating wavelet $w_Q(\tau, t)$, which is the source wavelet $w_0(t)$ modified by the attenuation effects after traveltime τ , is

$$w_Q(\tau, t) = (w_0 \cdot \alpha)(\tau, t) \equiv \int_{-\infty}^{\infty} w_0(t - t') \alpha(\tau, t') dt'. \quad (3.17)$$

Equation 3.13 can also be written as the nonstationary convolution of the propagating wavelet with the reflectivity

$$s(t) = (w_Q \odot r)(t) = \int_{-\infty}^{\infty} w_Q(\tau, t - \tau) r(\tau) d\tau. \quad (3.18)$$

The nonstationary convolution forms the linear superposition of a set of progressively attenuated wavelets scaled by the corresponding reflectivity values, which is shown in Figure 3.7.

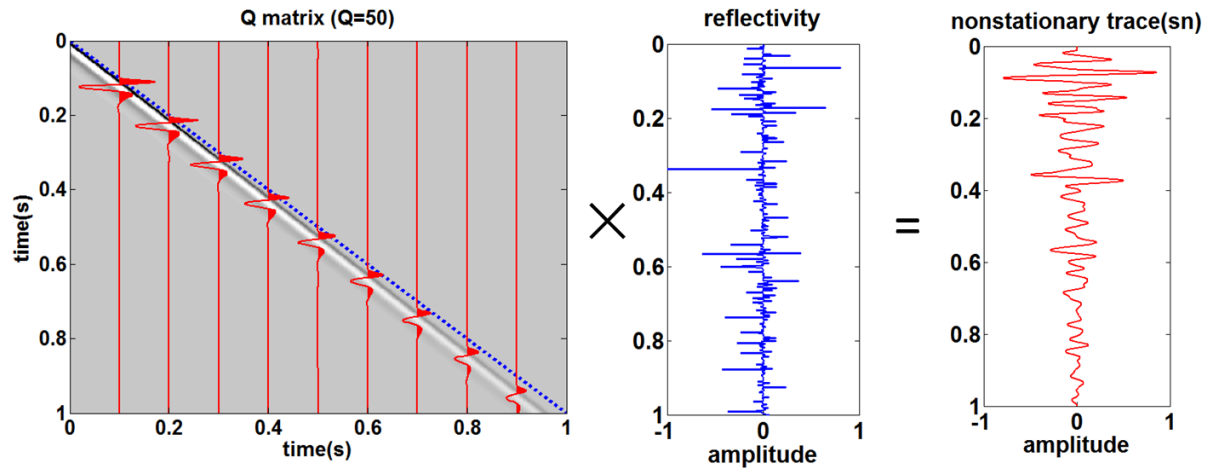


Figure 3.7: The nonstationary convolutional model is illustrated. The left panel is the Q matrix in gray, on top of which are wavelets plotted every 0.1s in red using wiggle-trace variable-area format. The bandlimited evolving wavelets lag behind the dashed blue diagonal by a progressively increasing amount. The Q matrix multiplies a column vector containing a reflectivity series (middle) to produce the nonstationary trace (right).

Figure 3.8 compares the stationary trace in Figure 3.1 and the nonstationary trace in Figure 3.7. In the time domain (top panel), the nonstationary trace agrees with the stationary trace at the beginning, but later shows progressive attenuation effects indicated by the diminishing amplitude, the widening waveforms and the delayed events, compared to the stationary trace. In the frequency domain, the nonstationary trace has less power at high frequencies than the stationary trace.

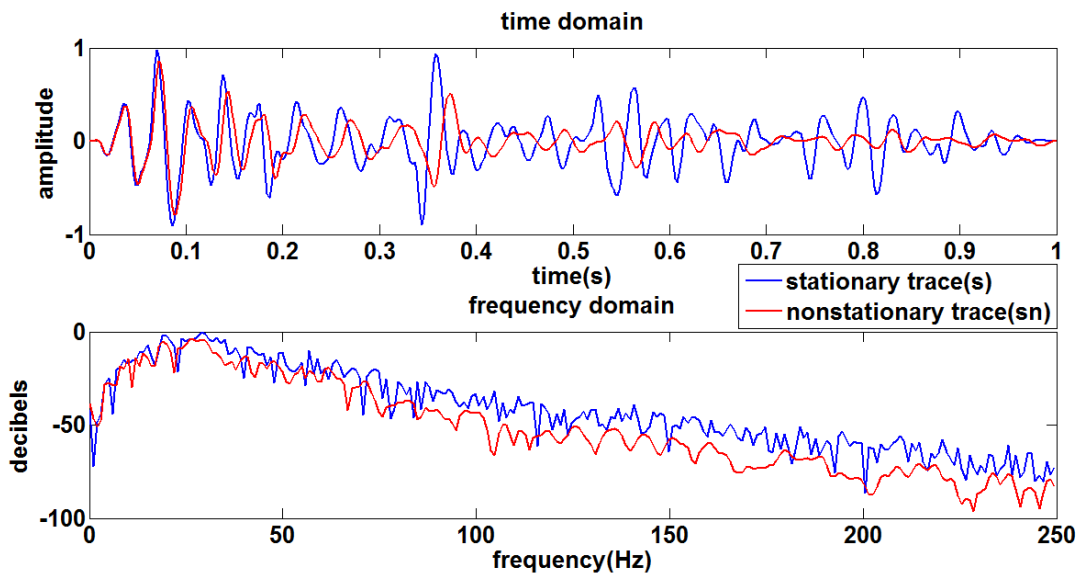


Figure 3.8: Comparison of stationary and nonstationary traces in the time and frequency domains.

3.6 Nonstationary analysis and processing tools

Seismic traces are always nonstationary due to ubiquitous attenuation while synthetic seismograms calculated from well reflectivity are usually stationary. In standard seismic-to-well ties, not only the trace at the well location, but also other hundreds or even thousands of traces are processed by comparing them to a single well reflectivity, in which only very smooth information from the well is used. In this thesis, a set of programs have been adopted to analyze and address the nonstationarity in amplitude, phase and time shift respectively, by comparing the deconvolved nonstationary trace to the well reflectivity within a sliding Gaussian window. This section demonstrates how these tools work through synthetic examples.

3.6.1 Time-variant amplitude balancing

A synthetic seismic trace $s_1(t)$ is plotted in solid blue in Figure 3.9 top panel. Trace $s_2(t)$ is obtained by scaling the amplitude of s_1 with a known time-variant scalar function $scalar(t)$ via

$$s_2(t) = scalar(t) s_1(t) \quad (3.19)$$

and is plotted in dotted red on top of trace s_1 , from which we observe that their amplitudes are different. The scalar function $scalar(t)$ is essentially the absolute value of a sinusoid function and is shown in solid blue in Figure 3.9 bottom panel.

Without knowledge of $scalar(t)$, time-variant (TV) amplitude balancing can estimate it to balance the amplitude of trace s_1 with respect to the reference trace s_2 . The scalar function is estimated by

$$scalar_{est}(\tau) = \frac{RMS[s_2^\sigma(\tau)]}{RMS[s_1^\sigma(\tau)]} \quad (3.20)$$

where $RMS[s_1^\sigma(\tau)]$ is the root mean square value over t of trace $s_1(t)$ windowed by a Gaussian function $g_\sigma(t)$ of standard width 2σ centered at time τ , namely

$$RMS[s_1^\sigma(\tau)] = \sqrt{\int_{-\infty}^{\infty} [s_1(t)g_\sigma(t - \tau)]^2 dt}. \quad (3.21)$$

Similarly,

$$RMS[s_2^\sigma(\tau)] = \sqrt{\int_{-\infty}^{\infty} [s_2(t)g_\sigma(t - \tau)]^2 dt}. \quad (3.22)$$

In this case, the Gaussian window is chosen to have a half-width (σ) of 200 ms and an increment between adjacent windows of 10 ms. The estimated scalar function $scalar_{est}(t)$ is plotted in dotted red in Figure 3.9 bottom panel, which approximates the known one but appears smoother.

Next trace s_1 is balanced by $scalar_{est}(t)$ through Equation 3.19 and is plotted in solid black in

Figure 3.9 top panel, on top of which the reference trace s_2 is plotted again in dotted red. We see their amplitudes are much more similar after TV amplitude balancing of trace s_1 . Inherent in this and other methods in this section is that the effects we are correcting are very slowly time variant.

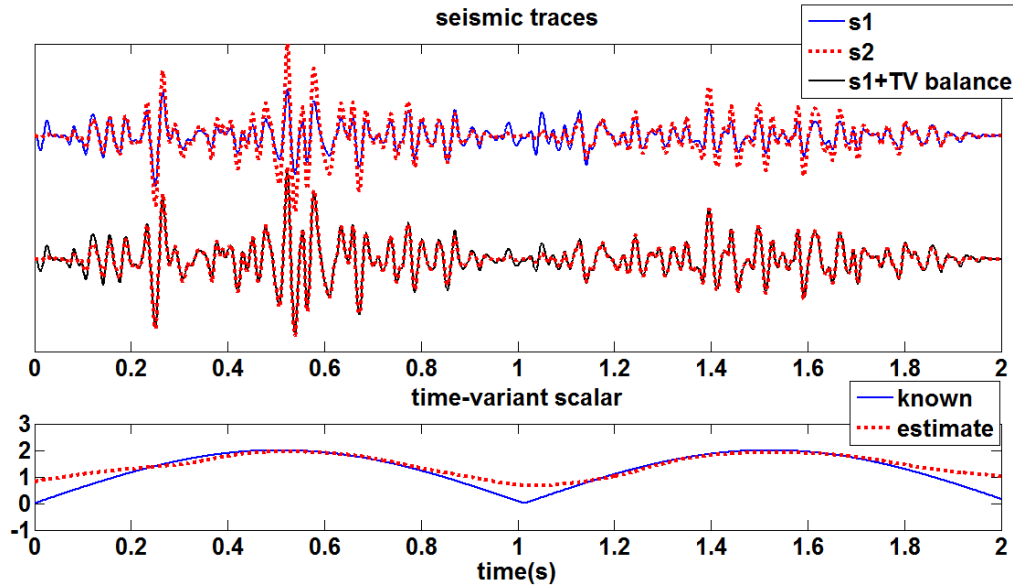


Figure 3.9: Time-variant amplitude balancing is illustrated. Seismic traces with and without time-variant balancing compared to the reference trace (top). The known time-variant scalar function and its estimate (bottom).

3.6.2 Time-variant constant-phase rotation and estimation

A synthetic seismic trace $s_1(t)$ is plotted in solid blue in Figure 3.10 top panel. Trace $s_2(t)$ is obtained by rotating the phase of s_1 with a known time-variant constant-phase function $\vartheta(t)$ via

$$s_2(t) = \cos\vartheta(t) s_1(t) + \sin\vartheta(t) s_1^\perp(t) \quad (3.23)$$

where $s_1^\perp(t)$ is 90 degree phase-rotated trace s_1 (Barnes, 2007). Here the constant phase means the phase is independent of frequency. Trace $s_2(t)$ is plotted in dotted red on top of trace s_1 ,

from which we observe that they do not match each other. The time-variant constant-phase $\vartheta(t)$ is essentially a sinusoid function and is shown in solid blue in Figure 3.10 bottom panel.

The time-variant constant-phase function $\vartheta(t)$ can be estimated by solving the optimization problem

$$\vartheta_{est}(\tau) = \underset{\theta \in -180:179}{arg\ min} \text{RMS}[s_1^{\sigma,\theta}(\tau) - s_2^\sigma(\tau)] \quad (3.24)$$

where $s_1^{\sigma,\theta}$ is the windowed trace s_1^σ rotated by a phase angle θ . Equation 3.24 means that the phase ϑ at time τ is estimated by applying a series of constant phases θ ranging from -180 to 179 degrees in 1 degree increment to the windowed trace s_1^σ and choosing the optimal phase angle to minimize the RMS errors between $s_1^{\sigma,\theta}$ and s_2^σ . In this case, the Gaussian window is chosen to have a half-width of 200 ms and an increment of 10 ms. The estimated time-variant constant-phase $\vartheta_{est}(t)$ is plotted in dotted red in Figure 3.10 bottom panel, which approximates the known one. Next trace s_1 is rotated by $\vartheta_{est}(t)$ through Equation 3.23 and is plotted in solid black in Figure 3.10 top panel, on top of which the reference trace s_2 is plotted again in dotted red. We see now they are tied to each other.

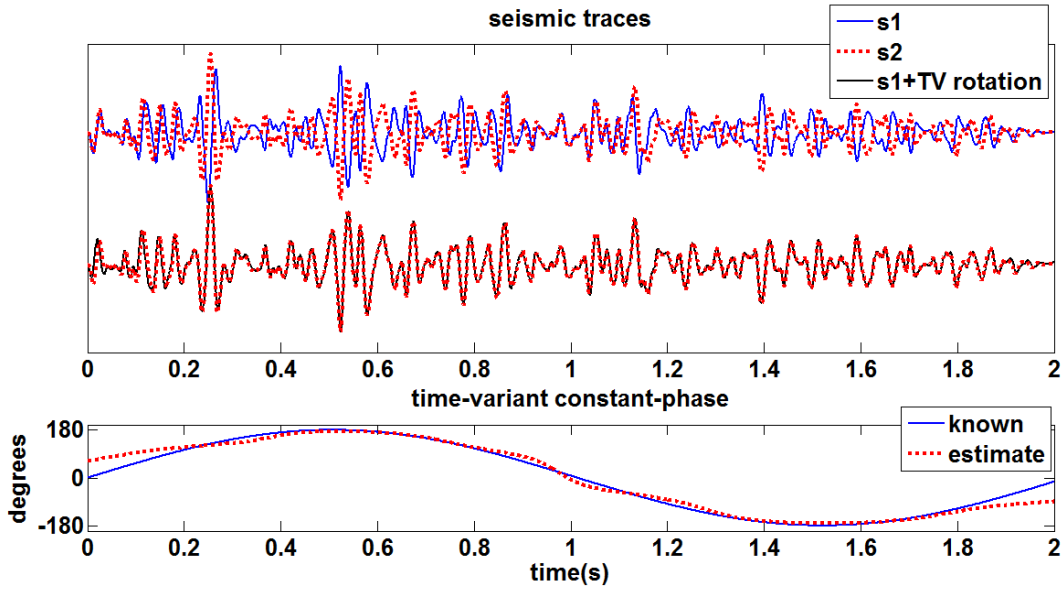


Figure 3.10: Time-variant constant-phase rotation and estimation are illustrated. Seismic traces before and after time-variant constant-phase rotation compared to the reference trace (top). The known time-variant constant-phase function and its estimate (bottom).

3.6.3 Time-variant crosscorrelation

A synthetic seismic trace $s_1(t)$ is plotted in solid blue in Figure 3.11 top panel. Trace $s_2(t)$ is obtained by shifting the time of s_1 with a known time shift function $tshift(t)$ via Equation 2.2 and is plotted in dotted red on top of trace s_1 , from which we observe that trace s_2 is delayed at early times and is advanced at late times compared to trace s_1 . The known time shift sequence is essentially a sinusoid function with the maximum value of 10 ms and is shown in solid blue in Figure 3.11 middle panel. Without knowledge of $tshift$, time-variant crosscorrelation (TVCC) can estimate it at every Gaussian window center time τ via

$$tshift_{est} = \underset{t}{arg\ max} (s_1^\sigma \otimes s_2)(t) \quad (3.25)$$

where \otimes denotes crosscorrelation over time t . Equation 3.25 means that trace s_1 is windowed by a sliding Gaussian function of standard width 2σ centered at time τ and the estimated time shift

corresponding to τ is the time lag at which the crosscorrelation coefficient between s_1^σ and s_2 is maximum. In this case, the Gaussian window is chosen to have a half-width of 100 ms and an increment of 10 ms. The estimated time shift function $tshift_{est}$ is plotted in dotted red in Figure 3.11 middle panel, which well approximates the known one. Next the time of trace s_1 is shifted by $tshift_{est}(t)$ through Equation 2.2 to get trace s_1^s and is plotted in solid black in Figure 3.11 top panel, on top of which the reference trace s_2 is plotted again in dotted red. We see now they are aligned to each other.

The time-variant crosscorrelation coefficient at time τ between s_1^s and s_2 is calculated by

$$cc = (s_1^{s,\sigma} \otimes s_2^\sigma)(t)|_{t=0} \quad (3.26)$$

where $s_1^{s,\sigma}$ is the time shifted trace s_1^s windowed by the same sliding Gaussian function as the one used to estimate the time-variant time shift sequence. Equation 3.26 means that trace s_1 after time shift and s_2 are windowed by the same sliding Gaussian function and the time-variant crosscorrelation coefficient corresponding to every Gaussian window center time is calculated between $s_1^{s,\sigma}$ and s_2^σ at the zero lag. Figure 3.11 bottom panel exhibits the calculated time-variant crosscorrelation coefficient function, whose value is nearly 1 along the whole travelttime, indicating good alignment between trace s_1 after time shift and trace s_2 .

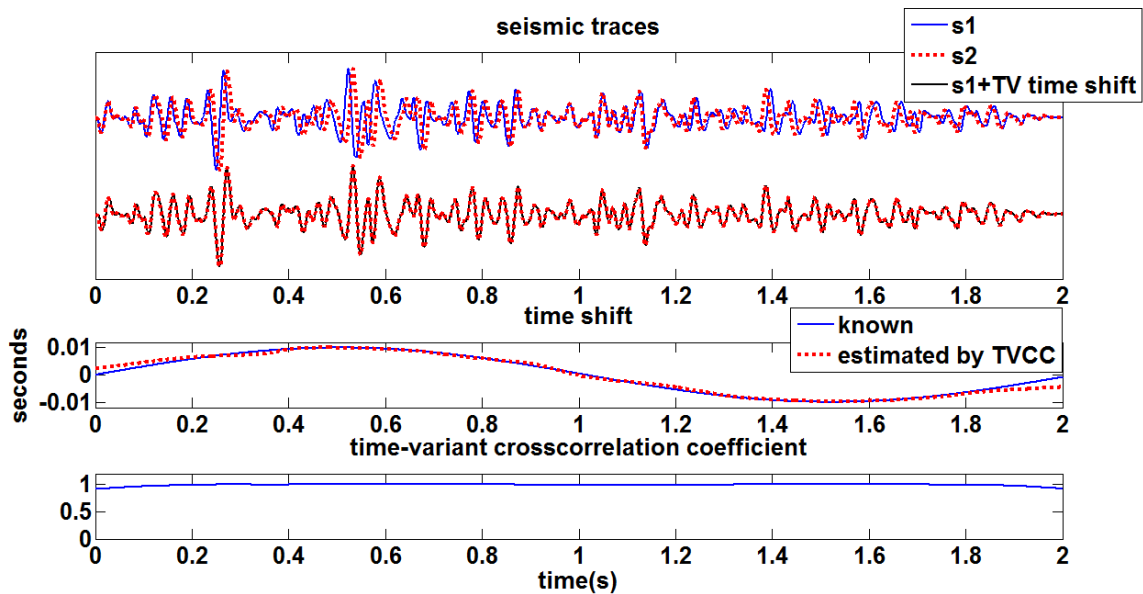


Figure 3.11: Time-variant crosscorrelation is illustrated. Seismic traces before and after time-variant time shift compared to the reference trace (top). The known time-variant time shift function and its estimate (middle). Time-variant crosscorrelation coefficient (bottom).

3.7 Stationary deconvolution on the nonstationary seismic trace

While the field recorded traces are always nonstationary because some attenuation is always present, they are usually deconvolved by the stationary deconvolution algorithm to tie the well reflectivity in the industrial practice. To simulate this process, the frequency domain spiking deconvolution is run on the nonstationary trace in Figure 3.7. The deconvolution parameters are the same as those used for the stationary trace except that an average wavelet is estimated within an imaginary target zone by windowing the nonstationary trace with a 100 ms half-width Gaussian function centered at 0.5 s, which is short enough to assume that the wavelet evolution is small within it. The Gaussian function is displayed in Figure 3.12. Figure 3.13 compares the amplitude spectra of the estimated wavelet (dotted red) with the source wavelet (solid blue), the propagating wavelet at 0.5 s (solid green) and at 1 s (solid black) extracted from the Q matrix in

Figure 3.7. The estimated wavelet is seen to best approximate the propagating wavelet traveling to the middle time of the deconvolution operator design window. Next the stationary deconvolution algorithm calculates the numerical inverse of this estimated wavelet and applies this inverse to the entire nonstationary trace, resulting in the catastrophic deconvolved trace shown as the green curve in Figure 3.12. The nonstationary catastrophe, named by Margrave (2013c), is the consequence of using a single wavelet to deconvolve all the evolving wavelets embedded in the nonstationary trace. Figure 3.14 shows the amplitude spectra of three different sections of the deconvolved trace in decibels. The 0.4 – 0.6 s section is within the design window and is properly whitened. However, the earlier section (0 – 0.2 s) is “overwhitened” meaning that its high frequencies are erroneously exaggerated, while the later section (0.8 – 1 s) is “underwhitened” meaning that its embedded wavelets are insufficiently collapsed and will give an underresolved seismic image.

Since there is an obvious amplitude imbalance on the deconvolved trace, time-variant (TV) amplitude balancing is applied to it with respect to the known reflectivity using a sliding Gaussian window with 200 ms half-width and 10 ms increment. Figure 3.12 shows the deconvolved trace after balancing in black. Although its amplitude is balanced in time, its spectral content is still nonstationary. Finally, the time-variant (TV) constant-phase difference, which is assumed to be a first order approximation to the phase errors, is detected between the known reflectivity and its estimate using a sliding Gaussian window with 200 ms half-width and 10 ms increment. Figure 3.15 top panel shows the detected phase difference in black, which gets as large as 180 degrees at some time points and is highly nonstationary along the traveltime. The amplitude balanced estimate is finally rotated by this phase difference in the same time-variant way and is shown in red in Figure 3.12. For a quality check, the time-variant (TV) constant-

phase difference is measured again between the known reflectivity and its estimate after phase rotation and is plotted in red in Figure 3.15 top panel.

To quantitatively examine the well tying procedure, the time-variant crosscorrelation (TVCC) coefficient is measured between the known reflectivity and its estimate at every well-tying step using a sliding Gaussian window with 200 ms half-width and 10 ms increment. Due to the limitation of the TVCC algorithm which is discussed in detail in Section 2.3, the estimated time shift sequences are not precise enough in the presence of a few discontinuities, but the general trends are trustable. It can be observed from Figure 3.15 middle and bottom panels that the crosscorrelation coefficient between the nonstationary trace and the reflectivity decreases while the corresponding time shift increases with two-way traveltime due to the progressive attenuation. After running the stationary deconvolution on the nonstationary trace, their crosscorrelation coefficient is enhanced especially within the design window and the corresponding time shift drops. However, the coefficient is still small and nonstationary, and the time shift still increases with traveltime because all the wavelets remain minimum-phase after deconvolution. After time-variant constant-phase rotation, there is still nonstationary residual phase in the rotated trace and its crosscorrelation coefficient with the well reflectivity decreases, implying that the phase errors after deconvolution are more complex than those that can be corrected by time-variant constant-phase rotation. To conclude, running stationary deconvolution on the nonstationary trace results in imbalanced amplitude, nonstationary spectral content and erroneous phase compared to the well control, which cannot be properly addressed by the nonstationary analysis and processing tools described in Section 1.5.

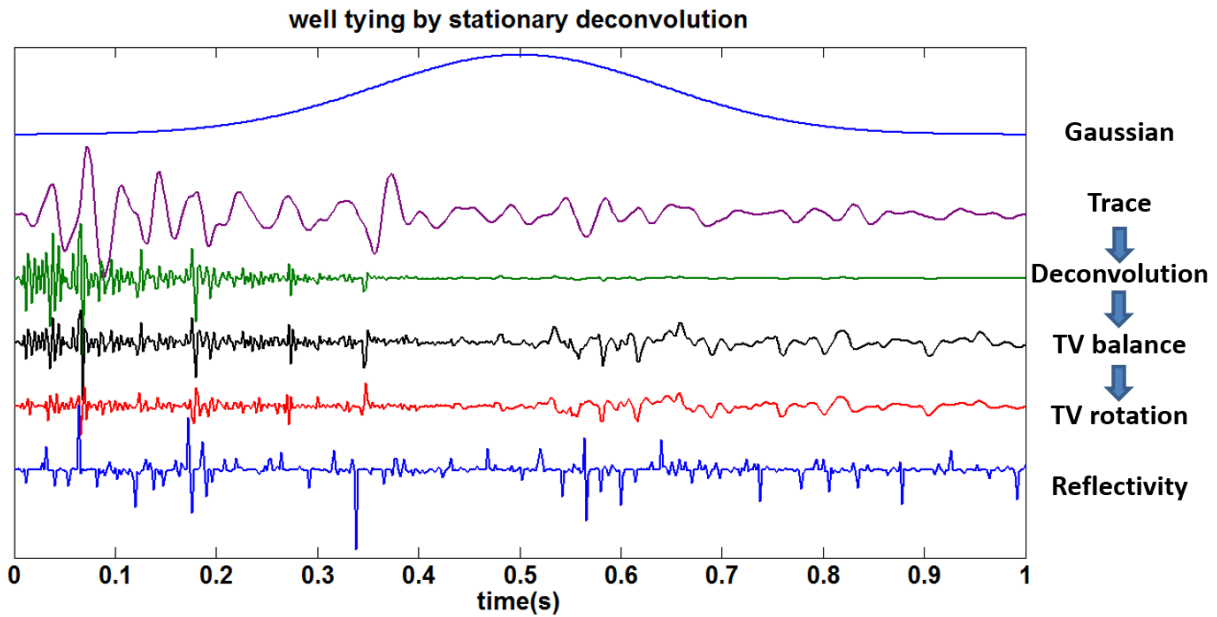


Figure 3.12: A procedure of tying the nonstationary trace to the known reflectivity by stationary deconvolution, time-variant amplitude balancing and time-variant constant-phase rotation.

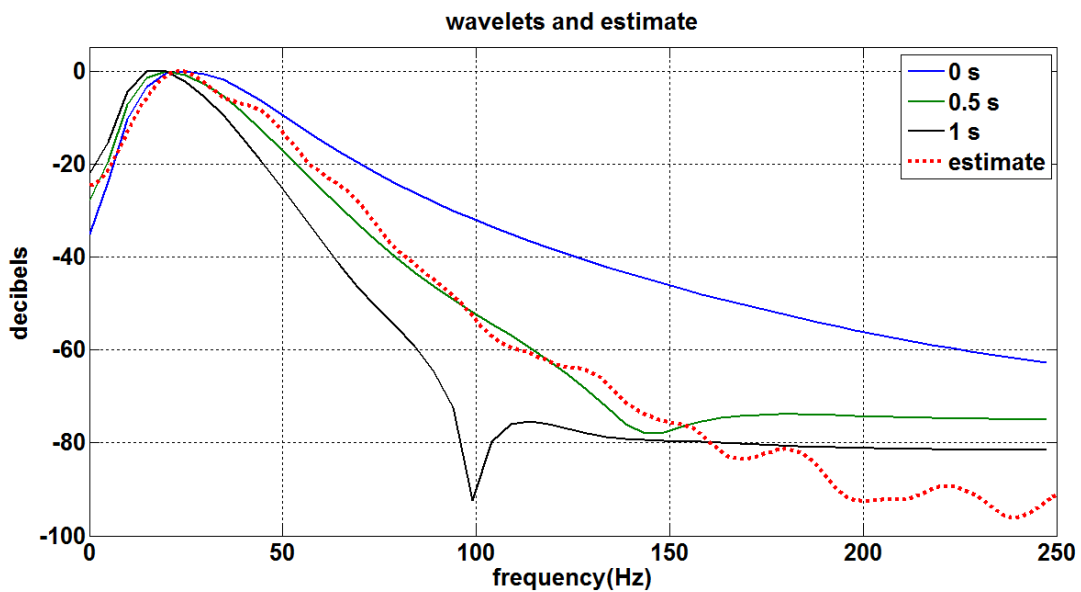


Figure 3.13: The estimated wavelet in comparison with the embedded evolving wavelets propagating to different traveltimes in the frequency domain.

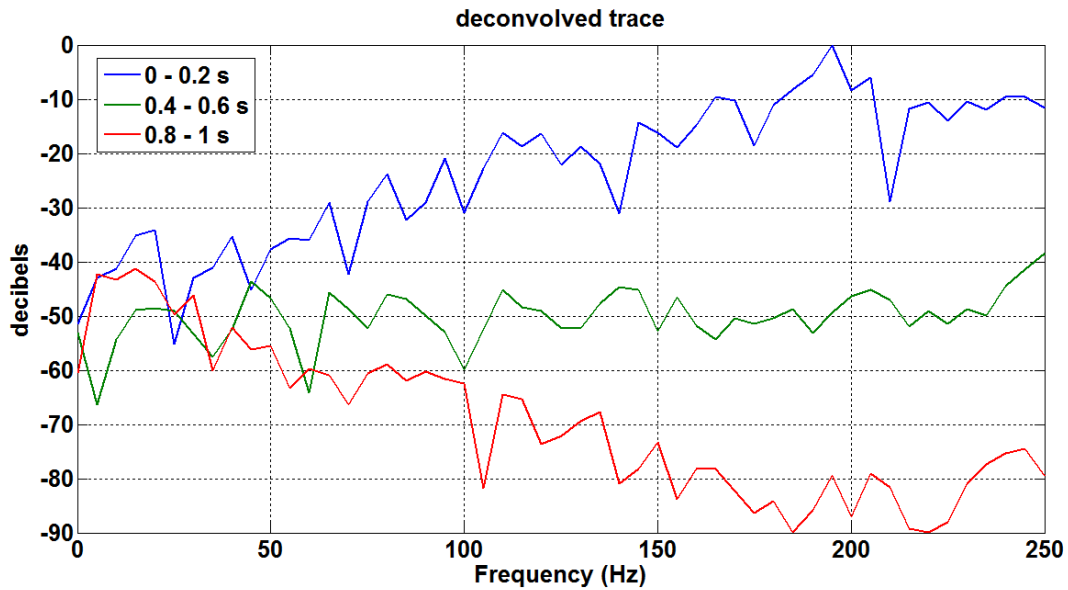


Figure 3.14: Amplitude spectra of the deconvolved seismic trace within different time ranges in decibels.

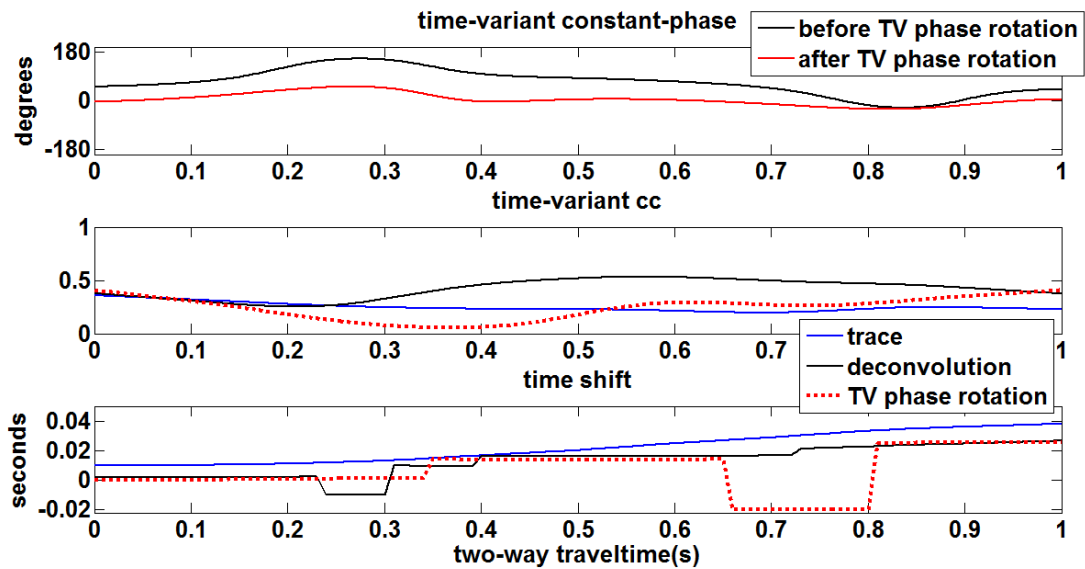


Figure 3.15: The time-variant constant-phase differences between the known reflectivity and the deconvolved trace before and after phase rotation (top). The time-variant crosscorrelation coefficient sequences between the known reflectivity and the nonstationary trace, the deconvolved trace after time-variant amplitude balancing, the deconvolved trace after time-variant amplitude balancing and time-variant constant-phase rotation (middle). The time-variant time shift sequences at which the coefficients are obtained (bottom).

3.8 Summary

- Stationary deconvolution on a stationary seismic trace can estimate an accurate wavelet and eliminate it to tie the well reflectivity.
- The constant-Q theory predicts seismic wavelet evolution with amplitude decay and minimum phase dispersion.
- The nonstationary seismic trace is the linear superposition of a set of progressively attenuated wavelets scaled by the corresponding reflectivity values.
- Compared to the stationary trace, the nonstationary trace shows progressive attenuation effects such as the diminishing amplitude, the widening waveforms and the delayed events.
- By comparing two traces within a sliding Gaussian window, time-variant amplitude balancing, time-variant constant-phase rotation and time-variant crosscorrelation can correct nonstationary effects that are very slowly time variant.
- Stationary deconvolution on a nonstationary seismic trace results in large amplitude and phase errors, resulting from deconvolving a single wavelet estimated within a target zone from the nonstationary trace with embedded evolving wavelets. These errors are nonstationary and difficult to be corrected for by time-variant amplitude balancing and time-variant constant-phase rotation compared to the well control.

Chapter Four: Seismic-to-well ties by Gabor deconvolution

4.1 Chapter overview

First, a nonstationary deconvolution algorithm named Gabor deconvolution is illustrated. Then the residual phase in the Gabor deconvolved trace is investigated and a phase correction operator is developed knowing the Q values and the well logging frequency. Finally, residual drift time after Gabor deconvolution is estimated by smooth dynamic time warping as an alternate way of phase correction without knowledge of Q or the well logging frequency.

4.2 Gabor deconvolution

Margrave and Lamoureux (2001) extend the stationary deconvolution theory to the nonstationary case using the Gabor transform, which is essentially a windowed Fourier transform. The forward Gabor transform decomposes a 1-D temporal signal $s(t)$ onto a 2-D time-frequency spectrum by windowing the signal with a set of Gaussian functions summing to unity and Fourier transforming:

$$\hat{s}_g(\tau, f) = \int_{-\infty}^{\infty} s(t) g_{\sigma}(t - \tau) e^{-2\pi i f t} dt \quad (4.1)$$

where $g_{\sigma}(t - \tau)$ is a Gaussian function of standard width 2σ centered at time τ and $\hat{s}_g(\tau, f)$ is the complex-valued Gabor spectrum of $s(t)$. Given $\hat{s}_g(\tau, f)$, the inverse Gabor transform recreates the signal via 2-D integration over the time-frequency plane:

$$s(t) = \int_{-\infty}^{\infty} \int_{-\infty}^{\infty} \hat{s}_g(\tau, f) e^{2\pi i f t} df d\tau. \quad (4.2)$$

Figure 4.1 shows the forward Gabor transform of the nonstationary trace using a set of Gaussian windows with 100 ms half-width (σ) and 10 ms increment, every 10th of which is plotted in the middle panel. The right panel is the magnitude of its Gabor spectrum, showing that the

nonstationary trace contains the greatest power at early times and low frequencies and the rapid fluctuations are attributed to the reflectivity. The inverse Gabor transform of the 2-D spectrum reconstructs the nonstationary trace, which is consistent with the original one shown in the left panel.

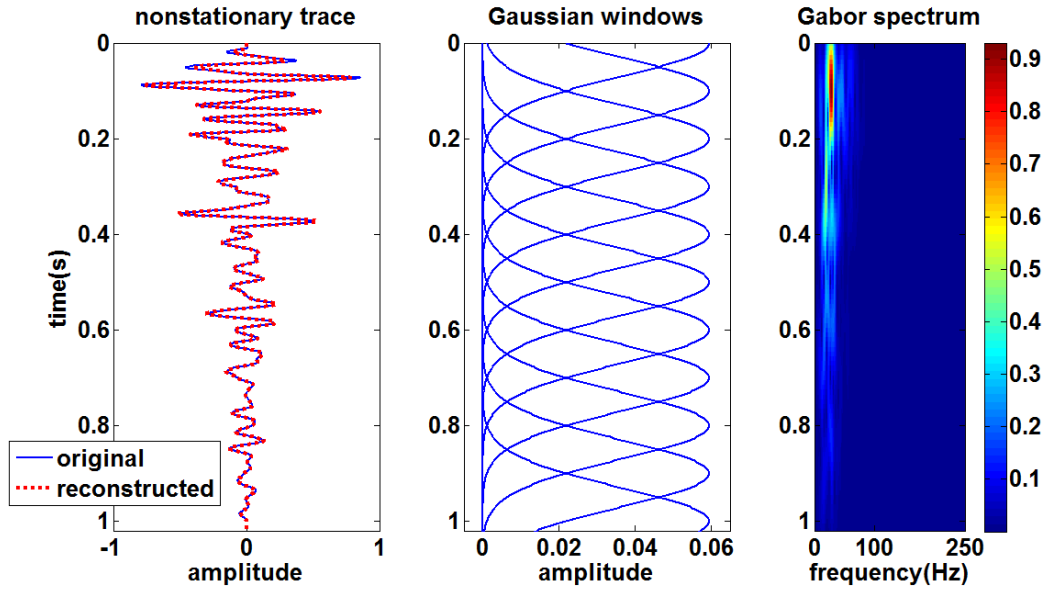


Figure 4.1: The forward and inverse Gabor transform is demonstrated. The nonstationary trace after forward and inverse Gabor transform is on top of the original trace (left). A set of selected Gaussian windows used for the forward Gabor transform (middle). The Gabor magnitude spectrum of the nonstationary trace (right).

Margrave and Lamoureux (2001) derived that the Gabor transform of the nonstationary convolutional model of Equation 3.13 can be approximated as

$$\hat{s}_g(\tau, f) \approx \widehat{w}_0(f)\alpha(\tau, f)\hat{r}_g(\tau, f) \quad (4.3)$$

where $\widehat{w}_0(f)$ is the Fourier transform of the source wavelet $w_0(t)$ and $\hat{r}_g(\tau, f)$ is the Gabor transform of the reflectivity $r(t)$. The Fourier transform of the propagating wavelet in Equation 3.17 is

$$\widehat{w}_Q(\tau, f) = \widehat{w}_0(f)\alpha(\tau, f). \quad (4.4)$$

Therefore, Equation 4.3 can also be written as

$$\hat{s}_g(\tau, f) \approx \widehat{w}_Q(\tau, f)\hat{r}_g(\tau, f). \quad (4.5)$$

Equation 4.5 shows that within a single Gaussian window which is centered at time τ and is narrow enough, the stationary convolutional model is locally valid. Thus, in the frequency domain, the windowed trace is the product of the nonstationary wavelet propagating to time τ and the windowed reflectivity. Figure 4.2 displays the magnitude of each component on the right hand side of Equation 4.3. The source wavelet is a time-invariant function. The attenuation function consists of seamless hyperbolic trajectories with the time and frequency axes as asymptotes. The reflectivity varies rapidly in both time and frequency. Figure 4.3 left panel is the pointwise product of those three components and it well approximates the Gabor magnitude spectrum of the nonstationary trace shown in Figure 4.3 right panel, validating the nonstationary convolutional model factorization in the Gabor domain. Figure 4.4 left panel shows the pointwise product of the Gabor magnitude spectra of the source wavelet and the attenuation function to form the Gabor magnitude spectrum of the propagating wavelet by Equation 4.4.

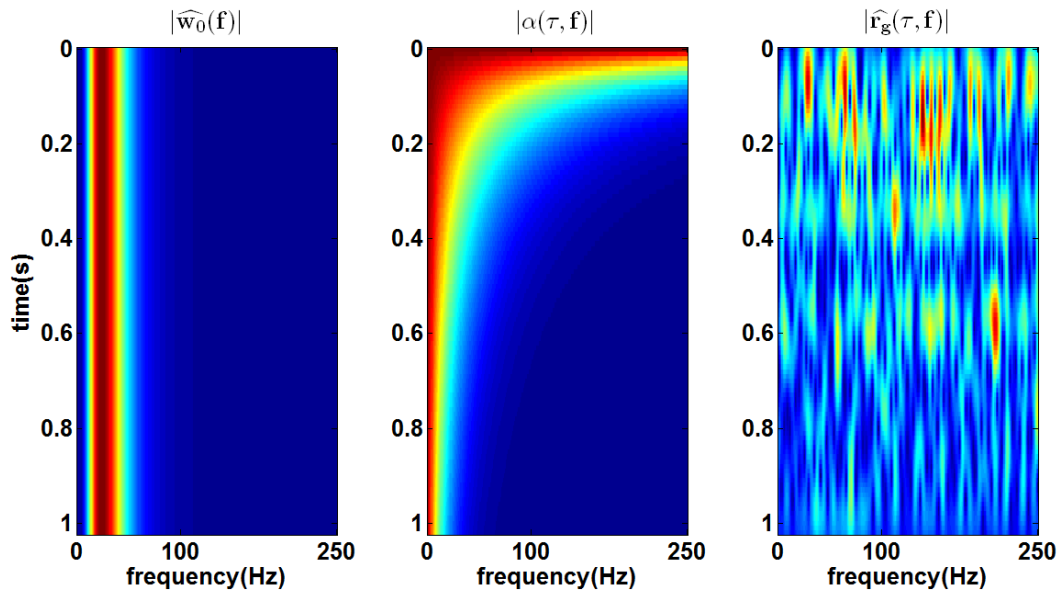


Figure 4.2: The magnitude of three components: the Fourier transform of the source wavelet duplicated along the travelttime (left), the attenuation function represented on the time-frequency plane (middle) and the Gabor spectrum of the reflectivity (right).

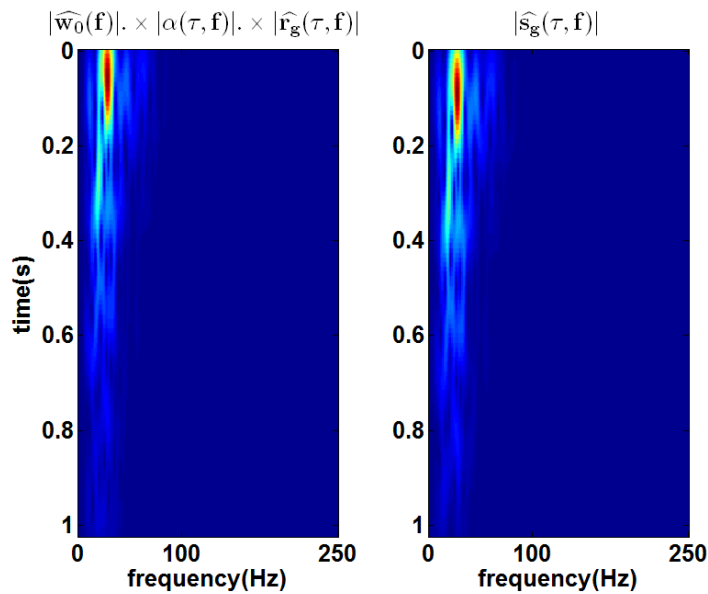


Figure 4.3: The pointwise product of the three magnitude spectra in Figure 4.2 (left) and the Gabor magnitude spectrum of the nonstationary trace (right), which is the same as Figure 4.1 right panel.

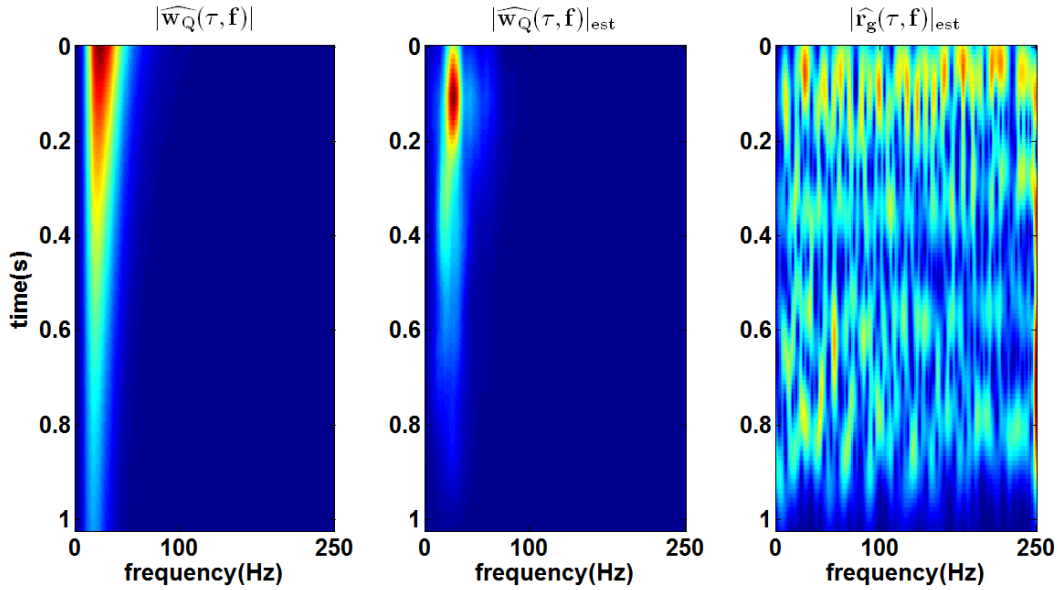


Figure 4.4: The Gabor magnitude spectra of the propagating wavelet (left), the estimated propagating wavelet (middle) and the estimated reflectivity (right) by Gabor deconvolution.

In analogy with the stationary deconvolution, estimating $\hat{r}_g(\tau, f)$ needs the spectral factorization of $\hat{s}_g(\tau, f)$ into two unknown parts: the propagating wavelet and the reflectivity. This can be solved based on the fact that $|\widehat{w}_Q(\tau, f)|$ is relatively smooth compared to the rapidly varying $|\hat{r}_g(\tau, f)|$. Thus, they can be estimated by a spectral smoothing process without knowing or estimating Q values. Similar to the stationary deconvolution, the wavelet design portion of Gabor deconvolution works on the amplitude spectra only and determines the wavelet phase spectrum based on the minimum-phase assumption. Take the absolute values of Equation 4.5:

$$|\hat{s}_g(\tau, f)| \approx |\widehat{w}_Q(\tau, f)| |\hat{r}_g(\tau, f)|. \quad (4.6)$$

The simplest Gabor deconvolution algorithm estimates $|\widehat{w}_Q(\tau, f)|$ by smoothing $|\hat{s}_g(\tau, f)|$ via convolving it with a 2-D boxcar over τ and f

$$|\widehat{w}_Q(\tau, f)|_{est} = |\widehat{s}_g(\tau, f)|. \quad (4.7)$$

Since both the source wavelet and the attenuation function are assumed to be minimum-phase, the phase of the nonstationary wavelet $\varphi_{w_Q}(\tau, f)$ at a constant time τ is also minimum and is calculated by the Hilbert transform

$$\varphi_{w_Q}(\tau, f) = -\frac{1}{\pi} \int_{-\infty}^{\infty} \frac{\ln|\widehat{w}_Q(\tau, \tilde{f})|_{est}}{f - \tilde{f}} d\tilde{f}. \quad (4.8)$$

In the digital implementation, the integral must be calculated within the seismic frequency band only

$$\varphi_{w_Q}(\tau, f) = -\frac{1}{\pi} \int_{-f_{NYQ}}^{f_{NYQ}} \frac{\ln|\widehat{w}_Q(\tau, \tilde{f})|_{est}}{f - \tilde{f}} d\tilde{f}. \quad (4.9)$$

Next $\widehat{r}_g(\tau, f)$ is estimated by dividing $\widehat{w}_Q(\tau, f)_{est}$ from $\widehat{s}_g(\tau, f)$ and $r_{est}(t)$ is got by inverse Gabor transforming $\widehat{r}_g(\tau, f)_{est}$.

Figure 4.4 middle panel shows the Gabor magnitude spectrum of the estimated propagating wavelet by convolving the Gabor magnitude spectrum of the nonstationary trace in Figure 4.3 right panel with a 2-D boxcar of dimensions 0.2 s by 10 Hz. The estimate approximates the known propagating wavelet in Figure 4.4 left panel. Figure 4.4 right panel shows the Gabor magnitude spectrum of the estimated reflectivity by pointwise division of Figure 4.4 middle panel from Figure 4.3 right panel. It approximates the known reflectivity in Figure 4.2 right panel to achieve a strong broadband whitening.

After the inverse Gabor transform, the nonstationary trace after Gabor deconvolution is shown in the time domain as the green curve in Figure 4.5. There is no nonstationary catastrophe and the reflectivity is well resolved. The amplitude spectra of its three sections are plotted in Figure 4.6, showing the appropriate whitening of all the sections. Next, the amplitude of the

Gabor deconvolved trace is balanced and its phase is rotated with respect to the known reflectivity in the same time-variant way as the well tying procedure by the stationary deconvolution. In this case, the time-variant amplitude balancing changes little of the deconvolved trace because the smoothing process does a kind of AGC (automatic gain correction) and simultaneously gains the trace in time. Figure 4.5 shows the final estimate in red on top of the known reflectivity in blue. It can be observed that they roughly tie in amplitude and spectral content but not the phase and/or timing. The time-variant constant-phase differences, crosscorrelation coefficient sequences and time shift sequences are also shown in Figure 4.7 as a quality control. It can be seen that the results at every well-tying step are similar to the case of running the stationary deconvolution. In conclusion, running Gabor deconvolution on the nonstationary trace can get reflectivity estimate tying the well reflectivity in amplitude and spectral content, but has phase errors which are more complex than those that can be solved by time-variant constant-phase rotation.

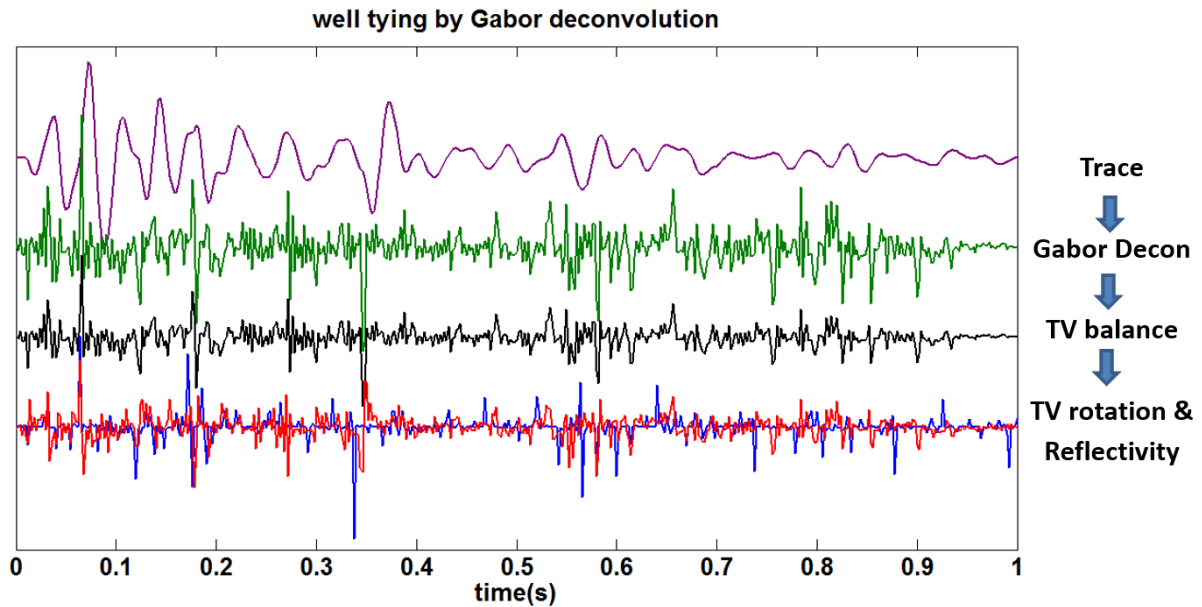


Figure 4.5: A procedure of tying the nonstationary trace to the known reflectivity (blue) by Gabor deconvolution, time-variant amplitude balancing and time-variant constant-phase rotation.

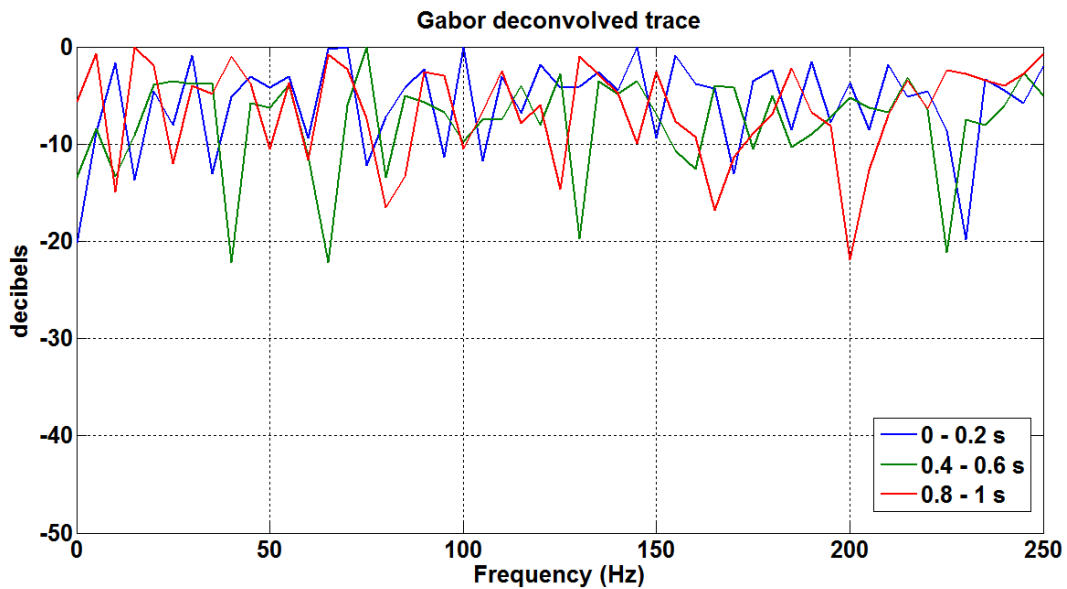


Figure 4.6: Amplitude spectra of the Gabor deconvolved seismic trace within different time ranges in decibels.

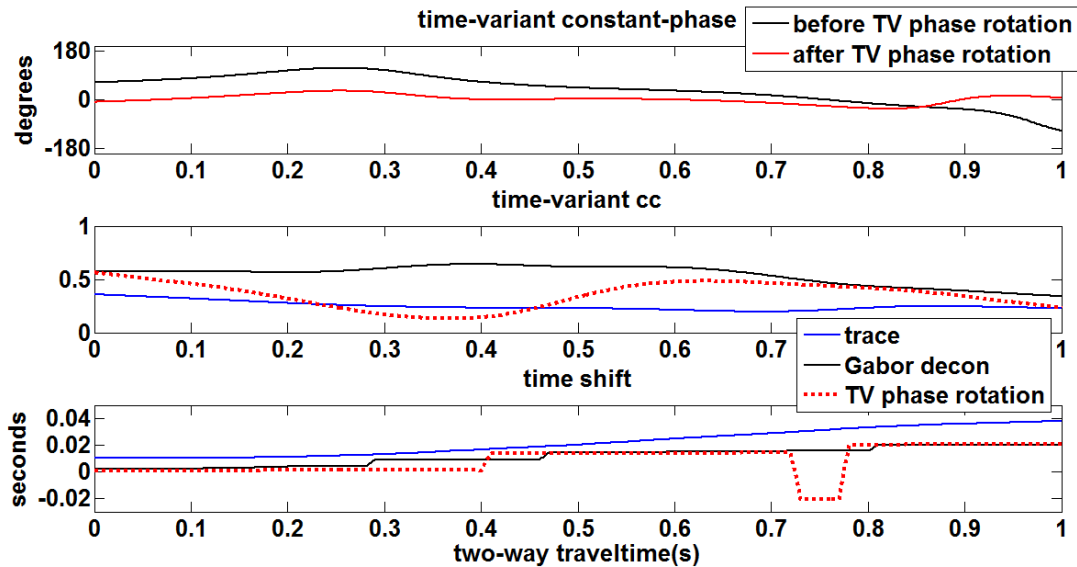


Figure 4.7: The time-variant constant-phase differences between the known reflectivity and the Gabor deconvolved trace before and after phase rotation (top). The time-variant crosscorrelation coefficient sequences between the known reflectivity and the nonstationary trace, the Gabor deconvolved trace after time-variant amplitude balancing, the Gabor deconvolved trace after time-variant amplitude balancing and time-variant constant-phase rotation (middle). The time-variant time shift sequences at which the coefficients are obtained (bottom).

4.3 Phase correction of Gabor deconvolution

To find out the reason for the residual phase after Gabor deconvolution, the propagating wavelets estimated by Gabor deconvolution are investigated. Figure 4.8 shows the estimated wavelets propagating to every 0.1 s in black, on top of which are the corresponding wavelets embedded in the nonstationary trace in red. Since the spectral separation of the propagating wavelets from the reflectivity is only determined to within a scale factor, the estimated wavelets are overall scaled so that the maximum amplitude of the estimated wavelet at time zero is equal to that of the known source wavelet for easy comparison. It can be observed that the estimated wavelets have the correct relative amplitudes and waveforms (except for those at early times

suffering from the edge effects), but they appear progressively earlier than the Q wavelets. Both the estimated and known wavelets propagating to four times: 0.3 s, 0.4 s, 0.5 s and 0.6 s are further studied in the frequency domain. Figure 4.9 compares their normalized amplitude spectra, verifying that the smoothing process in Gabor deconvolution estimates accurate amplitude spectra of the propagating wavelets. Figure 4.10 compares their unwrapped phase spectra after their propagating times at the high frequency reference velocity v_0 being removed. It can be seen that the phase estimated by Gabor deconvolution is insufficient compared to the Q wavelets.

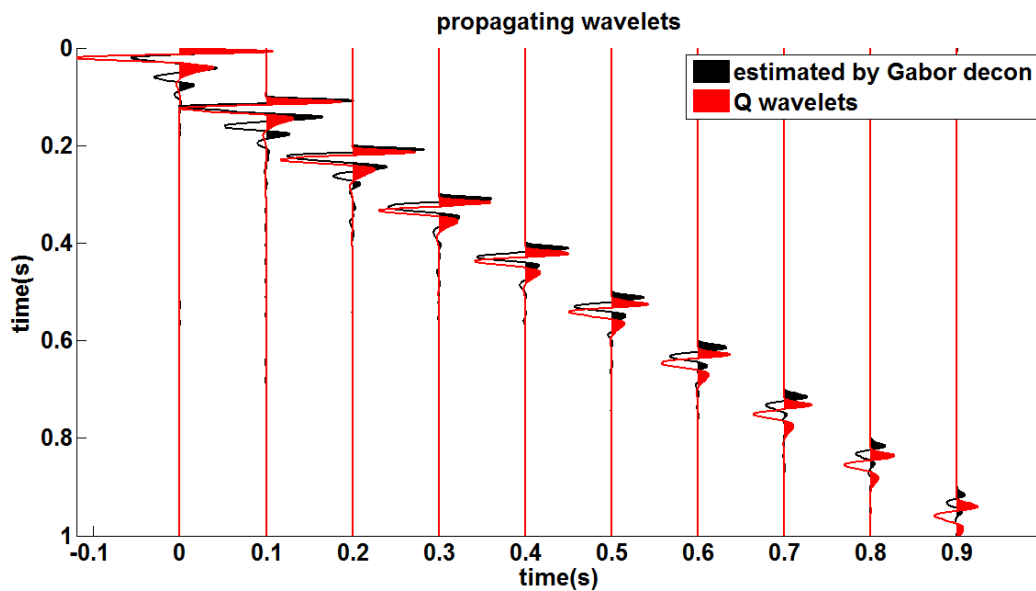


Figure 4.8: Comparison of the propagating wavelets estimated by Gabor deconvolution and those modeled by the Q matrix in Figure 3.7.

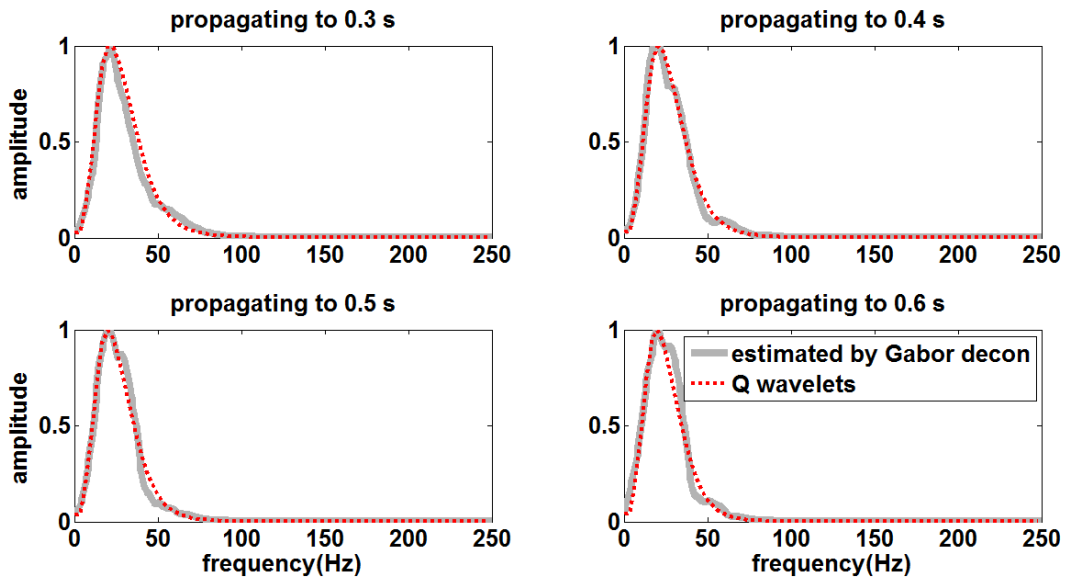


Figure 4.9: Amplitude spectra of the wavelets propagating to four different times in Figure 4.8.

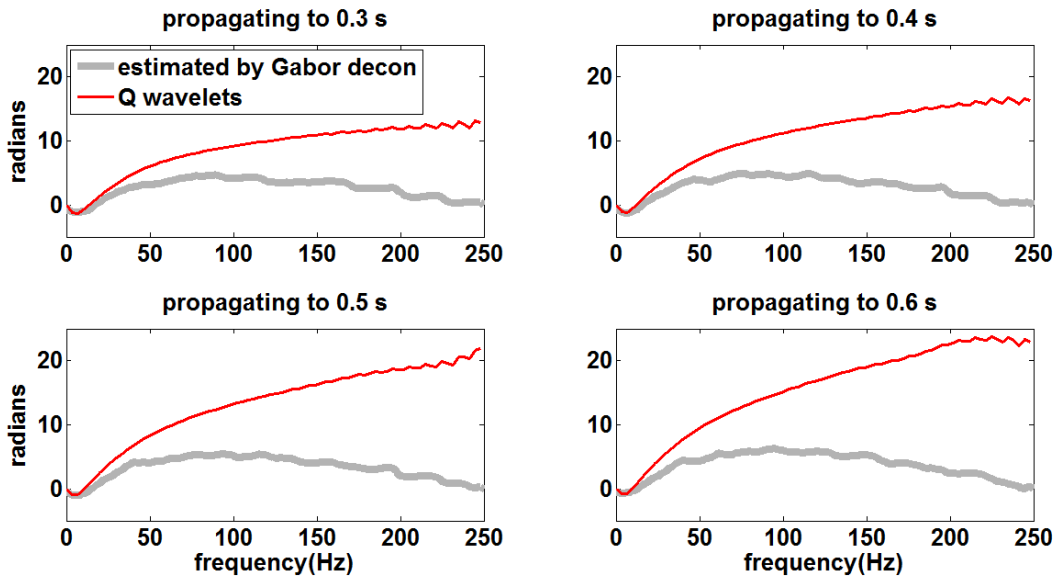


Figure 4.10: Phase spectra of the wavelets propagating to four different times in Figure 4.8.

The phase estimation errors result from the fact that the bandlimited Hilbert transform must be used (Equation 4.9) instead of the analytic one (Equation 4.8). The calculated phase is essentially with respect to the seismic Nyquist frequency f_{NYQ} (Margrave et al., 2011)

$$\varphi_{w_Q}^H(t, f) = \varphi_{w_0}(f) - 2\pi ft \left(1 - \frac{1}{\pi Q} \ln \frac{f}{f_{NYQ}}\right) \quad (4.10)$$

where $\varphi_{w_Q}^H(t, f)$ denotes the phase of the propagating wavelet at traveltime t estimated by the digital Hilbert transform. Its phase delay is less than the actual phase at traveltime t with respect to the well logging frequency f_w

$$\varphi_{w_Q}(t, f) = \varphi_{w_0}(f) - 2\pi ft \left(1 - \frac{1}{\pi Q} \ln \frac{f}{f_w}\right). \quad (4.11)$$

The difference between $\varphi_{w_Q}(t, f)$ and $\varphi_{w_Q}^H(t, f)$ is the residual phase remaining in the Gabor deconvolved trace compared to the well reflectivity

$$\Delta\varphi(t, f) = \varphi_{w_Q}(t, f) - \varphi_{w_Q}^H(t, f) = \frac{2ft}{Q} \ln \frac{f_{NYQ}}{f_w}. \quad (4.12)$$

where $\Delta\varphi(t, f)$ denotes the residual phase and it varies with traveltime t . It can be noticed from Equation 4.12 that the residual phase at a constant time t is a linear function of frequency f , implying that $\Delta\varphi(t, f)$ essentially acts as a time shift operator in the time domain, namely

$$\Delta\varphi(t, f) = -2\pi f \Delta drift(t) \quad (4.13)$$

where $\Delta drift(t)$ is a time-variant time shift function and is called the residual drift time.

According to Equations 4.12 and 4.13

$$\Delta drift(t) = \frac{t}{\pi Q} \ln \frac{f_w}{f_{NYQ}}. \quad (4.14)$$

The residual drift time is the difference between the event time at the seismic Nyquist frequency and at the sonic logging frequency after the difference between the dominant seismic frequency and the Nyquist frequency being removed by Gabor deconvolution. In the case of a time-

invariant Q value, $\Delta drift(t)$ is a linear function of t . For a layered medium where the average Q value varies with traveltime, $\Delta drift(t)$ takes on a more complex form.

Figure 4.11 compares two Q matrixes, of which the only difference is the phases of their Q wavelets. The Q wavelet phases in the left panel are constructed with respect to the well logging frequency (Equation 4.11), while those in the right panel are with respect to the seismic Nyquist frequency (Equation 4.10). Although both sets of the Q wavelets lag behind the dashed blue diagonal by a progressively increasing amount, the right-hand set appears less delayed than the left-hand set at the same traveltime. Four Q wavelets propagating to 0.3 s, 0.4 s, 0.5 s and 0.6 s are taken from the Q matrix in Figure 4.11 right panel and their phase spectra are plotted in dotted black on top of the corresponding panels in Figure 4.10 to generate Figure 4.12. The phase spectra of the propagating wavelets estimated by Gabor deconvolution match those of the Q wavelets modeled with respect to the seismic Nyquist frequency. These three sets of wavelets are plotted in the time domain in Figure 4.13, showing that the propagating wavelets estimated by Gabor deconvolution align those of the Q wavelets modeled with respect to the seismic Nyquist frequency, but are earlier than those modeled with respect to the well logging frequency. Their timing difference at an individual propagating time is a residual drift time and is denoted by a blue brace.

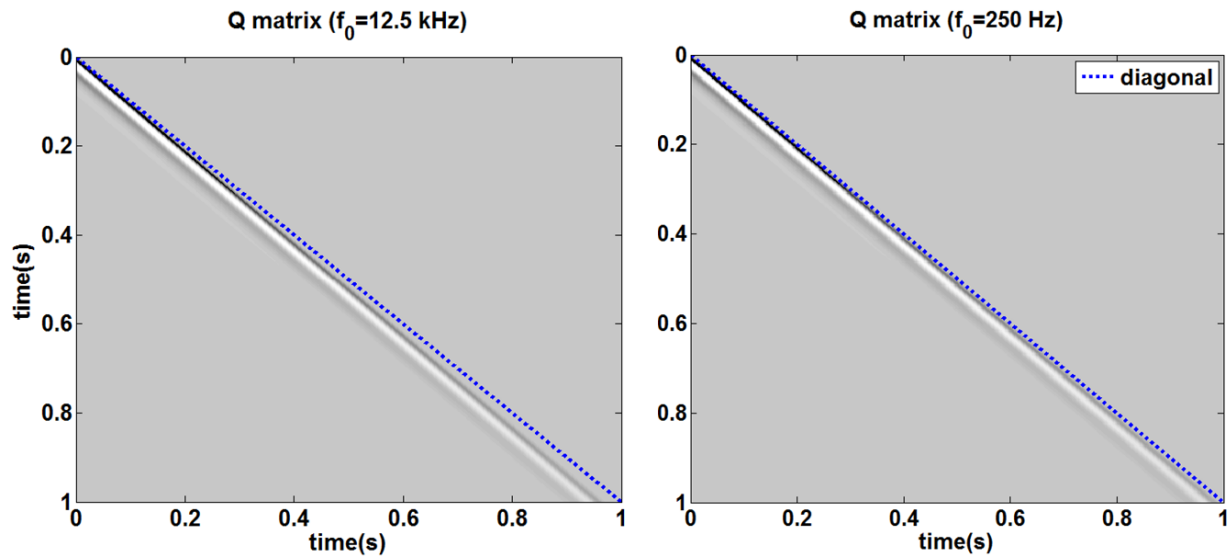


Figure 4.11: Comparison of the Q matrixes in gray built using the well logging frequency (left, the same as Figure 3.7 left panel) and the seismic Nyquist frequency (right) as the reference frequency respectively.

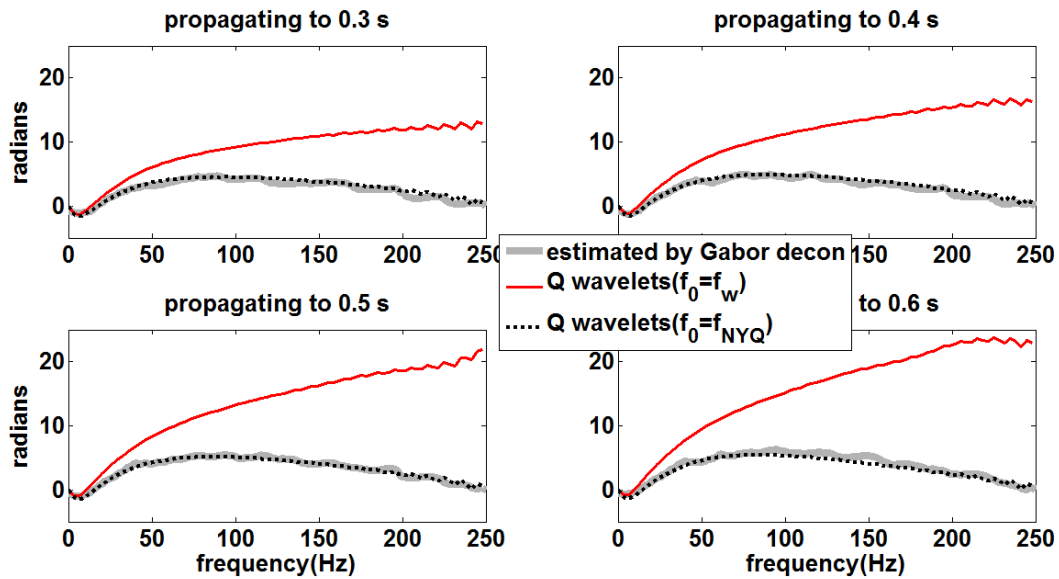


Figure 4.12: Same as Figure 4.10 except that the phase spectra of the propagating wavelets modeled by the Q matrix with respect to the seismic Nyquist frequency are plotted as well.

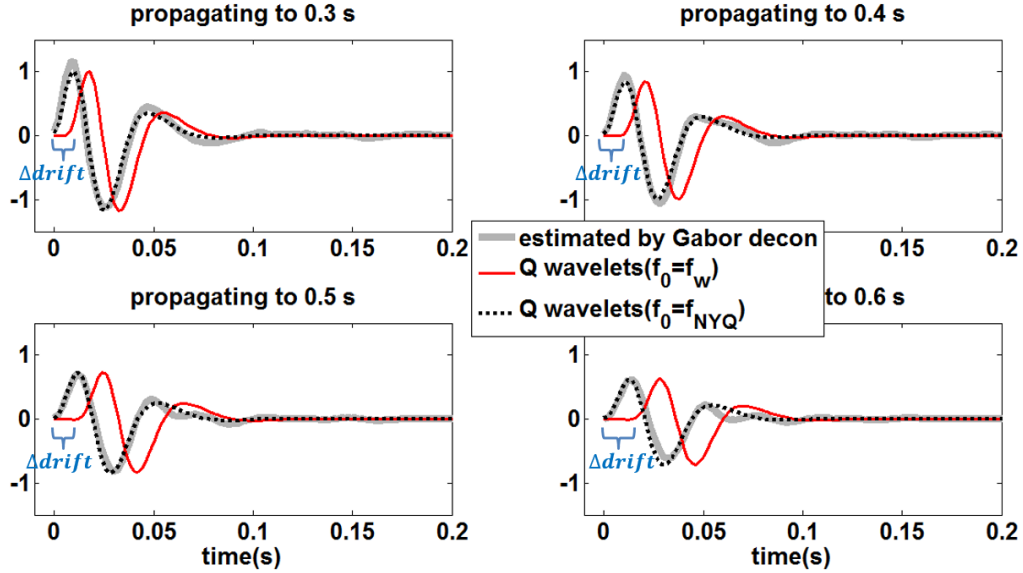


Figure 4.13: The time-domain propagating wavelets at four different times estimated by Gabor deconvolution, modeled by the Q matrixes with respect to the well logging frequency and the seismic Nyquist frequency.

The residual phase can be calculated by Equation 4.12 as long as the values of Q and f_w are known. Then the phase of the propagating wavelets estimated by Gabor deconvolution can be corrected by

$$\varphi_{w_Q}^{H,c}(t, f) = \varphi_{w_Q}^H(t, f) + \Delta\varphi(t, f) \quad (4.15)$$

where $\varphi_{w_Q}^{H,c}(t, f)$ is the corrected phase of the propagating wavelet at travelttime t . With the known values of $Q = 50$ and $f_w = 12.5 \text{ kHz}$, the phase spectra after correction are calculated and are plotted in bold gray in Figure 4.14. They are seen to match those of the Q wavelets with respect to the well logging frequency. These three sets of wavelets in Figure 4.14 are plotted in the time domain in Figure 4.15, showing that phase correction delays the estimated wavelets by the amount of the corresponding residual drift time to align them with the Q wavelets with respect to the well logging frequency. Similarly, Figure 4.16 shows the estimated wavelets after

phase correction propagating to every 0.1 s in black, the timing of which is consistent with that of the corresponding wavelets embedded in the nonstationary trace in red.

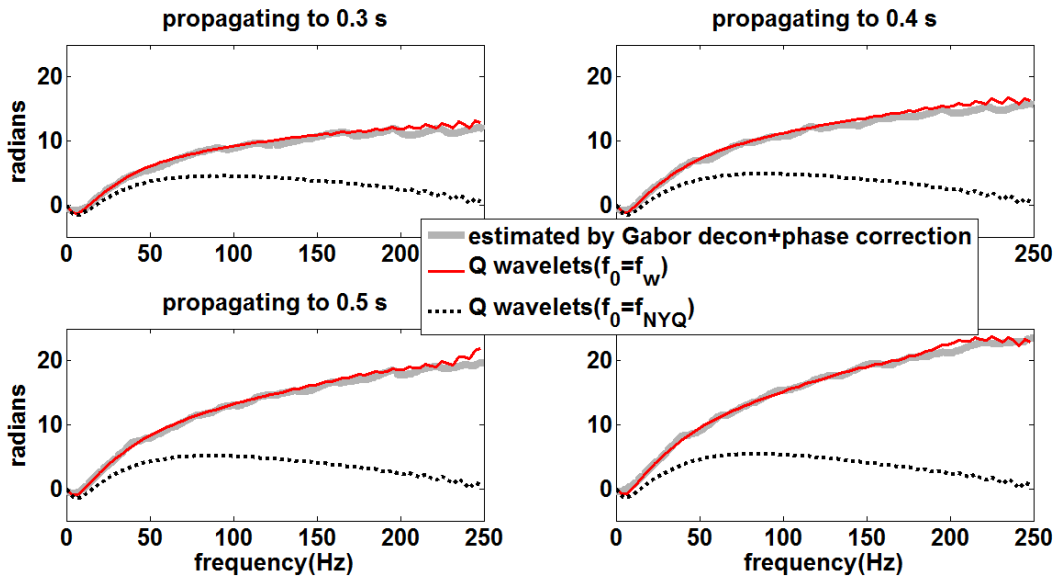


Figure 4.14: Same as Figure 4.12 except that the wavelets estimated by Gabor deconvolution are phase corrected.

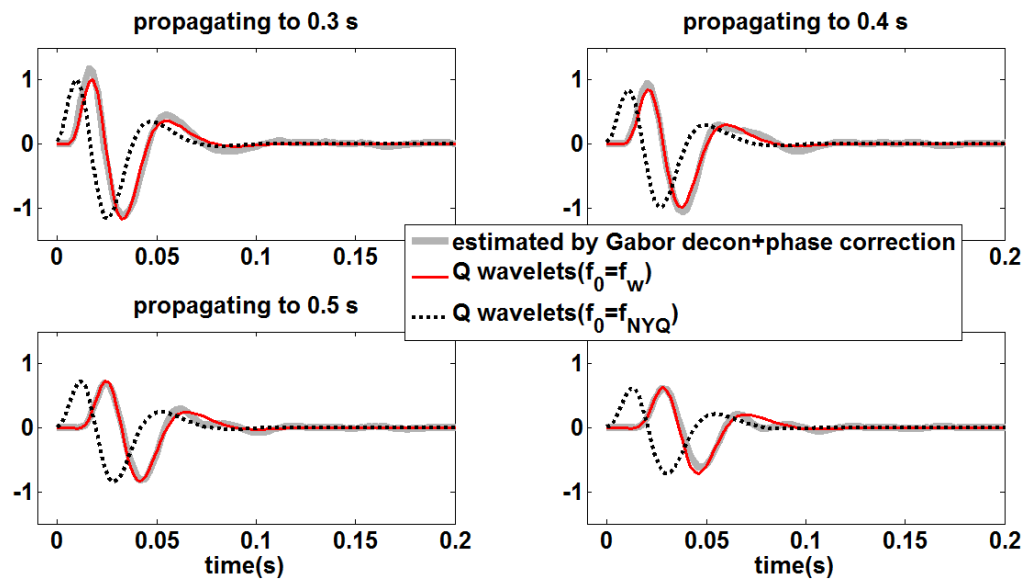


Figure 4.15: Same as Figure 4.13 except that the wavelets estimated by Gabor deconvolution are phase corrected.

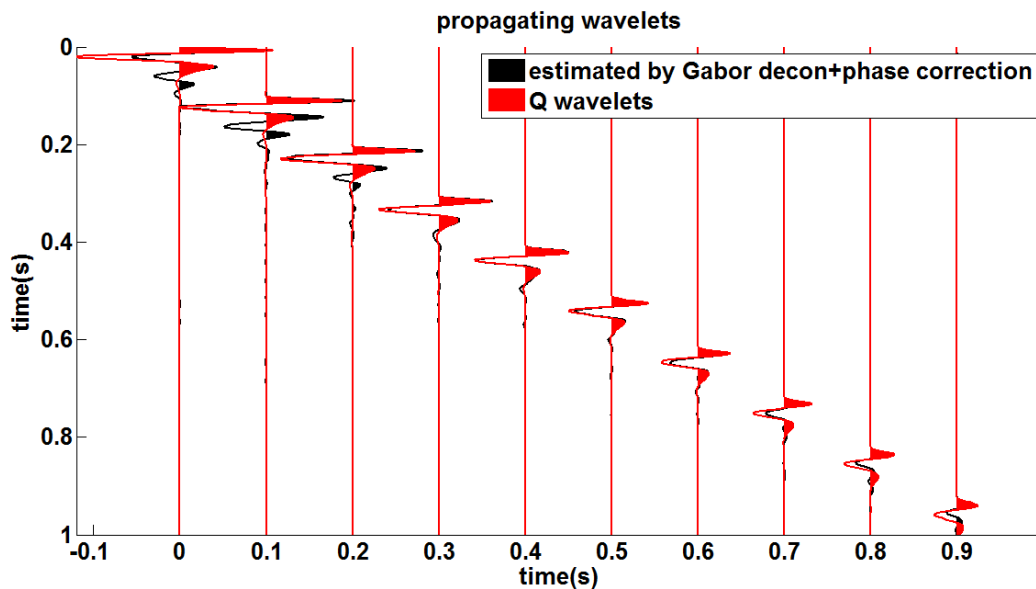


Figure 4.16: Comparison of the propagating wavelets estimated by Gabor deconvolution with phase correction and those modeled by the Q matrix with respect to the well logging frequency in Figure 3.7.

Deconvolving the estimated wavelets with the corrected phases from the nonstationary seismic trace, the estimated reflectivity is shown to be much better tied to the well reflectivity than that without phase correction in Figure 4.17. Next, the amplitude of the phase corrected reflectivity estimate is balanced and its phase is rotated with respect to the known reflectivity in the same time-variant way as before. It can be observed from Figure 4.17 that time-variant amplitude balancing and time-variant constant-phase rotation do little change to the phase corrected reflectivity estimate. As a quality control, Figure 4.18 shows that phase correction reduces both the time-variant constant-phase difference and the time-variant time shift to zero, and enhances the time-variant crosscorrelation coefficient between the estimated and known reflectivities. It can be concluded that running Gabor deconvolution on the nonstationary trace removes the propagating wavelet phase delay to the seismic Nyquist frequency only. By correcting the estimated wavelet phase to the well logging frequency, the Gabor deconvolved trace can be well tied to the known reflectivity with very little amplitude and phase errors.

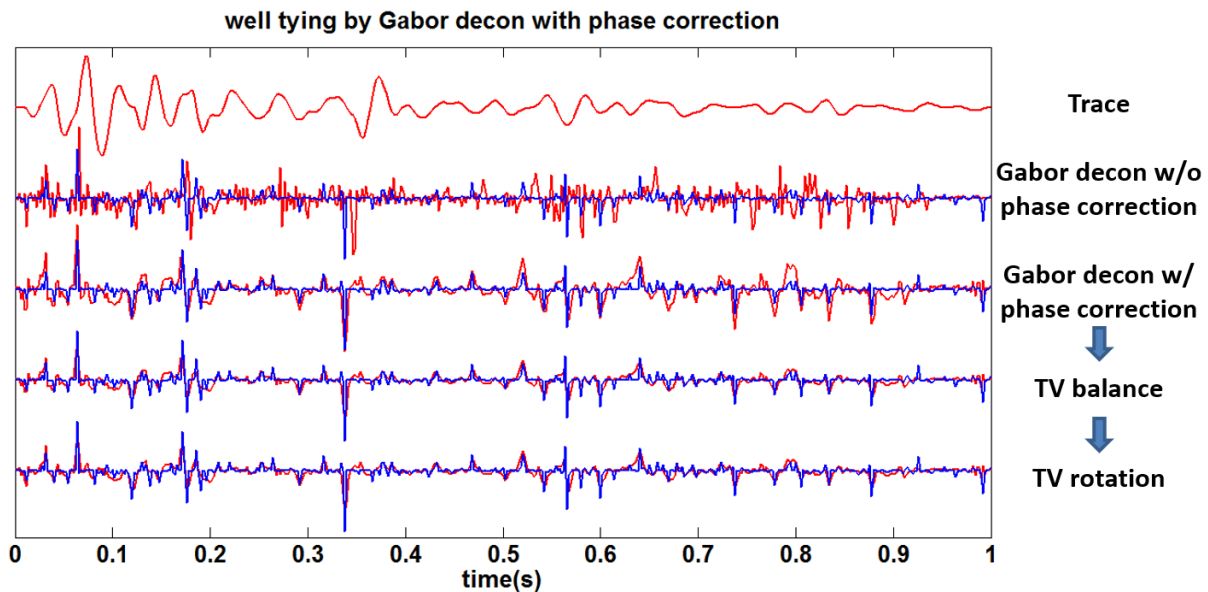


Figure 4.17: A procedure of tying the nonstationary trace to the known reflectivity (blue) by Gabor deconvolution, phase correction, time-variant amplitude balancing and time-variant constant-phase rotation.

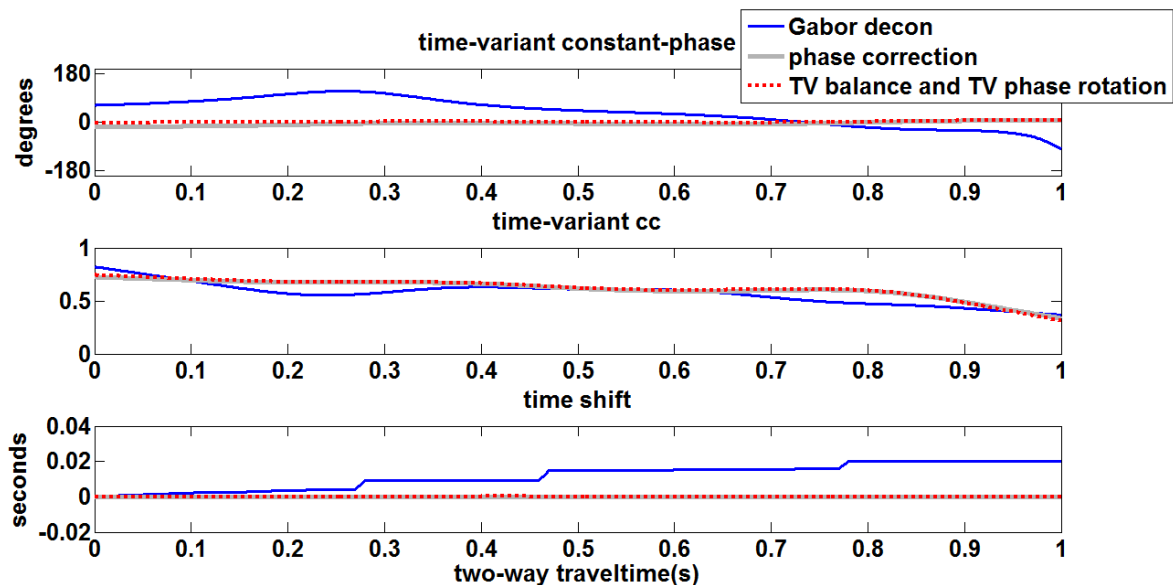


Figure 4.18: The time-variant constant-phase differences (top), the time-variant crosscorrelation coefficient sequences (middle) and the time-variant time shift sequences at which the coefficients are obtained (bottom) between the known reflectivity and the Gabor deconvolved trace, the Gabor deconvolved trace after phase correction, the Gabor

deconvolved trace after phase correction, time-variant amplitude balancing and time-variant constant-phase rotation.

4.4 Residual drift time estimation after Gabor deconvolution

As can be seen from Equation 4.13 that applying phase correction in the Gabor domain is equivalent to applying a time-variant residual drift time correction by Equation 2.2 in the time domain. Figure 4.19 displays that the Gabor deconvolved trace is precisely tied to the well reflectivity after its timing is corrected by the residual drift time, which is calculated using the known values of Q as well as the well logging frequency via Equation 4.14 and is plotted in solid gray in Figure 4.20 top panel. With a time-invariant Q value, the theoretical residual drift time in this case is a linear function of traveltime t .

Although Gabor deconvolution with either phase correction or residual drift time correction can tie the nonstationary seismic trace to the well reflectivity accurately, neither of them works without knowledge of Q or the well logging frequency. Without this information, time-variant crosscorrelation and smooth dynamic time warping are tested to estimate the residual time-variant drift time by matching the Gabor deconvolved seismic trace to the well reflectivity statistically. Figure 4.20 top panel shows the residual drift time estimated by TVCC in solid blue using a sliding Gaussian window with 200 ms half-width and 10 ms increment, which approximates the known trend but with major discontinuities. The residual drift time estimated by SDTW is plotted in dotted red using a coarse sampling interval h equals 200 samples (namely 0.4 s) and it estimates the known residual drift time perfectly. The timing of the Gabor deconvolved seismic trace is corrected by the estimated residual drift time with each method and is compared to the well reflectivity respectively in Figure 4.19. It can be observed

that the Gabor deconvolved trace corrected by TVCC has obvious misties (indicated by yellow boxes), where the estimated residual drift time has discontinuities. In contrast, the Gabor deconvolved trace corrected by SDTW is well tied to the known reflectivity. As a quality control, the time-variant crosscorrelation coefficient sequences between the well reflectivity and the Gabor deconvolved traces with different residual drift time corrections in Figure 4.19 are calculated by Equation 3.26 and are plotted in Figure 4.20 bottom panel, from which we see that the Gabor deconvolved trace corrected by the SDTW estimated residual drift time ties to the well reflectivity as well as that corrected by the known residual drift time and is better than that corrected by the TVCC estimated residual drift time.

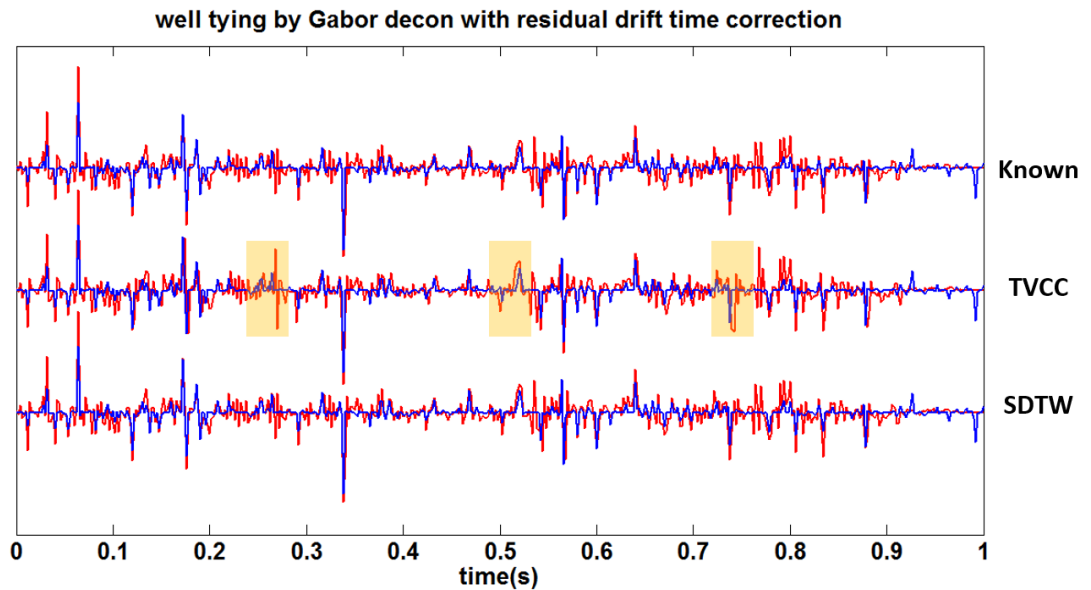


Figure 4.19: The Gabor deconvolved trace corrected by the known residual drift time, the residual drift time estimated by time-variant crosscorrelation and the residual drift time estimated by smooth dynamic time warping compared to the well reflectivity (blue) separately.

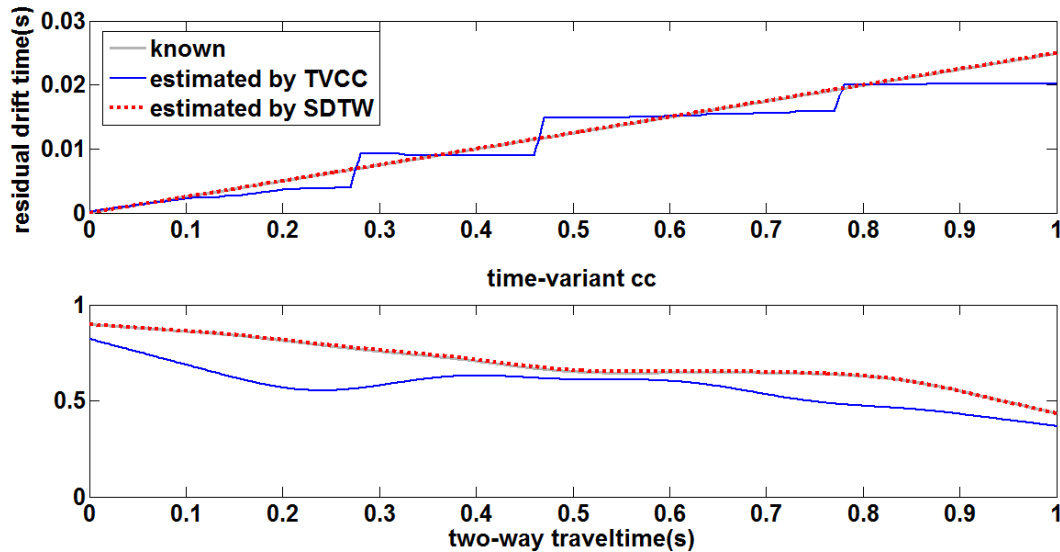


Figure 4.20: Residual drift time after Gabor deconvolution: the known function, time-variant crosscorrelation estimate and smooth dynamic time warping estimate (top). Time-variant time shift sequences between the known reflectivity and the Gabor deconvolved trace corrected by the known residual drift time, corrected by the residual drift time estimated by time-variant crosscorrelation and corrected by the residual drift time estimated by smooth dynamic time warping (bottom).

4.5 Summary

- Running Gabor deconvolution on the nonstationary trace can get the reflectivity estimate tying the well reflectivity in amplitude and spectral content, but has phase errors which are more complex than those that can be solved by time-variant constant-phase rotation.
- Gabor deconvolution accurately estimates the amplitude spectra of the propagating wavelets.
- Gabor deconvolution calculates the phase spectra of the propagating wavelets by the digital Hilbert transform, which integrates within the seismic frequency band and corrects the drift time to the Nyquist frequency only.

- By correcting the estimated wavelet phase to the well logging frequency, the Gabor deconvolved trace can be well tied to the known reflectivity with very little amplitude and phase errors.
- Gabor deconvolution with either phase correction or residual drift time correction can tie the nonstationary seismic trace to well reflectivity accurately knowing the Q values and the well logging frequency. Smooth dynamic time warping can estimate the residual drift time without knowledge of Q or the well logging frequency, and the estimation is more accurate than time-variant crosscorrelation.

Chapter Five: Seismic-to-well ties on Hussar synthetics and field data

5.1 Chapter overview

In September 2011, CREWES initiated a seismic experiment near Hussar, Alberta, with the goal to study the low frequency content of the seismic data (Margrave et al., 2012). Figure 5.1 shows the location of the 4.5 km long seismic line and the three intersected wells 12-27, 14-27 and 14-35. While seismic datasets with different source and receiver types are available, this thesis uses the dataset with dynamite source recorded by 10 Hz geophones. P-wave sonic, density, and gamma ray logs are available in all the three wells.

In this chapter, nonstationary synthetic seismogram is first constructed based on Hussar well 12-27 by creating a plausible Q structure. Internal multiples are also included in the nonstationary synthetic seismogram. The nonstationary seismograms are then tied to the well reflectivity by Gabor deconvolution with phase correction, during which the Q values are estimated. All the three wells are also tied to the real seismic data, followed by bandlimited impedance inversion to examine the quality of seismic-to-well ties.

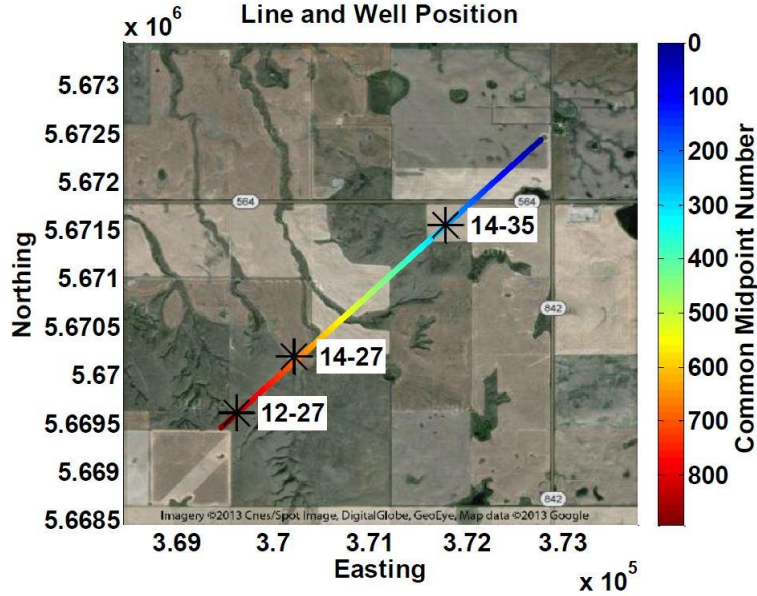


Figure 5.1: The location of the seismic line and wells in Hussar experiment (Lloyd, 2013).

5.2 Seismic-to-well ties on well-based 1-D seismogram models

5.2.1 Hypothetical Q log

Figure 5.2 shows a density log and a P-wave velocity log acquired from Hussar well 12-27. The logs are edited and the overburdens are neglected so that depth zero corresponds to the top of the logs. A plausible Q structure is generated by assuming that there is a linear relationship between the Q value and the values of P-wave velocity v_p and density ρ (Margrave, 2013b)

$$Q_v(z) = Q_{min} \frac{v_p(z) - v_{max}}{v_{min} - v_{max}} + Q_{max} \frac{v_p(z) - v_{min}}{v_{max} - v_{min}} \quad (5.1)$$

and

$$Q_\rho(z) = Q_{min} \frac{\rho(z) - \rho_{max}}{\rho_{min} - \rho_{max}} + Q_{max} \frac{\rho(z) - \rho_{min}}{\rho_{max} - \rho_{min}} \quad (5.2)$$

where Q_{min} , Q_{max} , v_{min} , v_{max} , ρ_{min} , ρ_{max} are all specified constants that determine the linear relationships by mapping Q_{min} to v_{min} and ρ_{min} , as well as mapping Q_{max} to v_{max} and ρ_{max} .

Then the velocity Q and density Q are combined into a final Q

$$\frac{1}{Q} = \frac{1}{Q_v} + \frac{1}{Q_\rho}. \quad (5.3)$$

Figure 5.2 plots the hypothetical Q log in green, which is created from the density and P-wave velocity logs given the values $Q_{min} = 20$, $Q_{max} = 100$, $v_{min} = 1500$ m/s, $v_{max} = 4500$ m/s, $\rho_{min} = 1800$ kg/m³ and $\rho_{max} = 3000$ kg/m³. Note that at a depth where the values of density and P-wave velocity are low, the Q value is also small, indicating strong attenuation effects.

With knowledge of the Q structure and the P-wave velocity at the logging frequency of 12.5 kHz as well as assuming that the dominant seismic frequency is about 30 Hz, the P-wave velocity propagating at the seismic frequency can be calculated by Equation 3.11 and is plotted in red in Figure 5.2, whose value is systematically lower than that measured by the sonic tool.

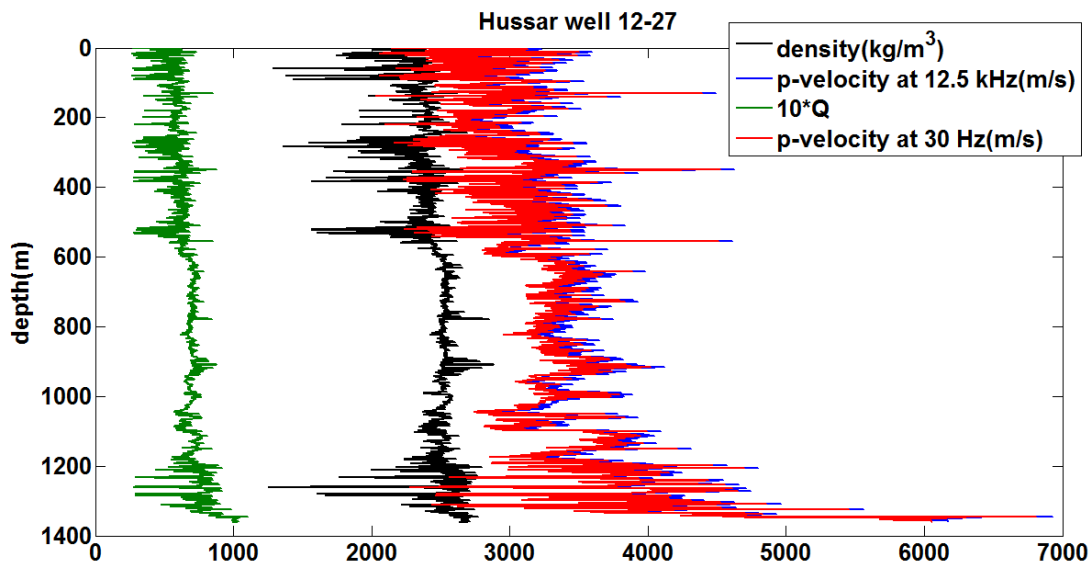


Figure 5.2: Logs from Hussar well 12-27.

5.2.2 Drift time

The constant-Q theory predicts that velocity must be frequency dependent. It follows that a synthetic seismogram computed from well logs will predict reflection event times systematically earlier than those in the seismic data. The difference between the event time at the dominant seismic frequency and at the sonic logging frequency is called the drift time (Margrave, 2013b). Given a layered medium, the two-way vertical traveltime to depth z_n is calculated by

$$t(z_n, f) = 2 \sum_{k=1}^n \frac{dz_k}{v_k(f)} \quad (5.4)$$

where $dz_k = z_{k+1} - z_k$ is the layer thickness, and $v_k(f)$ is the frequency-dependent velocity of the k^{th} layer. The drift time is calculated as

$$drift(z_n) = t(z_n, f_s) - t(z_n, f_w) \quad (5.5)$$

where f_s and f_w are the dominant frequencies of the seismic and the well logging respectively.

Plug Equation 5.4 into 5.5

$$drift(z_n) = 2 \sum_{k=1}^n \left[\frac{dz_k}{v_k(f_s)} - \frac{dz_k}{v_k(f_w)} \right]. \quad (5.6)$$

Substitute $v_k(f_s)$ for $v_k(f_w)$ by Equation 3.11

$$drift(z_n) = \frac{1}{\pi} \ln \frac{f_w}{f_s} \sum_{k=1}^n \frac{1}{Q_k} \frac{2dz_k}{v_k(f_w)} \quad (5.7)$$

where Q_k is the interval Q of the k^{th} layer. Since the two-way time thickness of the k^{th} layer

$dt_k = \frac{2dz_k}{v_k(f_w)}$, Equation 5.7 becomes

$$drift(z_n) = \frac{1}{\pi} \ln \frac{f_w}{f_s} \sum_{k=1}^n \frac{dt_k}{Q_k}. \quad (5.8)$$

The average Q and interval Q are related by

$$Q_{ave}(z_n) = \left[\frac{1}{t_n} \sum_{k=1}^n \frac{dt_k}{Q_k} \right]^{-1} \quad (5.9)$$

where $Q_{ave}(z_n)$ is the Q value averaged from the surface to the n^{th} layer and t_n is the two-way traveltime to the n^{th} layer. Substitute Equation 5.9 into 5.8

$$drift(z_n) = \frac{t_n}{\pi Q_{ave}(z_n)} \ln \frac{f_w}{f_s}. \quad (5.10)$$

As is introduced by Chapter 4, the residual drift time is the difference between the event time at the seismic Nyquist frequency and at the sonic logging frequency after the difference between the dominant seismic frequency and the Nyquist frequency being removed by Gabor deconvolution. Analogous to Equation 5.10, the residual drift time expressed by Equation 4.14 can also be written as

$$\Delta drift(z_n) = \frac{t_n}{\pi Q_{ave}(z_n)} \ln \frac{f_w}{f_{NYQ}}. \quad (5.11)$$

The two P-wave velocity logs in Figure 5.2 are converted into time-depth curves and are shown in Figure 5.3 left panel, from which the two-way traveltime at the seismic frequency is seen to be greater than that at the well logging frequency to the same depth. Their difference is the drift time shown in Figure 5.3 right panel.

In seismic-to-well ties, drift time correction is a necessary step to tie the synthetic seismogram to the seismic trace. Calculation of drift time in industrial practice needs one of the following: (1) estimating Q values and calculating the expected sonic velocities at the seismic frequency predicted by the constant-Q theory, (2) acquiring a VSP (vertical seismic profile) or a check-shot survey to get traveltime at the seismic frequency corresponding to each depth, (3) manually stretching and squeezing the synthetic seismograms until their key events interpretatively match those in the seismic traces. Measurement of Q is a difficult process and the

actual Q values can only be crudely estimated at present (Margrave, 2013c). A VSP or a check-shot survey is not always available. Manually stretching and squeezing the synthetic seismogram is a tedious process and is usually regarded as cosmetic (White et al., 1998). Without this information, smooth dynamic time warping (SDTW) is used to estimate the drift time and the residual drift time in the following examples.

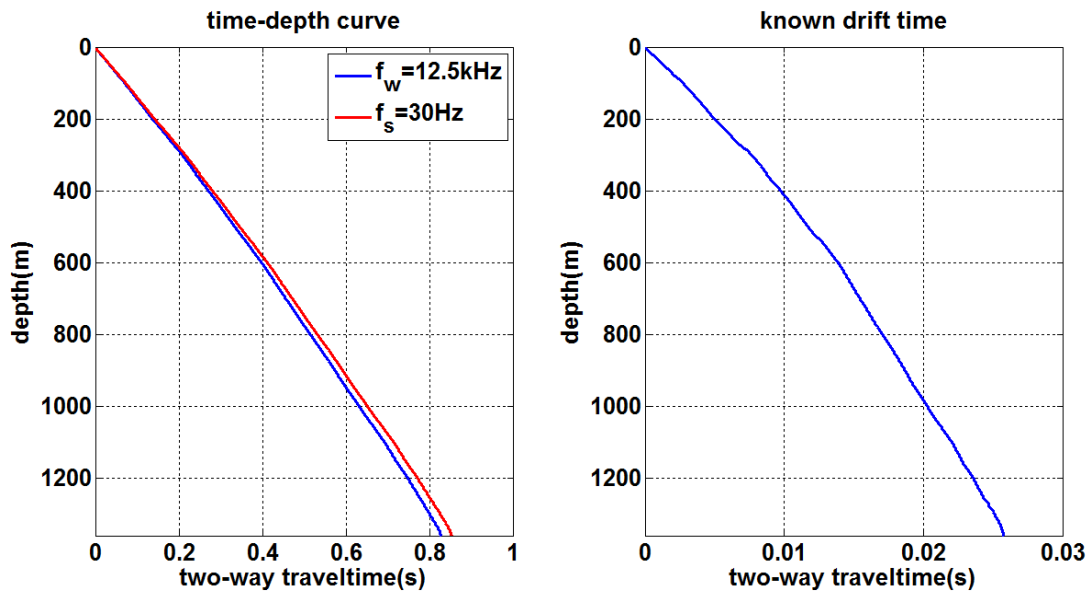


Figure 5.3: Time-depth relations at different frequencies (left) and the drift time with respect to depth (right).

5.2.3 Well-based 1-D seismogram models

A stationary seismogram is created to simulate the synthetic seismogram to tie well logs to seismic traces. Figure 5.4 left panel shows the reflectivity series, which is calculated from the density and P-wave velocity logs in Figure 5.2. It is a time series of normal incident P-wave reflection coefficients positioned at the two-way traveltme to each subsurface reflector. Stationary convolution of the reflectivity with a minimum-phase source wavelet whose dominant

frequency is 30 Hz (Figure 5.4 middle panel) is the stationary seismogram $s(t)$ in Figure 5.4 right panel.

To simulate the real seismic trace including Q effects, a synthetic zero-offset VSP model is generated using the hypothetical Q log, as well as the same density log, P-wave velocity log and source wavelet as those used to construct the stationary seismogram. The algorithm is based on propagator matrices proposed by Ganley (1981) and the program is developed by Margrave and Daley (2014). Figure 5.5 shows the primaries-only upgoing wavefield with Q effects. The trace recorded by the surface receiver is the nonstationary trace with Q effects $s_q(t)$, and is plotted on top of the stationary seismogram $s(t)$ in Figure 5.6. Although not shown here, $s_q(t)$ constructed by this algorithm is identical to that created by the nonstationary convolutional model described in Chapter 3 using the same input Q values, well logs and source wavelet.

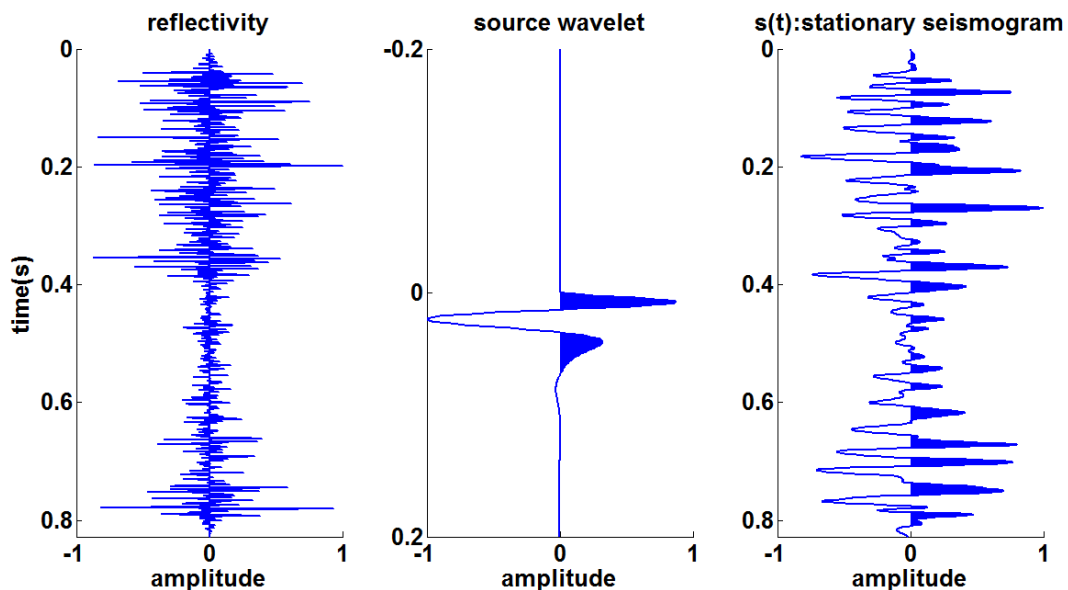


Figure 5.4: Construction of a stationary seismogram $s(t)$.

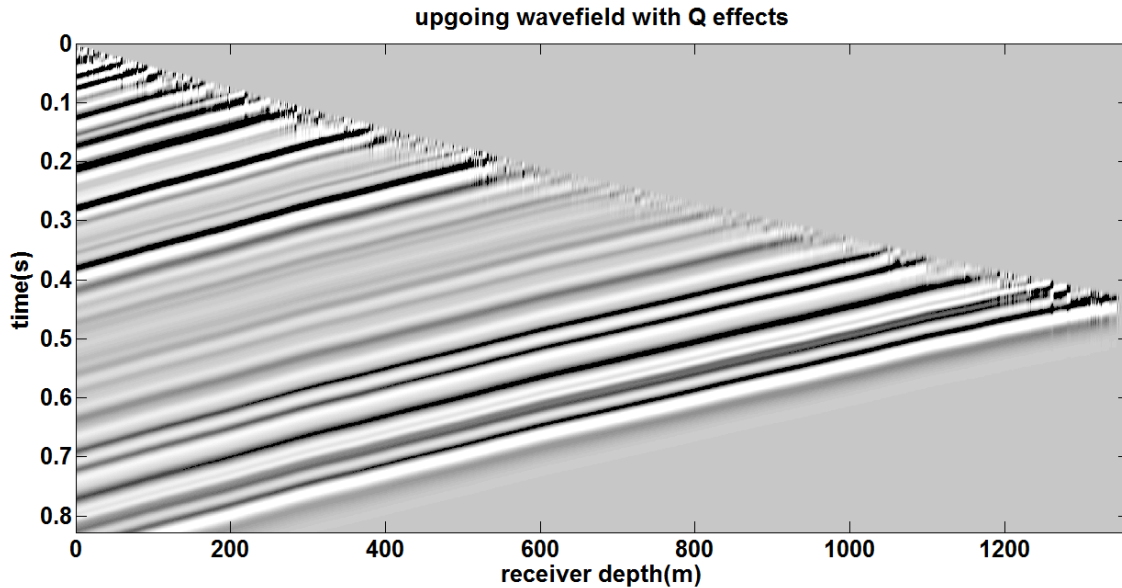


Figure 5.5: The primaries-only upgoing wavefield of the synthetic zero-offset VSP model with Q effects.

5.2.4 Tying the nonstationary trace with Q effects to the well reflectivity

As is shown in Figure 5.6, compared to the stationary seismogram s in blue, the nonstationary seismic trace s_q in red is delayed by the amount of drift time, which can be calculated via Equation 5.10 knowing Q values, and is plotted with respect to two-way traveltime in solid grey in Figure 5.7 top panel. Without knowledge of Q, SDTW can estimate the drift time by warping s_q to tie s . The estimated drift time is plotted in dotted black in Figure 5.7 top panel and is shown to well approximate the known drift time.

The nonstationary trace is tied to the well reflectivity by Gabor deconvolution with or without phase correction, time-variant amplitude balancing and time-variant constant-phase rotation. The final tying results are shown in Figure 5.6 in which the well reflectivities are plotted twice in blue while its estimates are in red. We can see that the nonstationary trace is

better tied to the well reflectivity with phase correction, during which SDTW estimates the residual drift time by warping Gabor deconvolved s_q to tie the well reflectivity. Figure 5.7 top panel shows the estimated residual drift time in dotted red. It is consistent with the known residual drift time in solid blue, which is calculated by Equation 5.11 using Q values. As is shown in Figure 5.7 middle panel, the time-variant constant-phase difference between Gabor deconvolved s_q and the well reflectivity becomes almost zero along the traveltime after phase correction. The time-variant crosscorrelation coefficients between the well reflectivity and its estimates are calculated at lag zero and are plotted in Figure 5.7 bottom panel, indicating an increased correlation after phase correction.

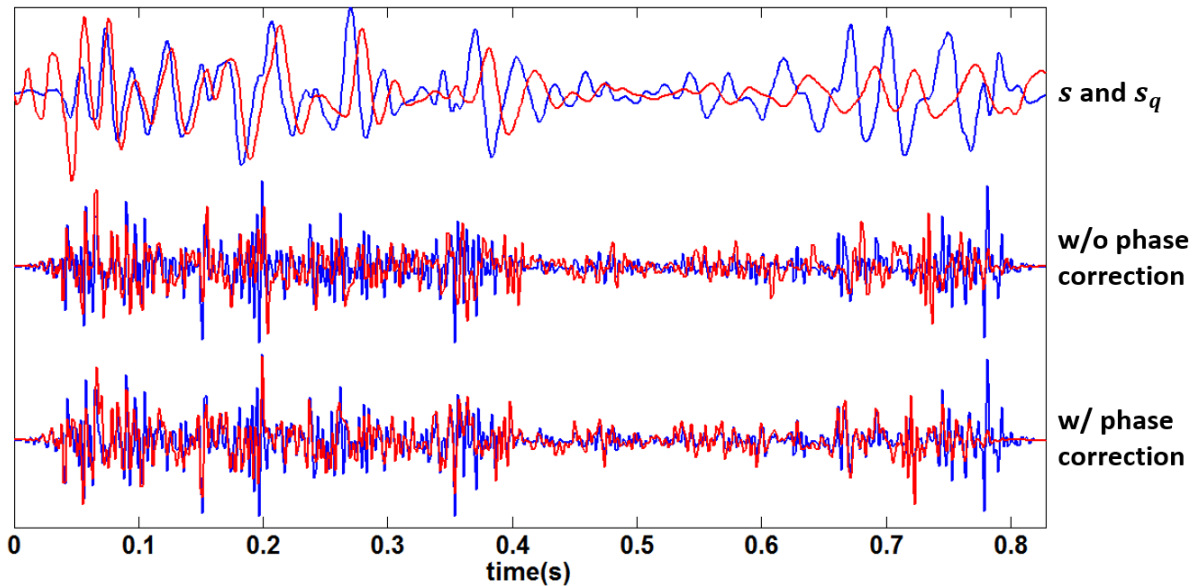


Figure 5.6: The stationary seismogram $s(t)$ and the nonstationary trace with Q effects $s_q(t)$ (top), the reflectivity estimate without phase correction compared to the well reflectivity (middle), the reflectivity estimate with phase correction compared to the well reflectivity (bottom).

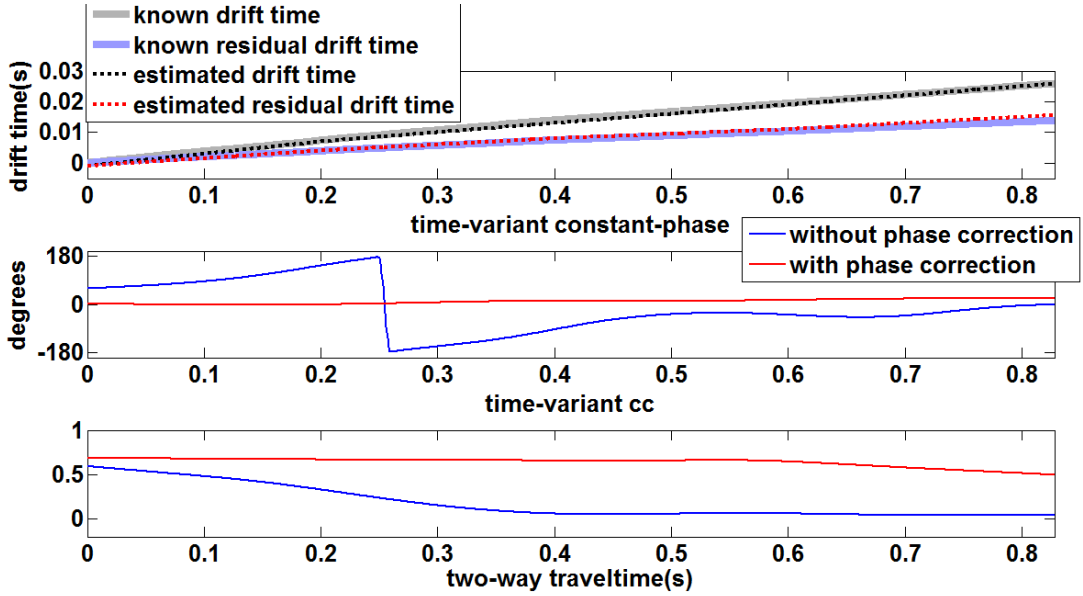


Figure 5.7: The estimated drift time and residual drift time sequences compared to the known ones (top). The time-variant constant-phase differences between the well reflectivity and Gabor deconvolved $s_q(t)$ with and without phase correction (middle). The time-variant crosscorrelation coefficients at lag zero between the well reflectivity and its estimates with and without phase correction (bottom).

5.2.5 Q estimation

As Figure 5.7 top panel shows, SDTW accurately estimates the drift time and the residual drift time without knowledge of Q . Since the Q values are related to the drift time and the residual drift time by Equation 5.10 and Equation 5.11 respectively, the average Q can be calculated from the estimated drift time via

$$Q_{ave}(z_n) = \frac{t_n}{\pi \text{drift}(z_n)} \ln \frac{f_w}{f_s} \quad (5.12)$$

or from the estimated residual drift time via

$$Q_{ave}(z_n) = \frac{t_n}{\pi \Delta \text{drift}(z_n)} \ln \frac{f_w}{f_{NYQ}}. \quad (5.13)$$

In Figure 5.8, the hypothetical Q log is mapped from depth to two-way traveltime and is plotted in solid blue, from which the known average Q is calculated by Equation 5.9 and is plotted in solid black. We can observe that the average Q is much smoother than the interval Q. The estimated average Q from drift time estimation is plotted in dotted red and that from the residual drift time estimation is plotted in dotted green. Although the estimated Q values have large errors at very early times, they are roughly precise after 0.2 s.

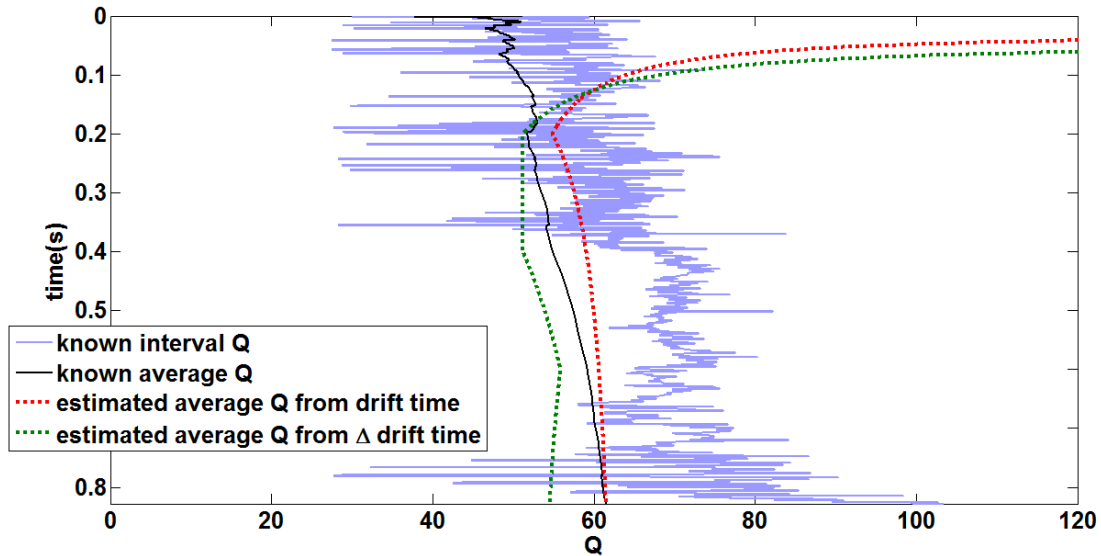


Figure 5.8: The known interval Q, known average Q, estimated average Q from drift time and residual drift time estimation.

Assuming that there is no knowledge or estimation of detailed Q structure, the accuracy of phase correction using a time-invariant Q is tested. A series of time-invariant Q values ranging from 20 to 100 in an increment of 10 are used individually for calculating the residual drift time by Equation 5.11 to correct the phase of Gabor deconvolved s_q , followed by time-variant amplitude balancing and time-variant constant-phase rotation. Figure 5.9 shows some final reflectivity estimates (red) after phase correction with corresponding Q values compared to the well

reflectivity (blue). The overall crosscorrelation coefficients between the well reflectivity and its estimates are calculated at lag zero and are plotted in blue Figure 5.10 with respect to the corresponding time-invariant Q values used for phase correction. The red star indicates the case that the known time-variant Q values are used for phase correction. Its vertical coordinate is the crosscorrelation coefficient and its horizontal coordinate is the overall average Q value from surface to the log bottom. The black star indicates the case that there is no phase correction. Its vertical coordinate is the crosscorrelation coefficient and its horizontal coordinate is the maximum Q value being tested. It can be seen that in this example, a time-invariant Q roughly ranging from 50 to 70 can plausibly correct the phase errors of Gabor deconvolved nonstationary seismic trace to tie the well reflectivity.

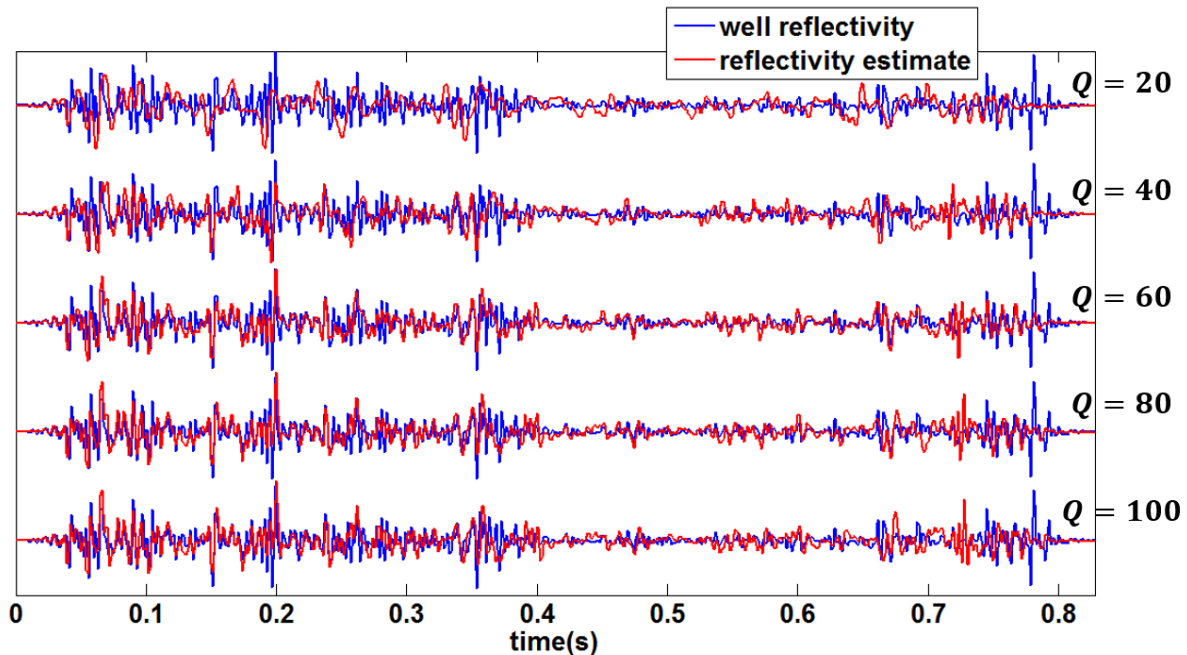


Figure 5.9: The reflectivity estimates (red) with phase correction using a series of time-invariant Q values compared to the well reflectivity (blue).

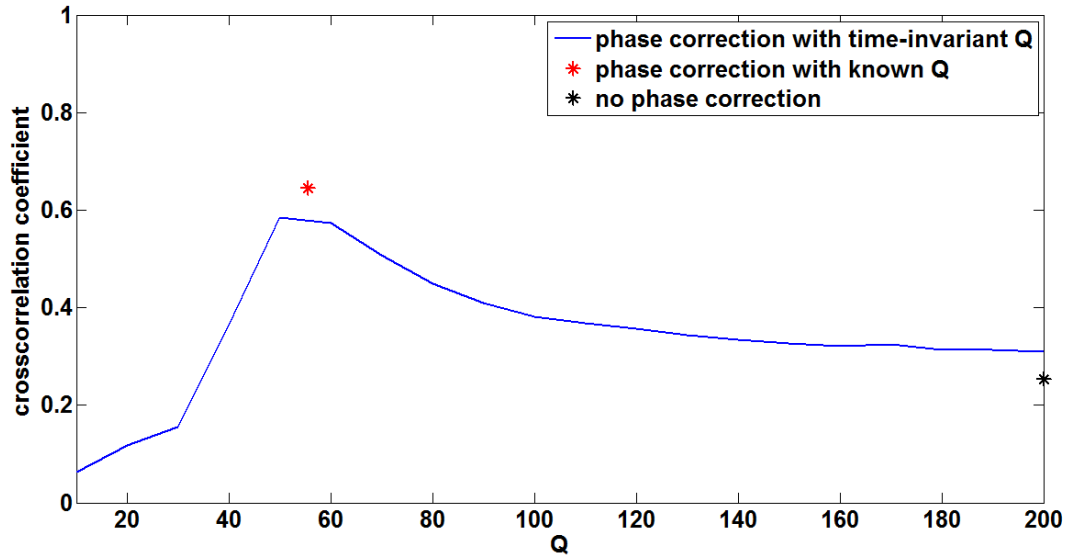


Figure 5.10: The overall crosscorrelation coefficients between the reflectivity estimates and the well reflectivity at lag zero with respect to the corresponding time-invariant Q values used for phase correction. The cases that the known time-variant Q values are used for phase correction and there is no phase correction are plotted as stars for reference.

5.2.6 Inclusion of internal multiples

A more realistic 1-D nonstationary seismogram containing internal multiples is constructed by the synthetic zero-offset VSP model using the same Q values, well logs and source wavelet. Figure 5.11 shows its upgoing wavefield including both primaries and internal multiples with Q effects. The trace recorded at depth zero is the nonstationary trace with both Q and internal multiple effects $s_{qi}(t)$ and is plotted in Figure 5.12 top panel on top of $s(t)$ and $s_q(t)$. The events in $s_{qi}(t)$ are observed to be more decayed in amplitude and more delayed in timing than $s_q(t)$. Figure 5.12 bottom panel plots the same known drift time in solid grey and the known residual time in solid blue as Figure 5.7 top panel. The SDTW estimated drift time between $s(t)$ and $s_{qi}(t)$ is plotted in dotted black, which appears greater than the known drift

time. The SDTW estimated residual drift time between the well reflectivity and Gabor deconvolved $s_{qi}(t)$ is plotted in dotted red, which is higher than the known residual drift time as well. The SDTW estimated time shift between the well reflectivity and Gabor deconvolved $s_{qi}(t)$ after phase correction using the known Q values is plotted in dotted green, which is not zero.

Although some multiples could be identified on the upgoing wavefield of a VSP through corridor filtering (Lines and Newrick, 2004), as first discussed by O'Doherty and Anstey (1971), internal multiples cause a nonstationary filtering effect that is essentially indistinguishable from anelastic attenuation and has come to be called stratigraphic filtering. Combination of both anelastic attenuation and stratigraphic filtering leads to a single combined effect that can be modelled by the constant-Q theory as an apparent Q. The apparent Q, intrinsic Q and stratigraphic Q are related by (Richards and Menke, 1983)

$$\frac{1}{Q_{apparent}} = \frac{1}{Q_{intrinsic}} + \frac{1}{Q_{stratigraphic}}. \quad (5.14)$$

Thus, the value of the apparent Q is lower than that of the intrinsic Q in the presence of internal multiples, leading to stronger attenuation effects such as more drift time delay. Figure 5.13 plots the same known interval intrinsic Q in solid blue and the known average intrinsic Q in solid black as Figure 5.8. The estimated average apparent Q from drift time estimation in Figure 5.12 bottom panel is plotted in dotted red and that from the residual drift time estimation in Figure 5.12 bottom panel is plotted in dotted green, whose values are both smaller than the known average intrinsic Q.

The nonstationary trace with both Q and internal multiple effects is tied to the well reflectivity by Gabor deconvolution without phase correction, or with phase correction calculated

from the known residual drift time, which is associated with the intrinsic Q, or with phase correction calculated from the SDTW estimated residual drift time, which is associated with the apparent Q, followed by time-variant amplitude balancing and time-variant constant-phase rotation. The final tying results are shown in Figure 5.14 in which the well reflectivities are plotted three times in blue while its estimates are in red. We can see that the nonstationary trace is best tied to the well reflectivity after phase correction, which is associated with the apparent Q. As a quality control, the time-variant constant-phase differences used to rotate those reflectivity estimates and the time-variant crosscorrelation coefficients at lag zero between those final estimates and the well reflectivity are plotted in Figure 5.15. The case that the nonstationary trace is multiple free and its phase is corrected after Gabor deconvolution using the intrinsic Q is also shown for comparison. As we can see, in the presence of internal multiples, Gabor deconvolved $s_{qi}(t)$ can have the smallest residual phase and maximum correlation with the well reflectivity by using the apparent Q to correct its phase, but the final correlation is still worse than the multiple-free case.

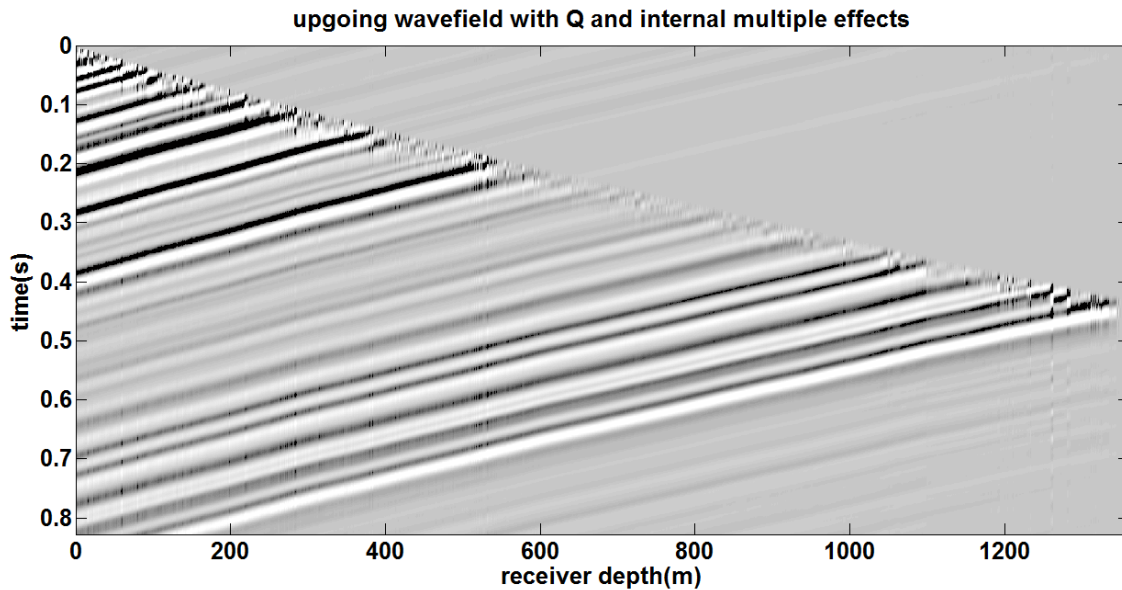


Figure 5.11: The upgoing wavefield of the synthetic zero-offset VSP model with both Q and internal multiple effects.

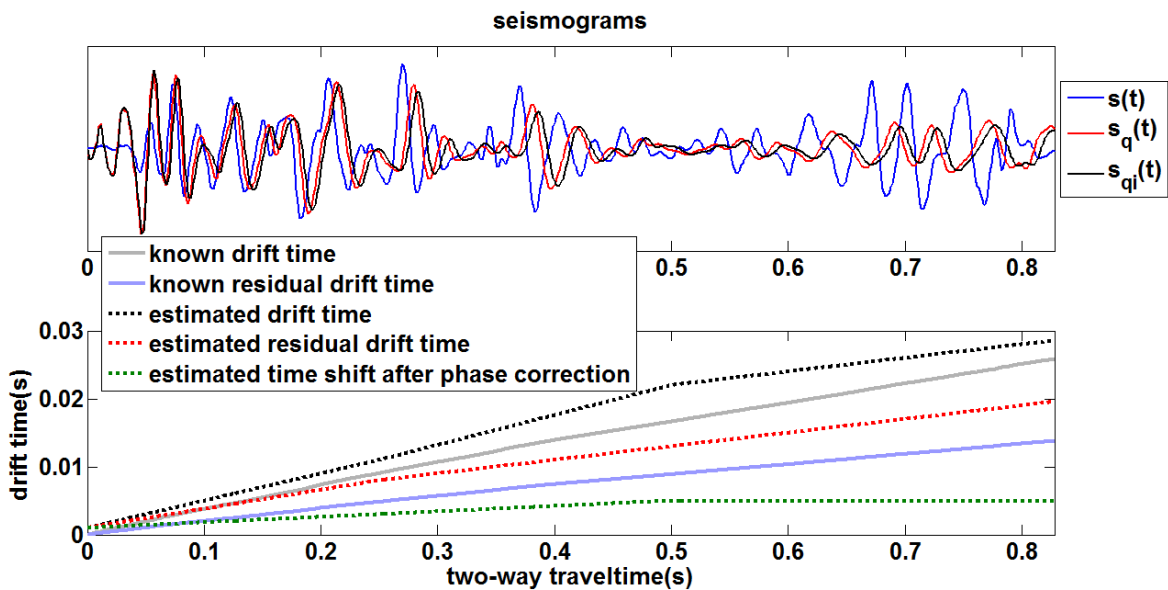


Figure 5.12: The stationary seismogram $s(t)$, the nonstationary trace with Q effects only $s_q(t)$, the nonstationary trace with both Q and internal multiple effects $s_{qi}(t)$ (top). The estimated drift time and residual drift time sequences compared to the known ones (bottom).

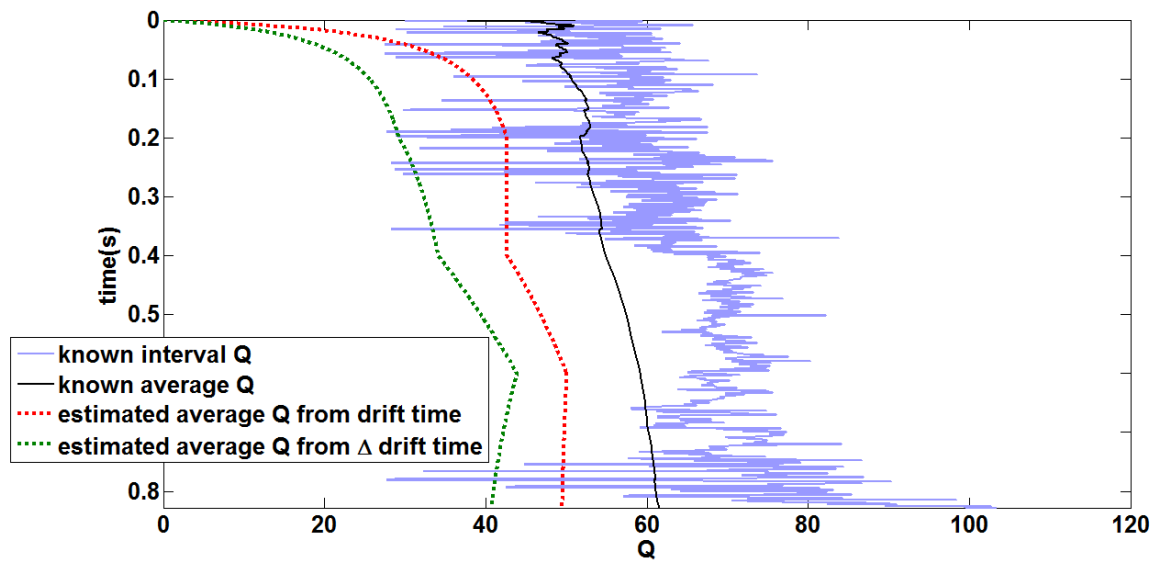


Figure 5.13: The known interval intrinsic Q , known average intrinsic Q , estimated average apparent Q from drift time estimation and that from residual drift time estimation in the presence of internal multiples.

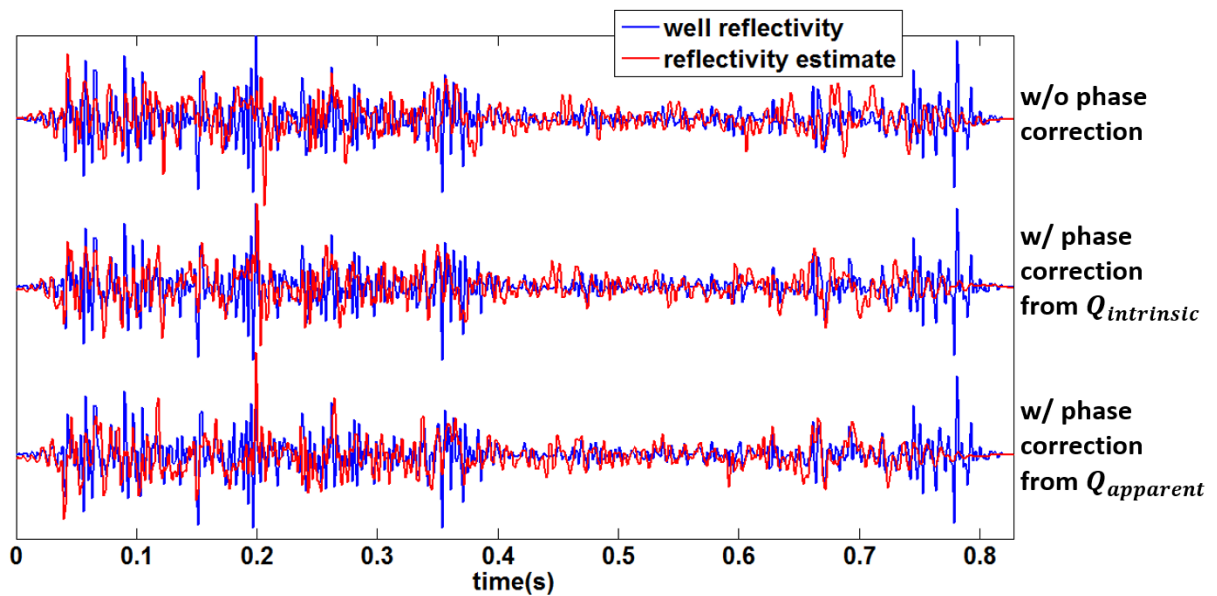


Figure 5.14: The reflectivity estimate without phase correction (top), with phase correction associated with the intrinsic Q (middle) and with phase correction associated with the apparent Q (bottom) compared to the well reflectivity.

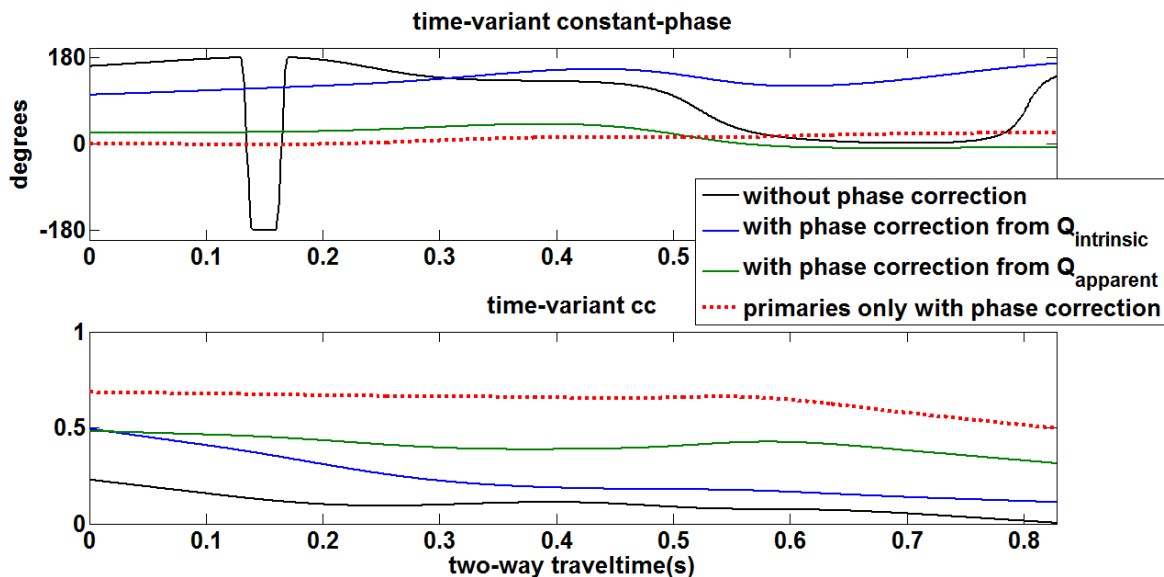


Figure 5.15: The time-variant constant-phase differences between the well reflectivity and Gabor deconvolved $s_{qi}(t)$ without phase correction, with phase correction associated with the intrinsic Q, with phase correction associated with the apparent Q and Gabor deconvolved $s_q(t)$ with phase correction associated with the intrinsic Q (top). The time-variant crosscorrelation coefficients at lag zero between the well reflectivity and its final estimates (bottom).

5.3 Seismic-to-well ties on Hussar field data

5.3.1 Data preparation

The Hussar seismic data is processed through a flow of scaling and noise attenuation, spiking deconvolution, statics and velocity analysis, normal moveout removal, common depth point stack and migration (Lloyd, 2013). Figure 5.16 shows the fully processed zero-offset seismic section. At each well location, the nearest 5 seismic traces are averaged to tie the corresponding synthetic seismograms.

Figure 5.17 shows the density and P-wave velocity logs after a log editing process of removing null values, clipping unrealistic values and adding overburdens. Each overburden linearly extends the average value of the top 10 sonic or density log samples to the starting value

at surface. The starting value for the density logs is 1500 kg/m^3 and that for the P-wave sonic logs is $1000 \text{ } \mu\text{s/m}$. Five tops called Basal Belly River, Base Fish Scales, Viking, Mannville and Medicine River Coal are denoted at the corresponding depth of each well, except that Medicine River Coal is missing at well 14-27. The subsurface structure is essentially flat in the Hussar area but the same tops appear deeper at well 12-27 than those of the other two wells. This is because the logs are measured with respect to the kelly bushing, whose elevation varies with the surface elevation and is significantly higher at well 12-27 than that at the other two wells (Margrave et al., 2012). In Figure 5.18, a normal incident P-wave reflectivity is calculated from each well and is plotted with respect to the two-way traveltimes converted from the depth using the sonic log values.

Next a residual wavelet is estimated from each average trace by smoothing its amplitude spectrum and applying a zero phase (Cui and Margrave, 2014). The residual wavelet is necessary to bandlimit the well reflectivity to the same frequency band of the seismic data. A zero-phase wavelet is symmetrical about time zero to make the maximum amount of energy in the wavelet be centered at the reflection coefficients, which is required by both interpretation and impedance inversion. All the three estimated wavelets are plotted in Figure 5.19 and they look very similar to each other.

Convolving a well reflectivity with the zero-phase wavelet estimated at the well location, a synthetic seismogram is created and is compared to the corresponding average trace in Figure 5.20. Their events are not tied to each other and the overall crosscorrelation coefficient at lag zero is very small at each well location. Figure 5.21 plots the synthetic seismograms on the 2-D seismic section in the same gray level. The tops are denoted at the corresponding two-way

traveltime converted from their depth using the sonic logs. We observe that none of the same well formations are tied to the same seismic events.

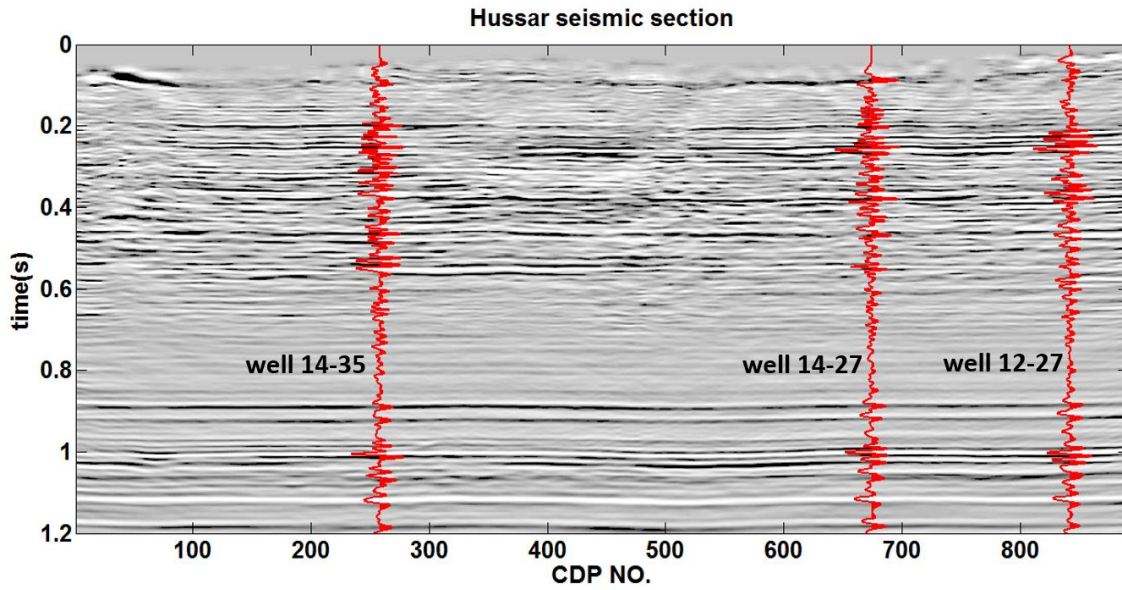


Figure 5.16: The 2-D seismic section after processing and migration. The three wiggle traces in red are the average traces at the corresponding well locations.

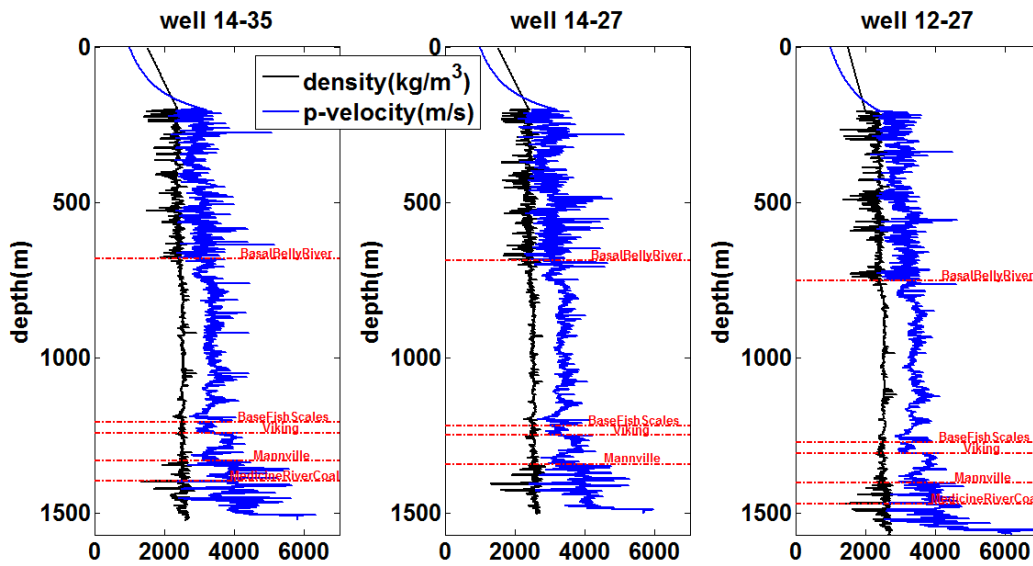


Figure 5.17: The density log and P-wave velocity log from each well after being edited.

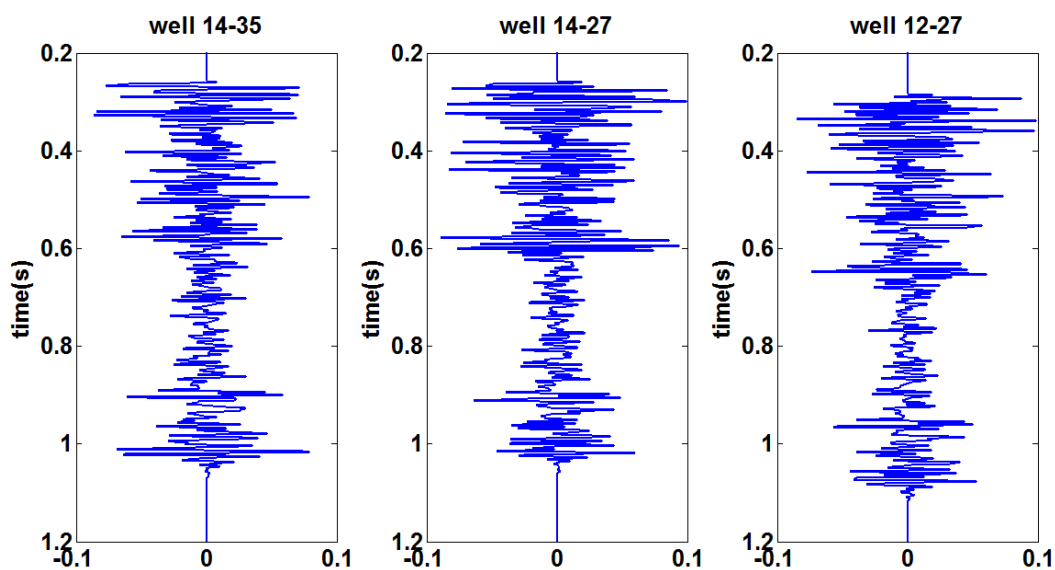


Figure 5.18: Reflectivity calculated from each well.

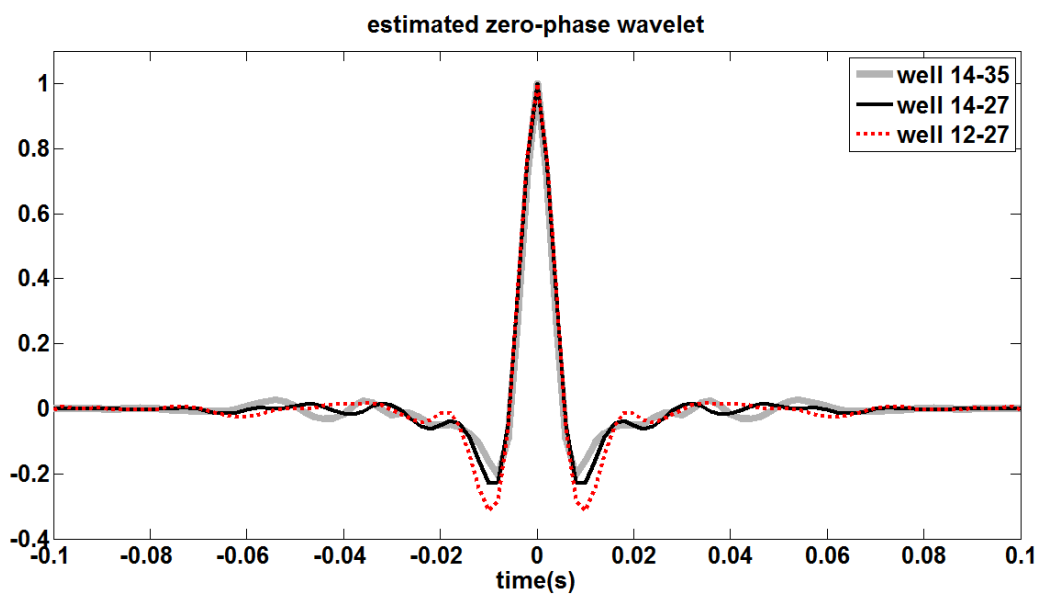


Figure 5.19: The zero-phase wavelet estimated from the average trace at each well location.

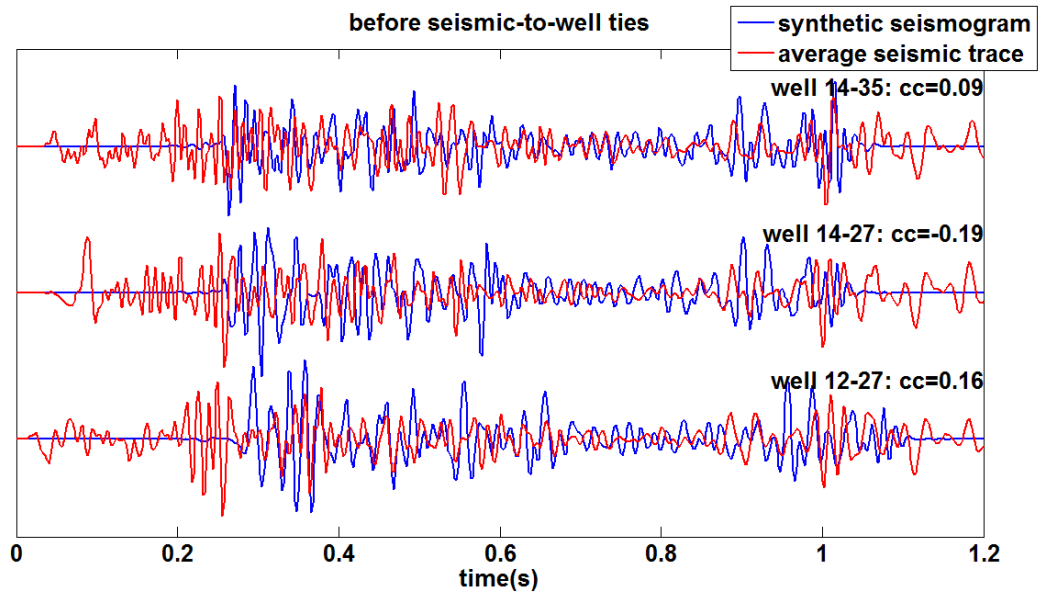


Figure 5.20: The synthetic seismogram and the average trace at the corresponding well location before being tied. The cc values annotated are their overall crosscorrelation coefficients at lag zero.

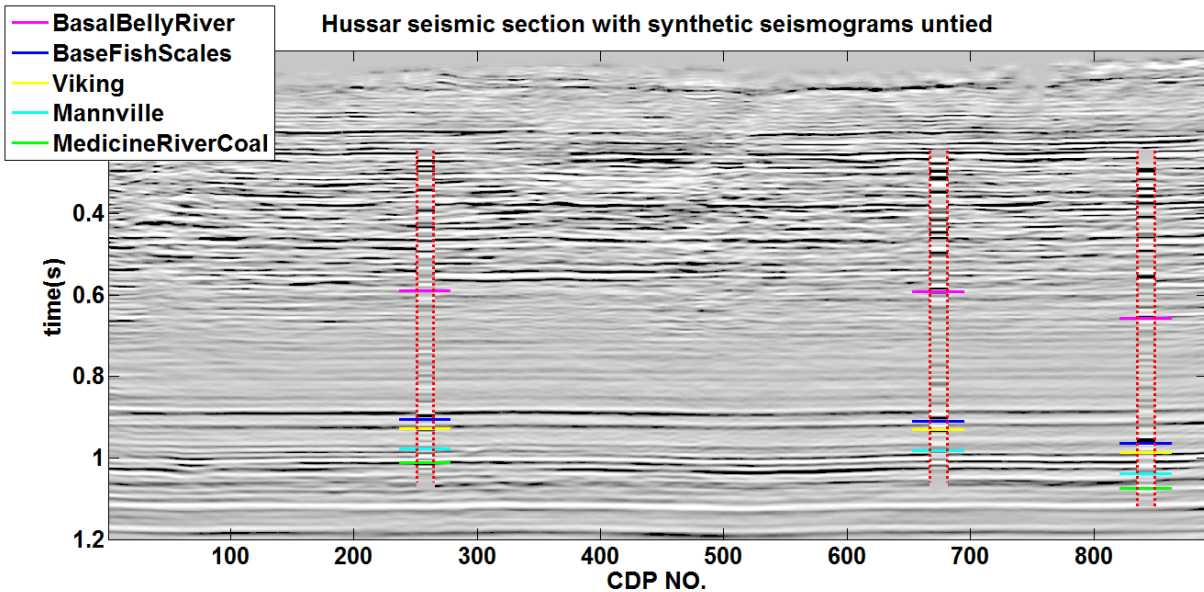


Figure 5.21: The 2-D seismic section, on top of which are the untied synthetic seismograms at the corresponding well locations separated by the dotted red lines.

5.3.2 *Seismic-to-well ties*

Without Q values or a check-shot/VSP survey available, SDTW is used to estimate the time shifts between the synthetic seismograms and the average seismic traces automatically. Figure 5.22 top panel shows the estimated time shifts using a coarse sample interval of 100 samples, namely 0.2 s. The time shifts are attributed to the combination of the residual drift time and overestimated sonic overburden, so they are all less than zero although they are getting larger with longer traveltime. The absolute values of the time shifts at well 12-27 are larger than those of the other two wells by a rough constant, resulting from the fact that its reference depth (the kelly bushing elevation) is higher than that of the other two wells. The accuracy of the time shift estimation can be verified by the fact that all the three time shift sequences have similar slopes because of the flat subsurface geological features in the Hussar area.

The timing of each well reflectivity is corrected by the corresponding time shifts and is plotted on top of the original reflectivity in Figure 5.23. Convolving the time shifted reflectivity with the corresponding zero-phase residual wavelet in Figure 5.19, the reconstructed synthetic seismogram is plotted in Figure 5.24 compared to the corresponding average trace at each well location. Note that in this time calibration step, it is the timing of the well reflectivity that is being corrected instead of warping the original synthetic seismograms, so that their embedded zero-phase wavelets are not destroyed.

Next the time-variant constant-phase differences and amplitude scalar functions between the synthetic seismograms and the average traces in Figure 5.24 are calculated and plotted in Figure 5.22 middle and bottom panels. They are then linearly interpolated and extrapolated in the horizontal direction because of the flat subsurface properties in the Hussar area. The 2-D time-variant constant-phase and the 2-D time-variant amplitude scalar are plotted in Figure 5.25 and

Figure 5.26 respectively. It can be seen that the traces near well 12-27 have relatively large phase errors at early times while the traces near well 14-27 have relatively large amplitude errors at middle times. Each seismic trace is phase rotated and amplitude balanced by the corresponding amounts. Since deconvolution is rarely perfect in its attempt to produce a zero-phase wavelet from the nonstationary minimum-phase wavelets, phase rotation is important to move the central peaks of the residual wavelets in the seismic traces to the positions of the reflection coefficients. Figure 5.27 shows that the synthetic seismograms after time calibration are now tied to the 2-D seismic section after phase rotation and amplitude balancing very well. The same well tops tie to the same seismic events, making major seismic horizons easy to be identified. In Figure 5.28, the correlation of each pair of the synthetic seismogram and the average trace is shown to be much improved after well tying compare to Figure 5.20.

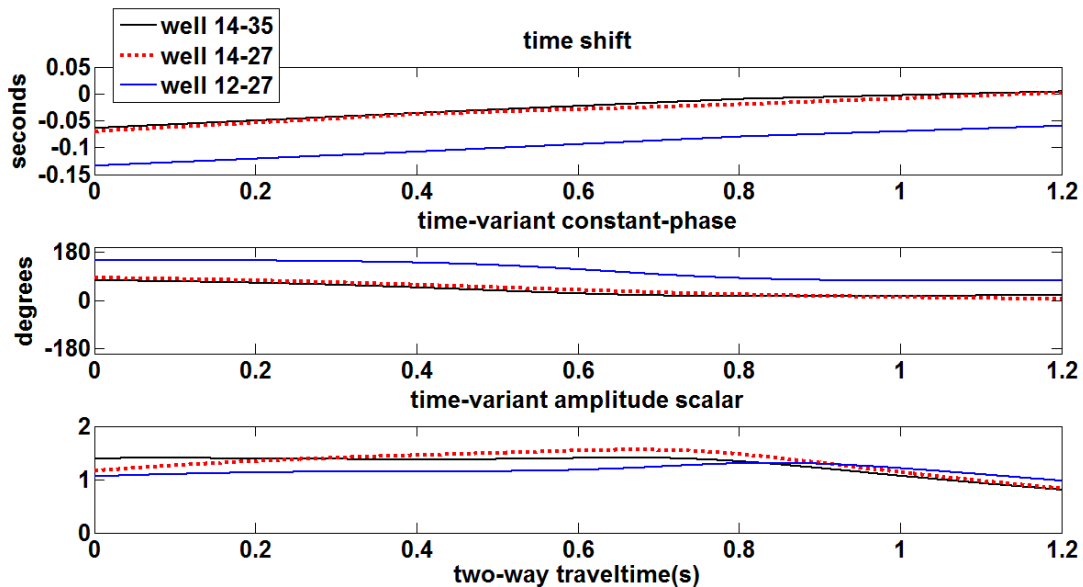


Figure 5.22: The time shifts between the synthetic seismogram and the average trace at the corresponding well location (top). The time-variant constant-phase difference between the average trace and the synthetic seismogram after time calibration at each well location (middle). The time-variant amplitude scalar function between the phase rotated average trace and the synthetic seismogram after time calibration at each well location (bottom).

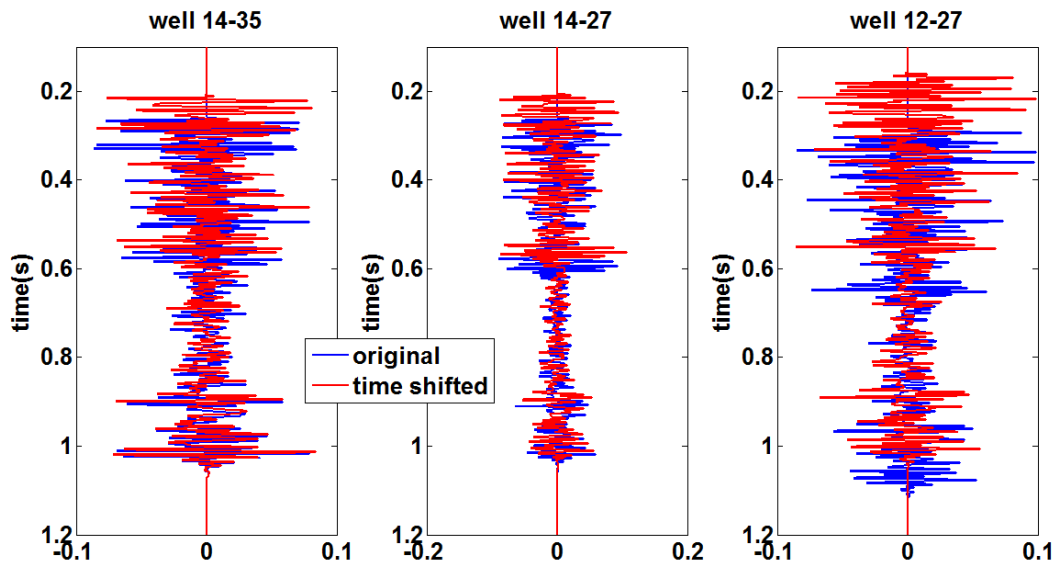


Figure 5.23: The original and time shifted reflectivities at each well.

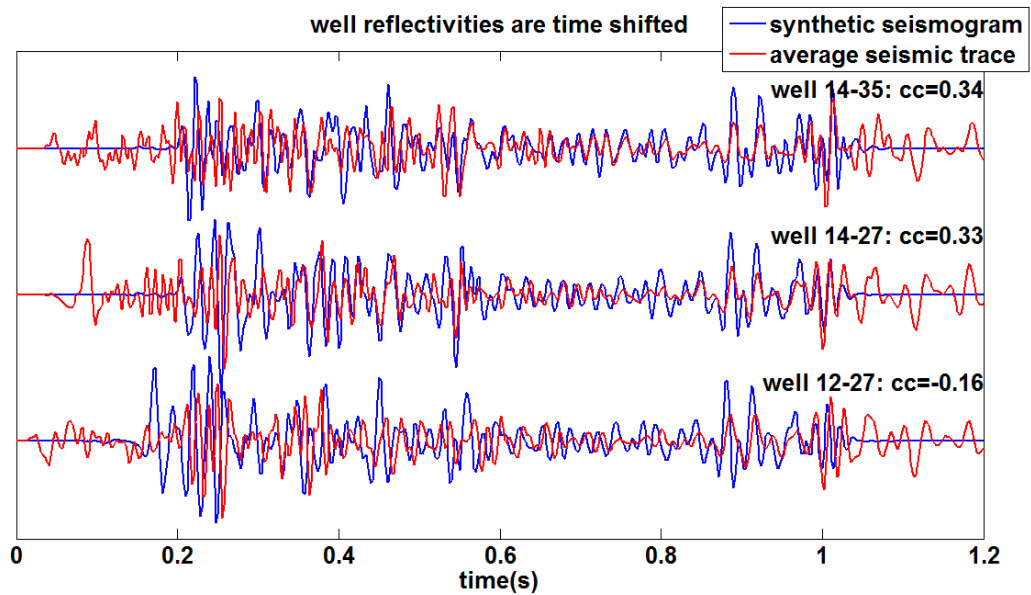


Figure 5.24: The reconstructed synthetic seismogram and the average trace at the corresponding well location after the timing of the reflectivity being corrected. The cc values annotated are their overall crosscorrelation coefficients at lag zero.

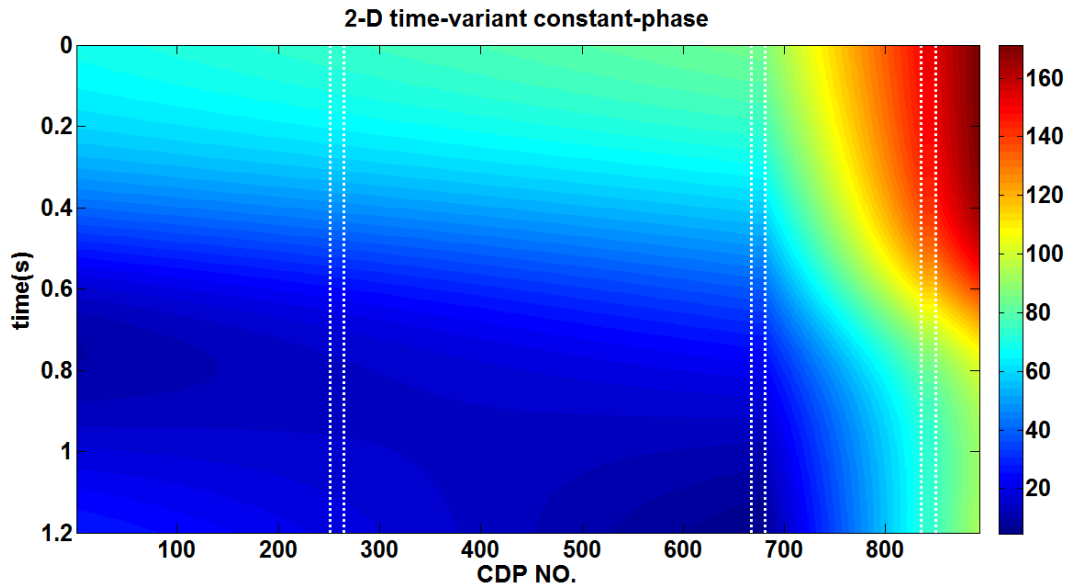


Figure 5.25: The 2-D time-variant constant-phase, on top of which are the phases used for interpolation and extrapolation at the corresponding well locations separated by the dotted white lines.

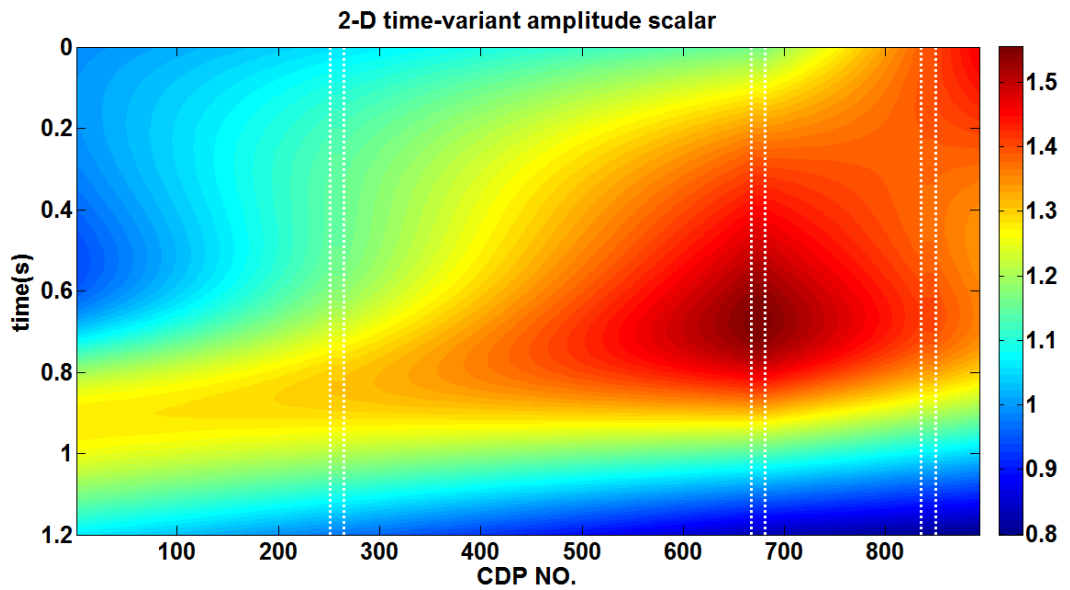


Figure 5.26: The 2-D time-variant amplitude scalar, on top of which are the scalars used for interpolation and extrapolation at the corresponding well locations separated by the dotted white lines.

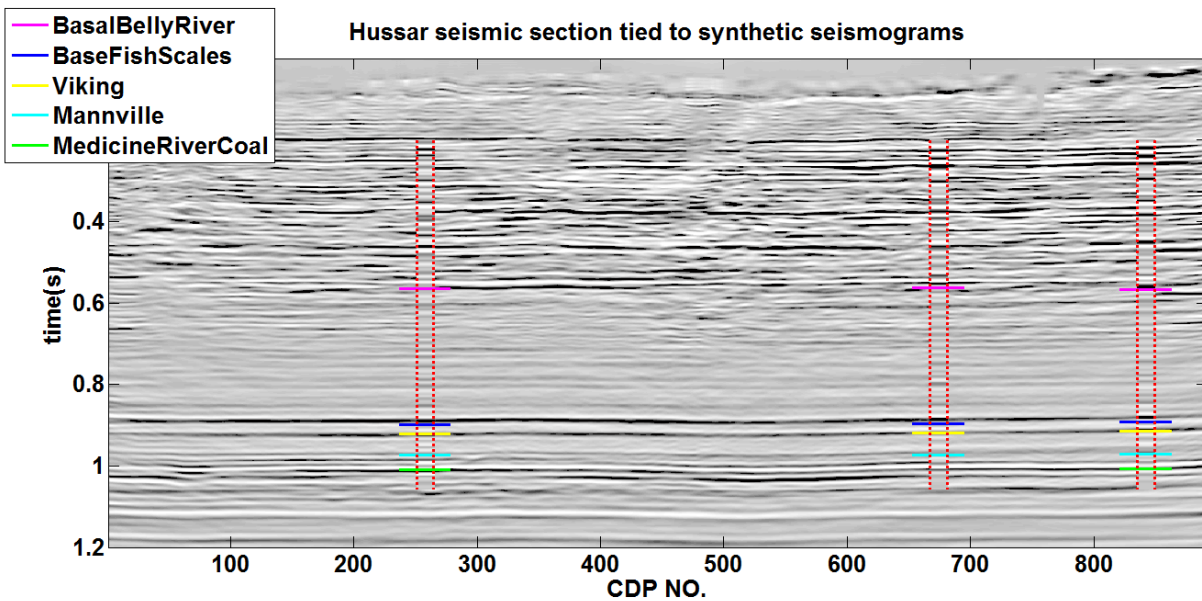


Figure 5.27: The 2-D seismic section after phase rotation and amplitude balancing, on top of which are the synthetic seismograms after time calibration at the corresponding well locations separated by the dotted red lines.

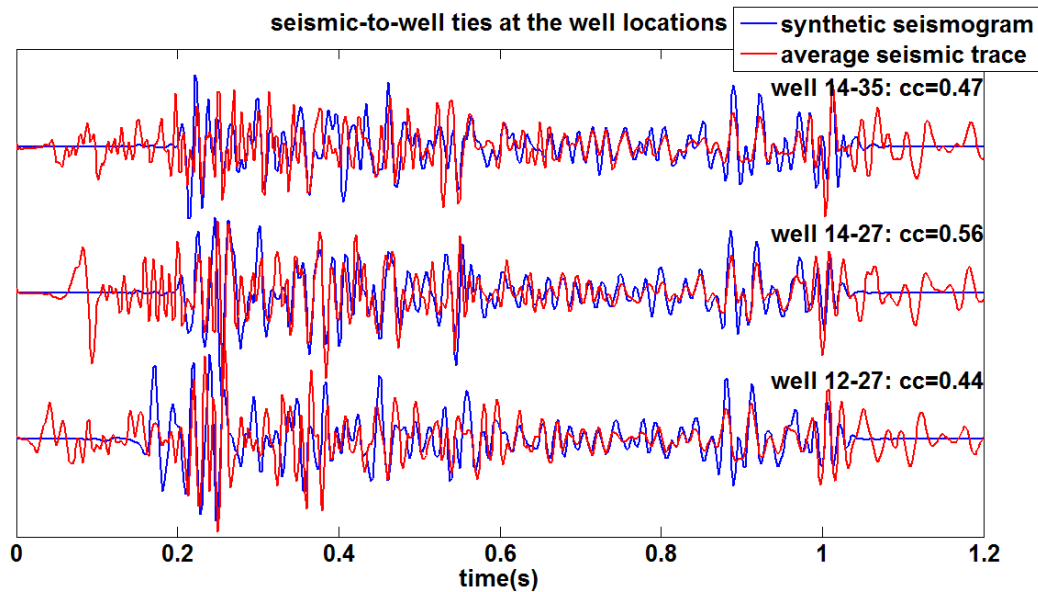


Figure 5.28: The synthetic seismogram and the average trace at the corresponding well location after being tied. The cc values annotated are their overall crosscorrelation coefficients at lag zero.

5.3.3 Bandlimited impedance inversion

Once the wells are tied to the seismic section, they can provide the low-frequency trend when the integrated seismic data is inverted into detailed impedance. The bandlimited impedance inversion (BLIMP) (Ferguson and Margrave, 1996) is a simple but powerful seismic inversion technique. The low frequency cut-off f_c and the high-end frequency f_h are two important parameters specified by the user. BLIMP estimates acoustic impedance from a seismic trace of bandwidth from f_c to f_h combined with a log impedance of bandwidth below f_c .

The impedance of the three wells are calculated with respect to two-way traveltime after their timing is corrected by the SDTW estimated time shifts. Then the well impedance is linearly interpolated and extrapolated in the horizontal direction for the inversion of each trace in the 2-D seismic section. Figure 5.29 shows the 2-D interpolated well impedance section.

The low frequency cut-off f_c should be the lowest reliable seismic frequency. Selecting its value too low, the impedance inversion will contain noise from the seismic. Selecting its value too high will cause the seismic data to be overwritten with the well log information, causing subtleties in the seismic to be erased (Lloyd, 2013). To determine the optimal value of f_c , a series of frequency values ranging from 1 to 20 Hz in an increment of 0.5 Hz is tested. The trace at each well location is inverted using different testing values of f_c , the corresponding well impedance and a high-end frequency f_h of 75 Hz. The 2-norm errors are calculated between each seismic impedance inversion and the corresponding low-pass filtered log impedance using $f_h=75$ Hz, and are plotted in Figure 5.30 with respect to the values of f_c . The errors drop rapidly with an increasing f_c and become stably small at about 3 Hz for the three wells, so 3 Hz is chosen as the optimal low frequency cut-off. Figure 5.31 shows the bandlimited impedance inversion of the

2-D seismic section using $f_c=3$ Hz and $f_h=75$ Hz, which is roughly consistent with the low-pass filtered log impedance at each well location. To qualitatively evaluate the accuracy of the seismic impedance inversion, Figure 5.32 compares the low-pass filtered log impedance I_{well} with the bandlimited seismic impedance inversion $I_{inversion}$ at the corresponding well location. Their percent error is calculated by

$$error = \frac{norm(I_{inversion} - I_{well})}{norm(I_{well})} \times 100 \quad (5.15)$$

where $norm$ is the 2-norm. It can be noticed that the percent error is relatively high at well 12-27 compared to the other two wells.

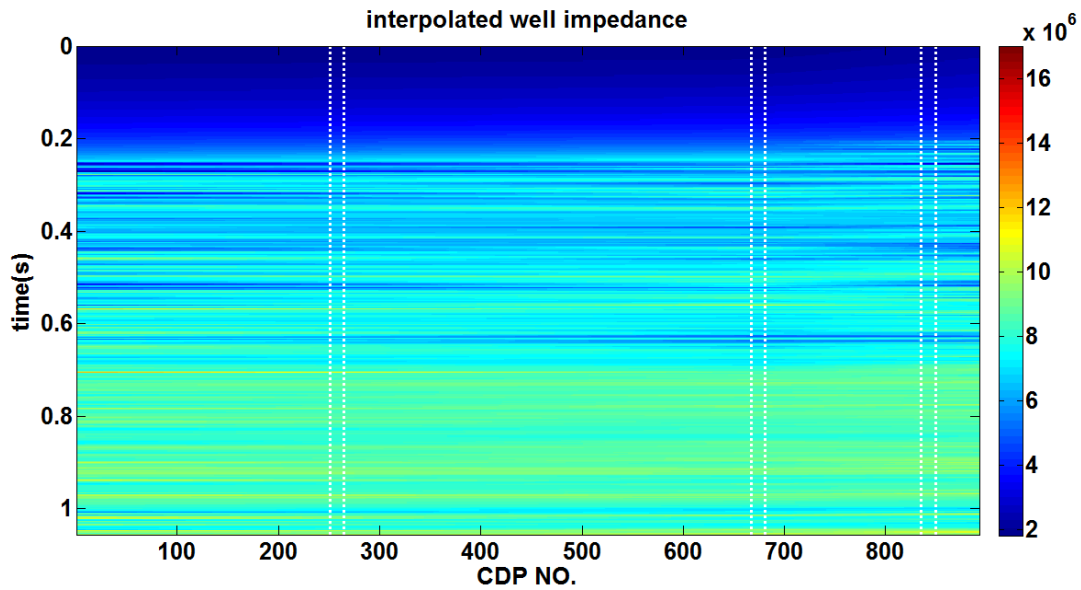


Figure 5.29: The 2-D interpolated well impedance, on top of which are the well impedance used for interpolation and extrapolation at the corresponding well locations separated by the dotted white lines.

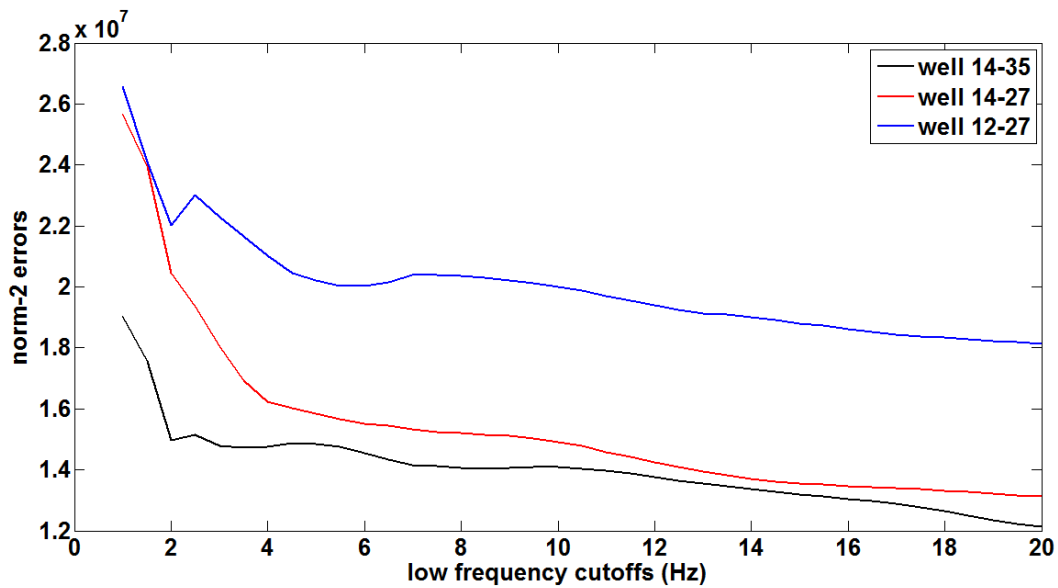


Figure 5.30: The 2-norm errors between the log impedance and the impedance inversion of the seismic trace at each well location using different low frequency cut-offs.

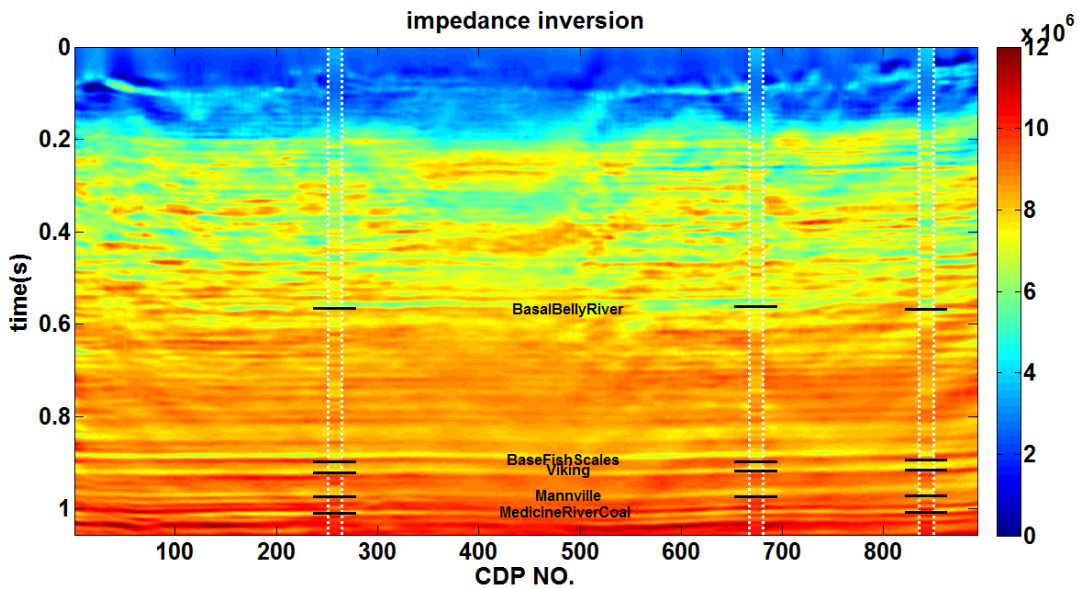


Figure 5.31: Bandlimited impedance inversion of the 2-D seismic section, on top of which are the low-pass filtered well impedance separated by the dotted white lines at the corresponding well locations with the tops annotated.

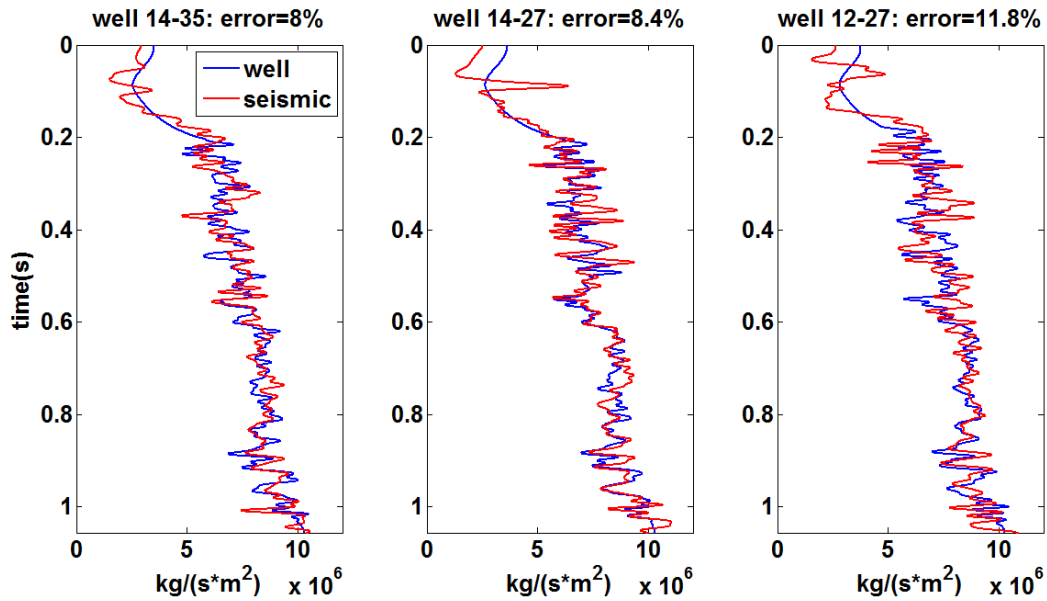


Figure 5.32: Comparison of the low-passed well impedance and the bandlimited seismic impedance inversion at each well location with their percent errors denoted.

5.3.4 Discussion

As is seen from the 2-D time-variant constant-phase section in Figure 5.25, the phase values are anomalously large around well 12-27. It is unrealistic to rotate the seismic traces by such large phase angles. The phase anomaly may be an indication of insufficient time shift correction of well 12-27 since its reference depth level is higher than that of the other two wells. To verify this guess, a second iteration of time calibration process is applied. The time shifts between the previously time corrected synthetic seismogram and the average seismic trace at each well location in Figure 5.24 are estimated by SDTW again and are plotted in Figure 5.33 top panel. Noticeable time shift amounts are detected even after the first iteration of time calibration, especially at well 12-27. Next, the timing of the reflectivity is further corrected by these time shifts again to construct the synthetic seismogram with twice time calibration, whose time-variant constant-phase difference with the average trace at each well location is calculated

and plotted in Figure 5.33 middle panel. The phase is smaller than that in the first iteration shown in Figure 5.22 middle panel, indicating that the inadequate time shift correction in the first iteration biases the following constant-phase estimation. A third iteration of time calibration is employed in the same way and the results are shown in Figure 5.34. The time shifts are all reduced to zero and the time-variant constant-phase difference is the same as that in the second iteration, verifying that the timing of the three wells is sufficiently corrected after two iterations. The reason why time calibration in this case needs several iterations to converge may be that the SDTW estimated time shifts are used to correct the timing of the reflectivity instead of warping the synthetic seismogram, the latter of which is required by the objective of the SDTW algorithm, making this optimization problem nonlinear.

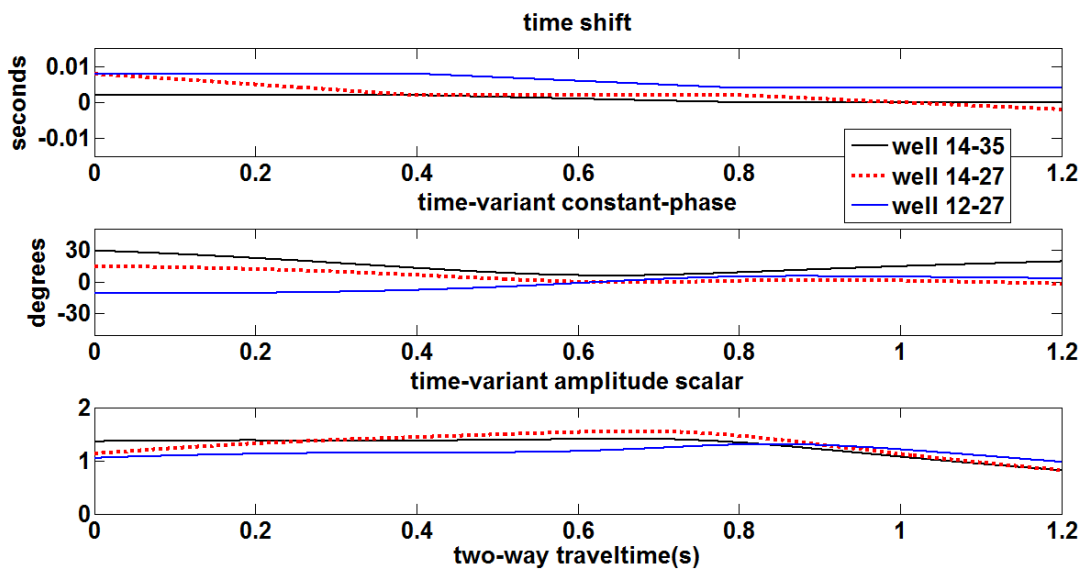


Figure 5.33: The results in the second iteration of time calibration are shown. The time shifts between the average trace and the synthetic seismogram after time calibration once (top). The time-variant constant-phase difference between the average trace and the synthetic seismogram after time calibration twice (middle). The time-variant amplitude scaler function between the phase rotated average trace and the synthetic seismogram after time calibration twice (bottom).

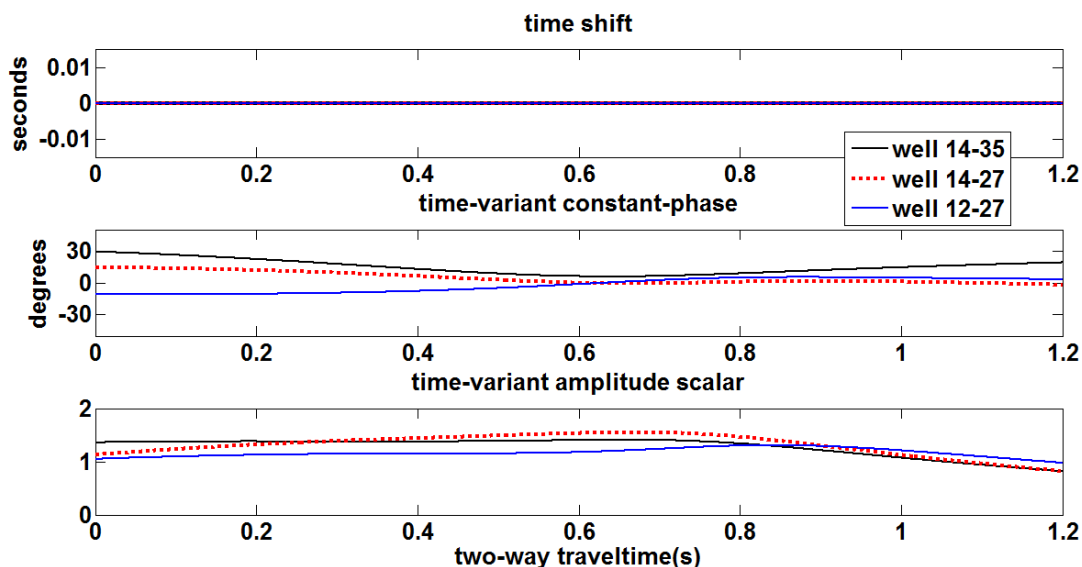


Figure 5.34: The results in the third iteration of time calibration are shown. The time shifts between the average trace and the synthetic seismogram after time calibration twice (top). The time-variant constant-phase difference between the average trace and the synthetic seismogram after time calibration three times (middle). The time-variant amplitude scalar function between the phase rotated average trace and the synthetic seismogram after time calibration three times (bottom).

After two iterations, the time-variant constant-phase difference (Figure 5.33 or Figure 5.34 middle panel) and the time-variant amplitude scalar (Figure 5.33 or Figure 5.34 bottom panel) at three well locations are linearly interpolated and extrapolated in the horizontal direction, shown in Figure 5.35 and Figure 5.36 respectively. The phase values are much smaller than those in the first iteration in Figure 5.25 while the 2-D amplitude scalar section is almost the same as Figure 5.26. The seismic traces are phase rotated and amplitude balanced by the amount calculated in the second iteration and the final 2-D seismic section is displayed in Figure 5.37, on top of which are the synthetic seismograms after time calibration twice. The well tying result is visually similar to that with only one iteration of time calibration as shown in Figure 5.27. Each

pair of the tied synthetic seismogram and the average trace is plotted in Figure 5.38 and their overall crosscorrelation coefficients are all increased from the first iteration in Figure 5.28. The time-variant crosscorrelation coefficients between the synthetic seismogram and the seismic trace before well tying, after well tying with time calibration once and after well tying with time calibration twice are calculated are plotted in Figure 5.39 for each well location, showing that the second iteration of time calibration considerably improves the well tying at early times for well 12-27.

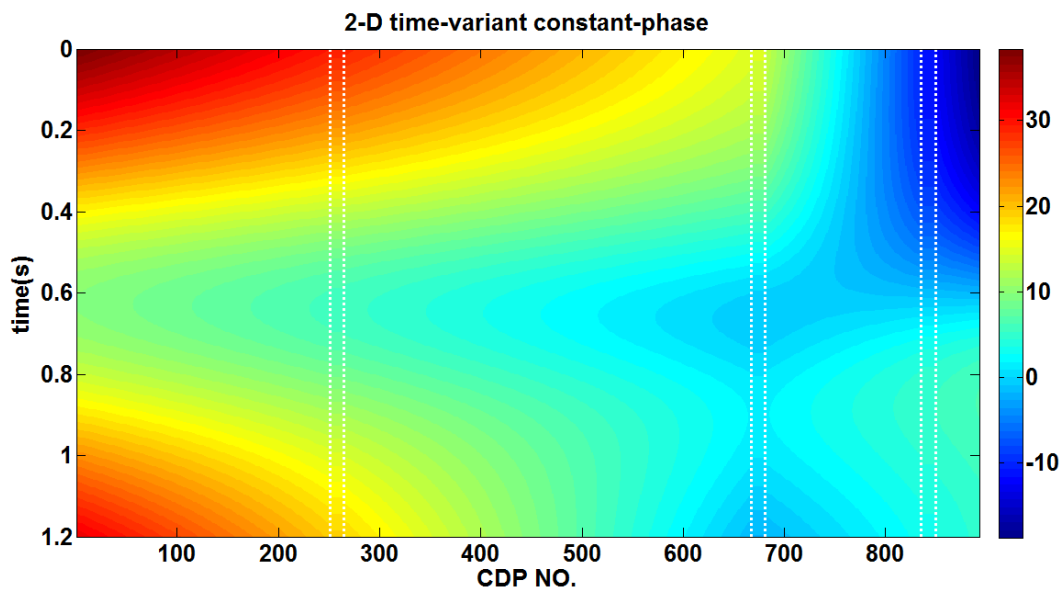


Figure 5.35: The 2-D time-variant constant-phase after two iterations, on top of which are the phases used for interpolation and extrapolation at the corresponding well locations separated by the dotted white lines.

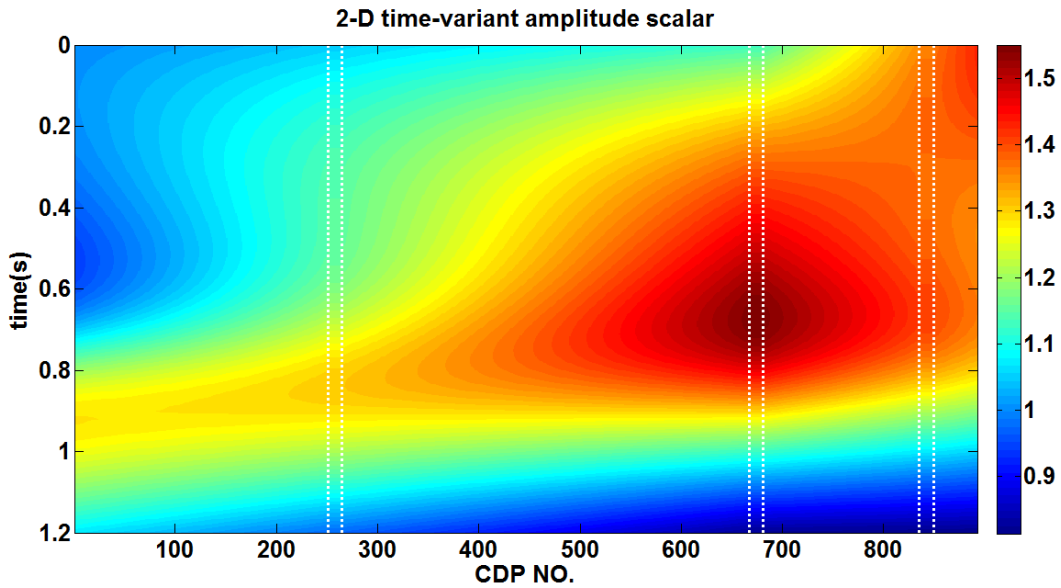


Figure 5.36: The 2-D time-variant amplitude scalar after two iterations, on top of which are the scalars used for interpolation and extrapolation at the corresponding well locations separated by the dotted white lines.

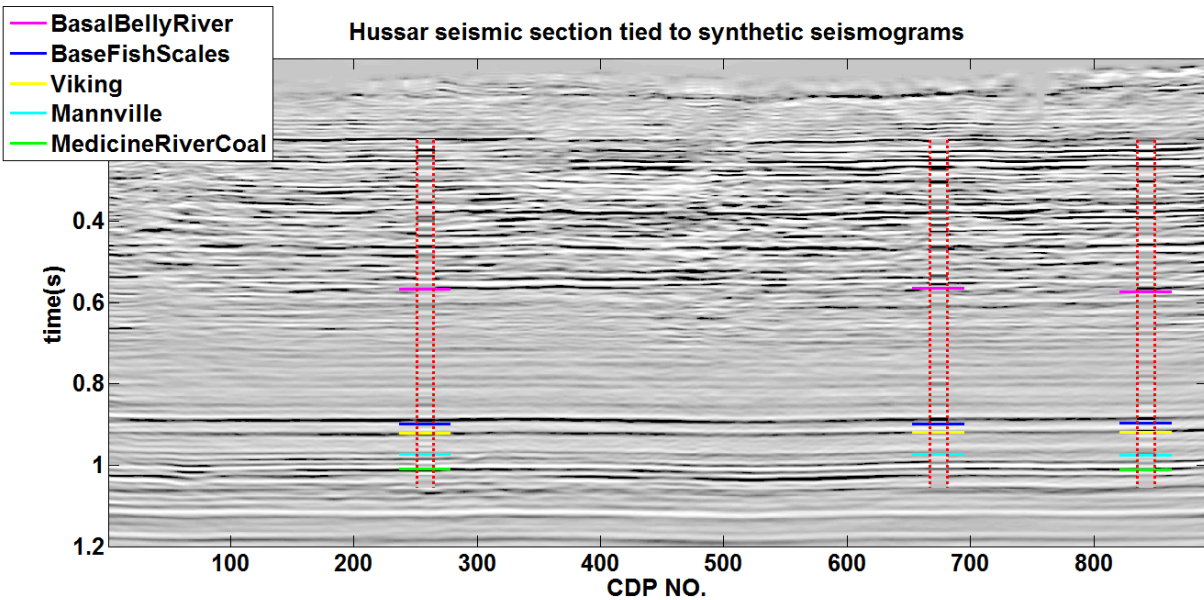


Figure 5.37: The final well tying results after two iterations of time calibration are shown. The 2-D seismic section after phase rotation and amplitude balancing, on top of which are the synthetic seismograms after time calibration twice at the corresponding well locations separated by the dotted red lines.

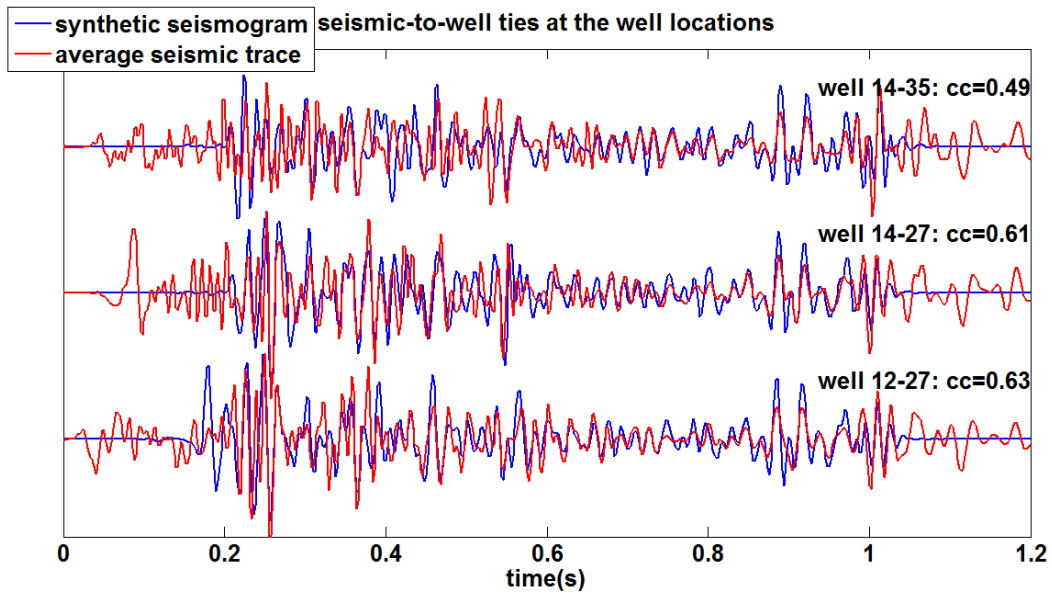


Figure 5.38: The synthetic seismogram and the average trace at the corresponding well location after being tied through two iterations of time calibration. The cc values annotated are their overall crosscorrelation coefficients at lag zero.

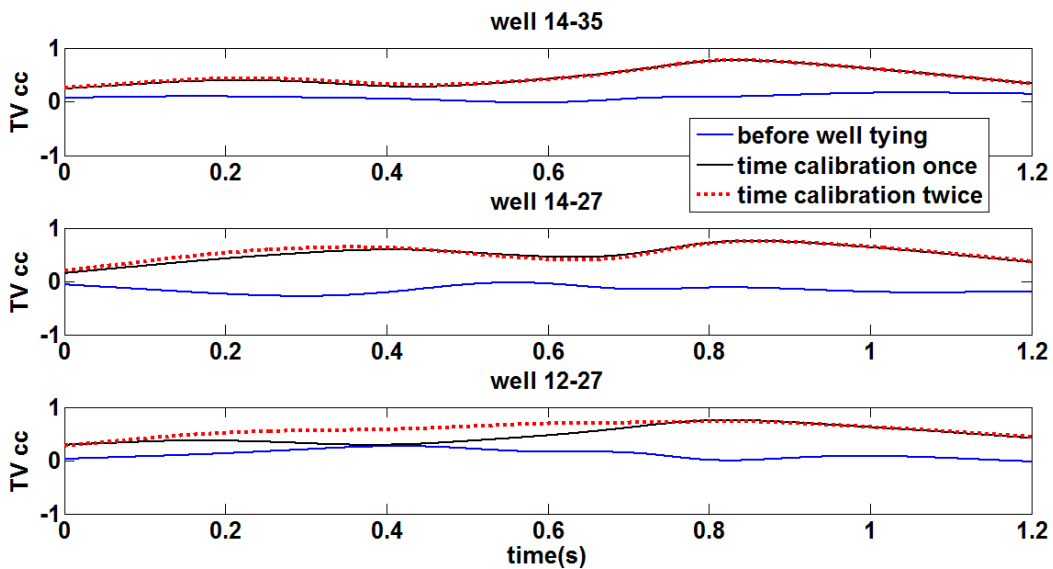


Figure 5.39: The time-variant crosscorrelation coefficients between the synthetic seismogram and the seismic trace before well tying, after well tying with time calibration once and after well tying with time calibration twice.

With the wells tied to the seismic section after two iterations of time calibration, the seismic data is inverted to the bandlimited impedance shown in Figure 5.40 using the same values of f_c and f_h . Figure 5.41 also compares the percent error between the low-pass filtered log impedance with the bandlimited seismic impedance inversion at each well location. The error is slightly higher at well 14-35 while is lower at well 14-27 and well 12-27 than that with well tying of one time calibration iteration. Similarly, the impedance percent error is calculated between the seismic impedance inversion and the interpolated well impedance at every CDP location. Figure 5.42 compares the errors with one and two iterations of time calibration in the well tying. The second iteration is seen to bring down the errors significantly around well 12-27, verifying better seismic-to-well ties.

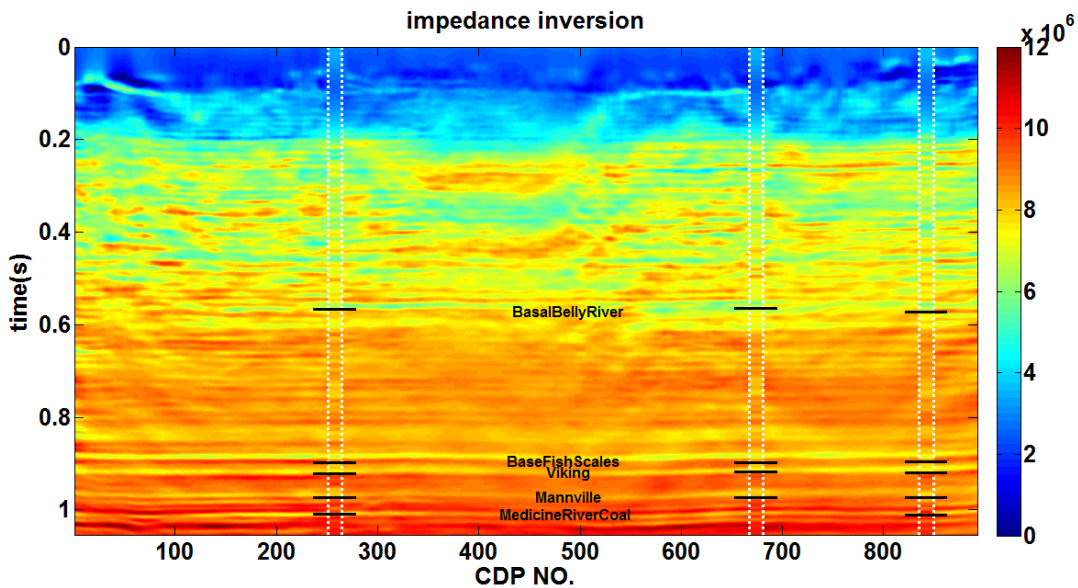


Figure 5.40: Bandlimited impedance inversion of the 2-D seismic section, with two iterations of time calibration in the well tying, on top of which are the low-pass filtered well impedance separated by the dotted white lines at the corresponding well locations with the tops annotated.

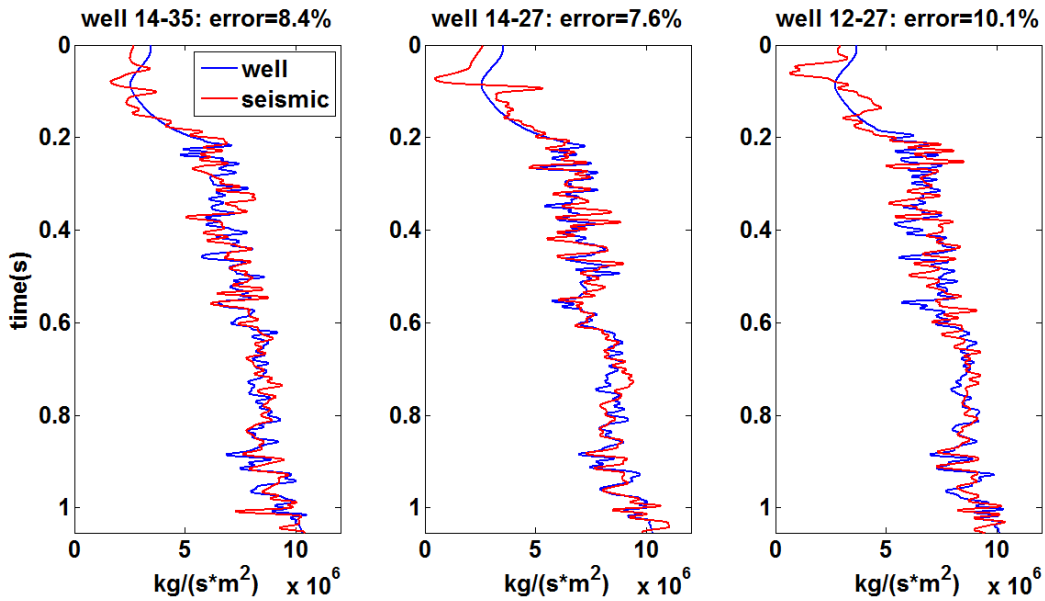


Figure 5.41: Comparison of the low-passed well impedance and the bandlimited seismic impedance inversion with two iterations of time calibration in the well tying. Their impedance percent errors are denoted.

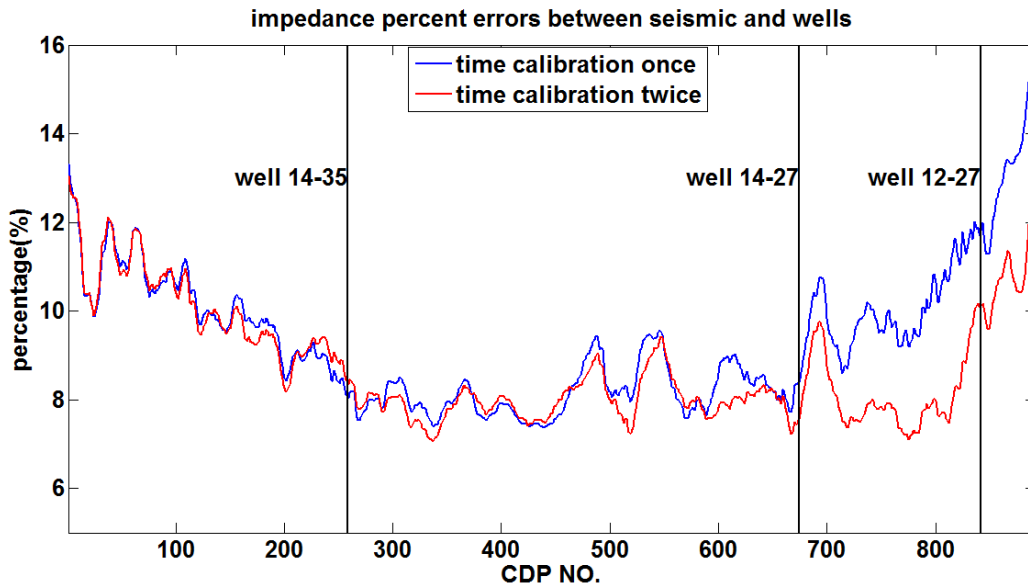


Figure 5.42: The impedance percent errors between the seismic impedance inversion and the interpolated well impedance at every CDP location, with one and two iterations of time calibration in the well tying.

5.4 Summary

- Smooth dynamic time warping can accurately estimate the drift time and the residual drift time automatically without knowledge of Q or a check-shot or a VSP survey. Average Q values can be roughly calculated from the estimated drift time or residual drift time.
- A roughly correct time-invariant Q can plausibly correct the phase errors of Gabor deconvolved nonstationary seismic trace to tie the well reflectivity.
- In the presence of internal multiples, smooth dynamic time warping estimates drift time or residual drift time associated with apparent Q , including both intrinsic and stratigraphic effects. Gabor deconvolved nonstationary trace using the apparent Q for phase correction can be tied to the well reflectivity at best, but the final correlation is still worse than the multiple-free case.
- The time shifts estimated between synthetic seismograms and seismic traces are the combination of drift time and sonic overburden estimation errors when tying Hussar wells to the field seismic data.
- The fact that the geological structure is horizontally flat in the Hussar area leads to similar time shift characters between the synthetic seismograms and the seismic traces at three well locations. It also validates the linear interpolation and extrapolation of the time-variant constant-phase and the time-variant scalar from the well locations to other CDP locations horizontally.
- The estimated time shifts are used to calibrate the timing of the reflectivity, instead of warping the synthetic seismogram required by the objective of the SDTW algorithm, to reserve the embedded zero-phase wavelets but making this optimization problem nonlinear and converge only after several iterations. For this Hussar dataset, the first

iteration of time calibration is not sufficient, leading to a constant-phase estimation bias.

After two iterations, the time shifts are adequately corrected and the constant-phase difference is reasonably small.

- After seismic-to-well ties, the same well tops are tied to the same seismic events, making major seismic horizons easy to be identified. The correlation of the synthetic seismogram and the average trace at each well location is much increased compared to that before well tying.
- The bandlimited impedance inversion of the Hussar seismic data using a low-frequency cut-off of 3 Hz and a high-end frequency of 75 Hz is shown to be a good approximation to the subsurface properties. The second iteration of time calibration significantly reduces the percent errors around well 12-27 between the seismic inversion and well impedance, verifying better seismic-to-well ties.

Chapter Six: Conclusions

- Smooth dynamic time warping can accurately estimate smooth time shifts between two traces automatically to get a good correlation between them. Dynamic time warping or smooth dynamic time warping is more sensitive to the rapidly varying time shifts than time-variant crosscorrelation.
- The constant-Q theory predicts seismic wavelet evolution with amplitude decay and minimum phase dispersion. Compared to the stationary trace, the nonstationary trace shows progressive attenuation effects such as the diminishing amplitude, the widening waveforms and the delayed events.
- By comparing two traces within a sliding Gaussian window, time-variant amplitude balancing, time-variant constant-phase rotation and time-variant crosscorrelation can correct nonstationary effects that are very slowly time variant.
- Stationary deconvolution on a nonstationary seismic trace results in large amplitude and phase errors, resulting from deconvolving a single wavelet estimated within a target zone from the nonstationary trace with embedded evolving wavelets. These errors are nonstationary and difficult to be corrected for by time-variant amplitude balancing and time-variant constant-phase rotation compared to the well control.
- Running Gabor deconvolution on the nonstationary trace can get reflectivity estimate tying the well reflectivity in amplitude and spectral content, but has phase errors which are more complex than those that can be solved by time-variant constant-phase rotation.
- Gabor deconvolution accurately estimates the amplitude spectra of the propagating wavelets.

- Gabor deconvolution calculates the phase spectra of the propagating wavelets by the digital Hilbert transform, which integrates within the seismic frequency band and corrects the drift time to the Nyquist frequency only.
- By correcting the estimated wavelet phase to the well logging frequency, the Gabor deconvolved trace can be well tied to the known reflectivity with very little amplitude and phase errors.
- Gabor deconvolution with either phase correction or residual drift time correction can tie the nonstationary seismic trace to well reflectivity accurately knowing the Q values and the well logging frequency. Smooth dynamic time warping can estimate the residual drift time without knowledge of Q or the well logging frequency, and the estimation is more accurate than time-variant crosscorrelation.
- Smooth dynamic time warping can accurately estimate the drift time and the residual drift time automatically without knowledge of Q or a check-shot or a VSP survey. Average Q values can be roughly calculated from the estimated drift time or residual drift time.
- A roughly correct time-invariant Q can plausibly correct the phase errors of Gabor deconvolved nonstationary seismic trace to tie the well reflectivity.
- In the presence of internal multiples, smooth dynamic time warping estimates drift time or residual drift time associated with apparent Q, including both intrinsic and stratigraphic effects. Gabor deconvolved nonstationary trace using the apparent Q for phase correction can be tied to the well reflectivity at best, but the final correlation is still worse than the multiple-free case.

- In seismic-to-well ties of Hussar field data, the time shifts estimated between synthetic seismograms and seismic traces are the combination of drift time and sonic overburden estimation errors when tying Hussar wells to the field seismic data.
- The fact that the geological structure is horizontally flat in the Hussar area leads to similar time shift characters between the synthetic seismograms and the seismic traces at three well locations. It also validates the linear interpolation and extrapolation of the time-variant constant-phase and the time-variant scalar from the well locations to other CDP locations horizontally.
- The estimated time shifts are used to calibrate the timing of the reflectivity, instead of warping the synthetic seismogram required by the objective of the SDTW algorithm, to reserve the embedded zero-phase wavelets but making this optimization problem nonlinear and converge only after several iterations. For this Hussar dataset, the first iteration of time calibration is not sufficient, leading to a constant-phase estimation bias. After two iterations, the time shifts are adequately corrected and the constant-phase difference is reasonably small.
- After seismic-to-well ties, the same well tops are tied to the same seismic events, making major seismic horizons easy to be identified. The correlation of the synthetic seismogram and the average trace at each well location is much increased compared to that before well tying.
- The bandlimited impedance inversion of the Hussar seismic data using a low-frequency cut-off of 3 Hz and a high-end frequency of 75 Hz is shown to be a good approximation to the subsurface properties. The second iteration of time calibration significantly reduces

the percent errors around well 12-27 between the seismic inversion and well impedance, verifying better seismic-to-well ties.

References

- Barnes, A. E., 2007, A tutorial on complex seismic trace analysis: *Geophysics*, 72, W33-W43.
- Cheng, P., 2013, Anelastic attenuation in seismic data: modeling, measurement, and correction: Ph.D. thesis, University of Calgary.
- Compton, S., and Hale, D., 2014, Estimating V-P/V-S ratios using smooth dynamic image warping: *Geophysics*, 79, V201-V215.
- Cui, T., and Margrave, G. F., 2014, Seismic wavelet estimation: CREWES Research Report, 26.
- Ferguson, R. J., and Margrave, G. F., 1996, A simple algorithm for bandlimited impedance inversion: CREWES Research Report, 8.
- Futterman, W. I., 1962, Dispersive Body Waves: *Journal of Geophysical Research*, 67, 5279-5291.
- Ganley, D. C., 1981, A method for calculating synthetic seismograms which include the effects of absorption and dispersion: *Geophysics*, 46, 1100-1107.
- Hale, D., 2013, Dynamic warping of seismic images: *Geophysics*, 78, S105-S115.
- Herrera, R. H., Fomel, S., and Van der Baan, M., 2014, Automatic approaches for seismic to well tying: *Interpretation*, 2, SD9-SD17.
- Herrera, R. H., and van der Baan, M., 2014, A semiautomatic method to tie well logs to seismic data: *Geophysics*, 79, V47-V54.

- Kjartansson, E., 1979, Constant Q-Wave Propagation and Attenuation: *Journal of Geophysical Research*, 84, 4737-4748.
- Lines, L. R., and Newrick, R. T., 2004, *Fundamentals of geophysical interpretation*: Society of Exploration Geophysicists.
- Lloyd, H. J. E., 2013, An investigation of the role of low frequencies in seismic impedance inversion: M.Sc. thesis, University of Calgary.
- Margrave, G. F., 2013a, *Methods of Seismic Data Processing - Geophysics 517/557 Course Notes*: The Department of Geoscience, University of Calgary.
- Margrave, G. F., 2013b, Q tools: Summary of CREWES software for Q modelling and analysis: CREWES Research Report, 25.
- Margrave, G. F., 2013c, Why seismic-to-well ties are difficult: CREWES Research Report, 25.
- Margrave, G. F., and Daley, P. F., 2014, VSP modelling in 1D with Q and buried source: CREWES Research Report, 26.
- Margrave, G. F., and Lamoureux, M. P., 2001, Gabor deconvolution: CREWES Research Report, 13.
- Margrave, G. F., Lamoureux, M. P., and Henley, D. C., 2011, Gabor deconvolution: Estimating reflectivity by nonstationary deconvolution of seismic data: *Geophysics*, 76, W15-W30.
- Margrave, G. F., Mewhort, L., Phillips, T., Hall, M., Bertram, M. B., Lawton, D. C., Innanen, K. A. H., Hall, K. W., and Bertram, K. L., 2012, The Hussar low-frequency experiment: *CSEG Recorder*, September, 25-39.

Munoz, A., and Dave, H., 2012, Automatically tying well logs to seismic data: Center for Wave Phenomena Research Report 725,

Munoz, A., and Hale, D., 2015, Automatic simultaneous multiple well ties: Geophysics, 80, IM45-IM51.

O'Doherty, R. F., and Anstey, N. A., 1971, Reflections on amplitudes: Geophysical Prospecting, 19, 430-458.

Richards, P. G., and Menke, W., 1983, The apparent attenuation of a scattering medium: Bulletin of the Seismological Society of America, 73, 1005-1021.

Hampson-Russell Software Version HRS9R2.0, 2013, Hampson-Russell Software Documentation, a CGG Company.

White, R. E., and Simm, R., 2003, Tutorial: Good practice in well ties: First Break, 21, 75-83.

White, R. E., Thomas, R. T., and Castoro, A. 1998, Stretch and squeeze - Just keeping up appearances?: 60th EAGE Conference and Exhibition, 138-139.